Instabilities of jets of non-Newtonian fluids impacting a plate

by

Matthieu Varagnat

Ingénieur of the Ecole Polytechnique (Palaiseau, France)

Submitted to the Department of Materials Science and Engineering
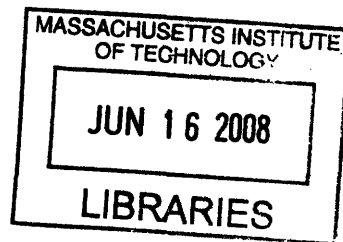in partial fulfillment of the requirements for the degree of

Master of Science in Materials Science and Engineering

at the

MASSACHUSETTS INSTITUTE OF TECHNOLOGY

June 2008

© Massachusetts Institute of Technology 2008

Signature of Author.

Department of Materials Science and Engineering
May 7, 2008

Certified by

Gareth H McKinley
Director, Hatsopoulos Microfluidics Laboratory
Director, Program for Polymer Science and Technology
Thesis Supervisor

Certified by

Michael J. Cima
Sumitomo Electric Industries Professor of Engineering
Thesis reader

Accepted by

Samuel M. Allen
POSCO Professor of Physical Metallurgy
Chair, Departmental Committee on Graduate Students

Instabilities of jets of non-Newtonian fluids impacting a plate

by

Matthieu Varagnat

Submitted to the Department of Materials Science and Engineering
on May 7, 2008, in partial fulfillment of the
requirements for the degree of
Master of Science in Materials Science and Engineering

Abstract

The problem of buckling and coiling of jets of viscous, Newtonian liquids impacting a plate
has received a substantial level of attention over the past two decades, both from experimental
and theoretical points of view. Nevertheless, most industrial and everyday life fluids are non-
Newtonian, and their rheological properties affects their behavior in this problem. The present
work aims at studying the instabilities of jets of such fluids falling on a plate, via both phe-
nomenological descriptions and theoretical analysis of jet motion and shape. Several fluids with
different rheological properties, including viscous Newtonian oil, model non-Newtonian fluids,
and commercial shampoos, are used and different dynamical regimes are documented. A special
focus is placed on viscoelastic, shear-thinning cetylpyridinium (CPyCl) solutions. In concen-
trated solutions, CPyCl surfactant molecules have been shown to assemble in long wormlike
micellar structures, which gives the fluid its non-Newtonian properties. Jets of CPyCl solution
show several novel shapes and dynamical regimes not observed in the case of Newtonian fluids.
The present study provides quantitative experimental measurements and mechanisms for these
novel features.

Thesis Supervisor: Gareth H McKinley
Title: Director, Hatsopoulos Microfluidics Laboratory
Director, Program for Polymer Science and Technology

Thesis reader: Michael J. Cima
Title: Sumitomo Electric Industries Professor of Engineering

Contents

6 Conclusion   **101**

Chapter 1

Introduction

Situations where a continuous stream of material is flowing downward onto a plane surface occur in both everyday life and industrial applications. Honey poured on toast, shampoo flowing out of a bottle, as well as numerous other examples in the oil, food, and cosmetic industries, are similar problems in which the stability of the streamline is a crucial feature (figure 1-1 (a) and (b)). For example, in these industries, bottles or other containers are often filled with different types of fluids, often having large variations in their rheological properties. This is usually done by moving the container below a nozzle connected to a reservoir of fluid. When the liquid flows from the nozzle, it creates a case of vertical jet of fluid impacting an horizontal surface with an imposed initial flow rate, and this is the problem studied in this work. The nozzle can also be lowered inside the bottle and raised as the bottle gets filled (a technique called "diving nozzle", figure 1-1 (c)), the nozzle can have varying shape, and the imposed flow rate can be varied by an automatic control system.

Depending on the fluid properties and the control parameters such as flow rate, the jet can exhibit different behaviors or regimes. The preferred regime from the industrial point of view is almost always the most stable one, with the jet remaining steady and the fluid flowing homogeneously in the container. Nevertheless, in most experimental conditions, the jet is not steady, for example capillarity can lead to drop breakup[1] (figure 1-1 (d)), low-viscosity fluids may undergo an hydraulic jump[2] (figure 1-1 (e)), or compressive forces can force the jet to buckle and to move out of the nozzle axis[3] (figure 1-1 (a) and (b)). And even if the jet is steady

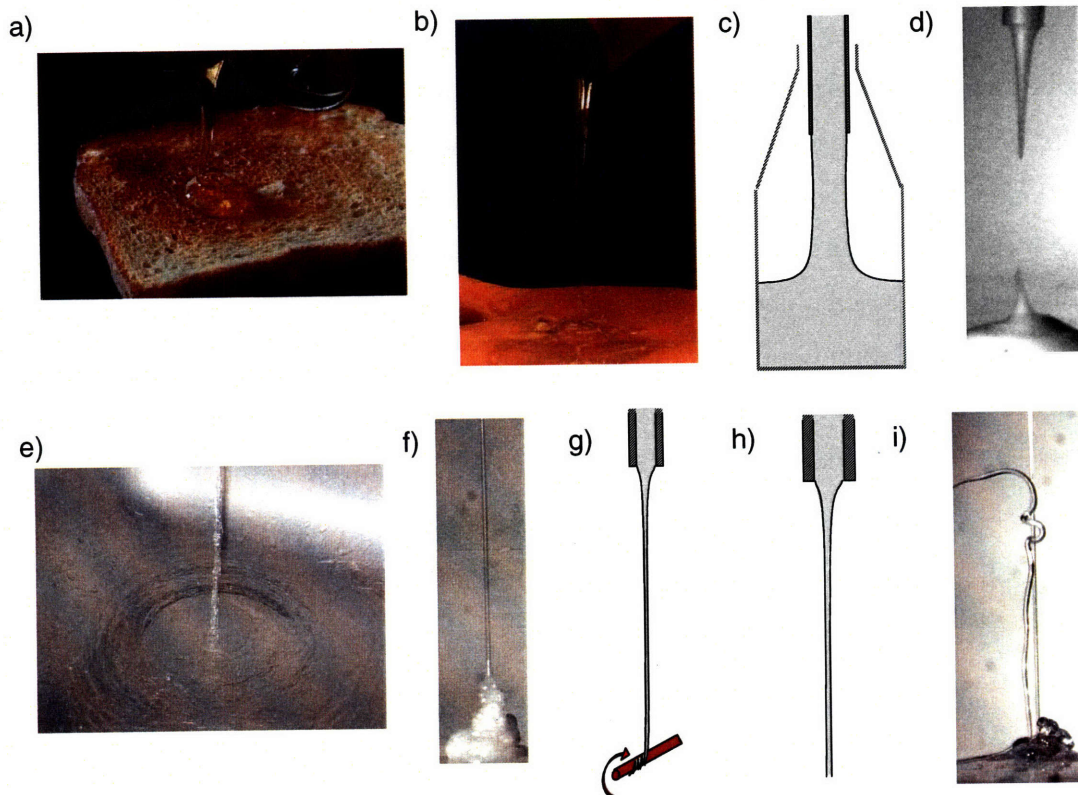Figure 1-1: Photos and sketches of several possible jetting situations. a) Jet of honey falling on a toast b) Jet of shampoo falling on a hand c) "Diving nozzle" filling technique, in which the nozzle is lowered inside the bottle d) Jet breakup e) Hydraulic jump f) Stack of fluid accumulating under the jet g) Fiber drawn by a wind-up mechanism, used with polymeric fluids h) Free-falling jet i) "Leaping" shampoo or Kaye effect.

the rheological properties of the fluid may prevent it from spreading uniformly in the container. For example, fluids with a yield-stress, very common in the food and cosmetic industries, will tend to build up a growing stack of material under the nozzle (figure 1-1 (f)), reaching the top of the container before it is entirely filled. Air bubbles can also be trapped by the various instabilities, leading to incomplete filling[4].

For these reasons there is an economic and technological interest in studying the rheological and flow parameters that control how the jet deforms. From a more fundamental point of view, the interplay between different forces explains the transitions between the various regimes, although most of them have been studied only in the simplest case of Newtonian fluids. In addition, the motion of buckled viscous jets is a matter of study in itself. The displacement of the centerline is often periodic, either having a circular trajectory around the vertical nozzle axis, or a pendulum-like planar oscillatory motion. The regularity of the periodic motion can in some cases be maintained for an extended period of time, building very regular stacks with a critical height that depends on the viscosity of the fluid. In other cases the jet quickly switches between two different frequencies, trajectory radius or plane of confinement, and may even switch between different flow regimes, up to the point where the motion loses all regularity and becomes chaotic ([3], [5], [6]).

So far, the research on jets impacting a plate has mostly focused on Newtonian fluids, for example with viscous fluids such as silicone oil. The object of the present work is to extend the field of study to non-Newtonian fluids, because of their relevance to many industrial problems, and to study how the rheology of the fluid affects its jetting behavior. The main focus of the study will be jets of wormlike micellar fluids, which are good model fluids for many products in the cosmetic industry, and because they have pronounced and tunable non-Newtonian properties, such as viscoelasticity and shear-thinning[7]. Other fluids will also be used for comparison purposes, such as a Newtonian silicone oil, shampoo bases, commercial shampoo, and polymer solutions.

The goal of the study is threefold. Firstly, it is an exploration of the unknown jetting behavior of these non-Newtonian fluids with respect to both flow parameters and fluid properties. For that purpose, extensive description of the possible regimes is provided, and dimensionless num-

bers characterizing the experiments are defined to obtain a clear picture of the regime diagram. These elements are used to establish experimental regime maps for several non-Newtonian fluids. The second objective is to understand the transitions between the regimes, which requires balancing the different forces at play using dimensional analysis and scaling laws. The third goal is to identify and document several of the most peculiar non-Newtonian features, such as the jet shape and jet motion, to find underlying physical mechanisms, and to compare theoretical scaling laws to experimental measurements.

The thesis is divided into six chapters including this introduction. Chapter 2 presents an extensive review of the existing literature on jets, as well as on non-Newtonian fluids. This review is especially focused on the elements used in this study, such as jets falling on plates and wormlike micellar fluids. Chapter 3 describes the experimental methods, including the characterization of non-Newtonian fluids and experimental setups to study the jets themselves. The parametrization of the problem and the relevant dimensionless numbers are defined in Chapter 4, followed by the description of the experimental results, including the regime diagrams, the critical conditions for transitions between regimes, and the influence of experimental parameters on jet shape and motion. In Chapter 5, physical mechanisms are proposed for the observed phenomena, and are used to derive scaling laws for the jet shape and motion, as well as the transitions between flow regimes. These theoretical laws are compared to experimental data and discussed. Finally, Chapter 6 we present the conclusions of the study and draw perspectives for future work.

Chapter 2

Literature overview and background

Jets of Newtonian fluids and rheological properties of non-Newtonian liquids have been extensively studied in the literature, but the intersection of the two domains is primarily focused on fibers drawn out of polymeric fluids (figure 1-1 (g)) and elasto-capillary breakup, in which the elastic forces in the fluid thread resist the thinning action of surface tension. Nevertheless, spectacular phenomena can occur with non-Newtonian fluids, such as the "leaping shampoo" or Kaye effect, shown on figure figure 1-1 (i). The goal of the present research is to extend a problem that has been studied only with Newtonian fluids, the buckling instability and subsequent unsteady motion of a jet falling on a plate, to non-Newtonian fluids. An overview of the literature covering jets, jet buckling, and relevant non-Newtonian fluid rheology is provided in the present chapter.

2.1 Liquid columns and jets

The subject of jets of fluids exiting a nozzle has been studied under a wide range of viewpoints. It could be, for example, the conditions to actually form a jet rather than to have fluid dripping from the nozzle. The shape of the jets under different physical situations is another subject covered in the literature. In order to provide a clear overview of the state of the art in this domain, the general topics of capillary thinning and breakup of liquid columns and of jets are first described in this section. Then, the problem of a jet falling on a plate is covered in detail, from the shape of stable jets, the conditions under which they buckle, to the subsequent coiling
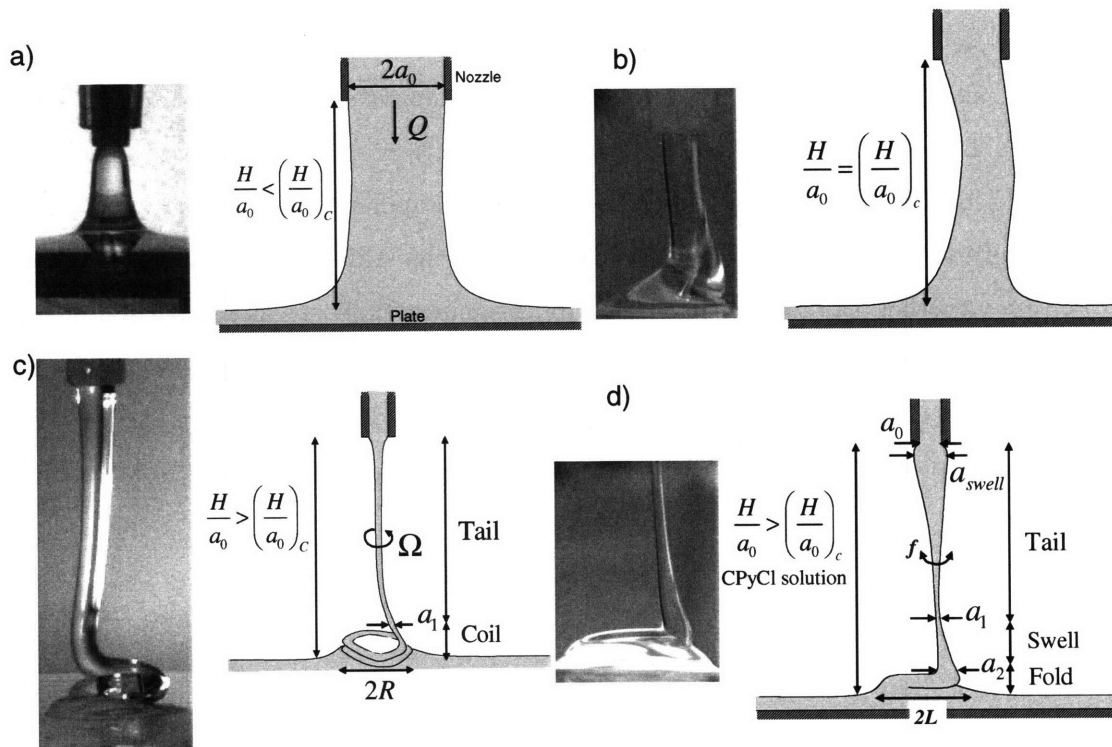
Figure 2-1: Instabilities of a fluid jet impacting a plate. a) The jet remains axisymmetric at low heights. b) Compressive forces in the jet lead to buckling at critical aspect ratio. c) Coiling jet. d) Folding jet. All photos are jets of a solution of CPyCl wormlike micelles, which will be detailed farther, excepted for photo c), with a silicone oil jet.

motion of the buckled jets.

2.1.1   Capillary breakup of liquid columns

Several physical forces can act on fluid columns, typically viscosity, inertia, gravity, and surface tension[8]. The effect of surface tension, or capillary force, is to destabilize the column, leading to thinning and breakup, whereas fluid inertia and viscosity tend to resist and slow down this breakup process. Non-Newtonian fluid properties, such as viscoelasticity, can also play a role[9]. The magnitude of each force can be estimated by dimensional analysis, and the comparison of two forces gives a dimensionless number that helps characterize the phenomenon and relevant

regimes. For example, the ratio of inertial forces to viscous forces is represented by the Reynolds number $Re = LU/\nu$, where L and U are characteristic transverse length and axial velocity of the jet, and ν is the fluid dynamic viscosity. For example in the situation presented in figure 2-1 (a), $L = a_0$, the nozzle radius, and $U = Q/(\pi a_0^2)$, with Q the imposed flow rate. In the same fashion, the Ohnesorge number compares the capillary forces to the viscous forces, and is usually written as $Oh^{-2} = \sigma L/\rho \nu^2$, where σ is the surface tension of the fluid, and ρ its density. Another way to interpret these dimensionless number is as comparison of timescales: the characteristic timescale over which diffusion-like viscous effects happen is $t_V = L^2/\nu$, inertial (convective) charateristic timescale is $t_I = L/U$, and processes balancing surface tension and viscosity typically take place over $t_{visc-cap} = L\rho\nu/\sigma$. The dimensionless number can then be written as

$$\mathrm{Re} = \frac{t_V}{t_I} = \frac{LU}{\nu} = \frac{Q}{\pi a_0 \nu} \qquad (2.1)$$

and

$$Oh^{-2} = \frac{t_V}{t_{visc-cap}} = \frac{\sigma L}{\rho \nu^2} = \frac{\sigma a_0}{\rho \nu^2} \qquad (2.2)$$

Jet column are destabilized by surface tension, eventually leading to breakup into drops, when the value of Oh^{-2} is much larger than unity. Most of the state of the art of jet breakup is covered in the comprehensive review by Eggers and Villermaux[9]. At large Re and Oh^{-2}, Lord Rayleigh[1] studied the breakup of inviscid columns of fluids under the effect of surface tension. Clanet and Lasheras also worked on inviscid jets and the transition between dripping faucets and continuous jets[10]. At still $Oh^{-2} \gg 1$ but $Re \ll 1$, the problem shifts to the visco-capillary thinning and breakup, studied by Papageorgiou[11]. Eggers developed an asymptotic theory for pinch-off in universal situation called inertial-viscous regime[12], and Doshi and co-workers also derived similar scaling laws for generalized Newtonian fluids[13], thus taking into account some non-Newtonian effects. The effect of non-Newtonian properties on jet breakup was also studied by Anna and McKinley[14], taking into account fluid viscoelasticity in elasto-capillary thinning. At large Re, another effect is that the jet becomes turbulent, and the aerodynamic friction can break it into a spray of droplets.
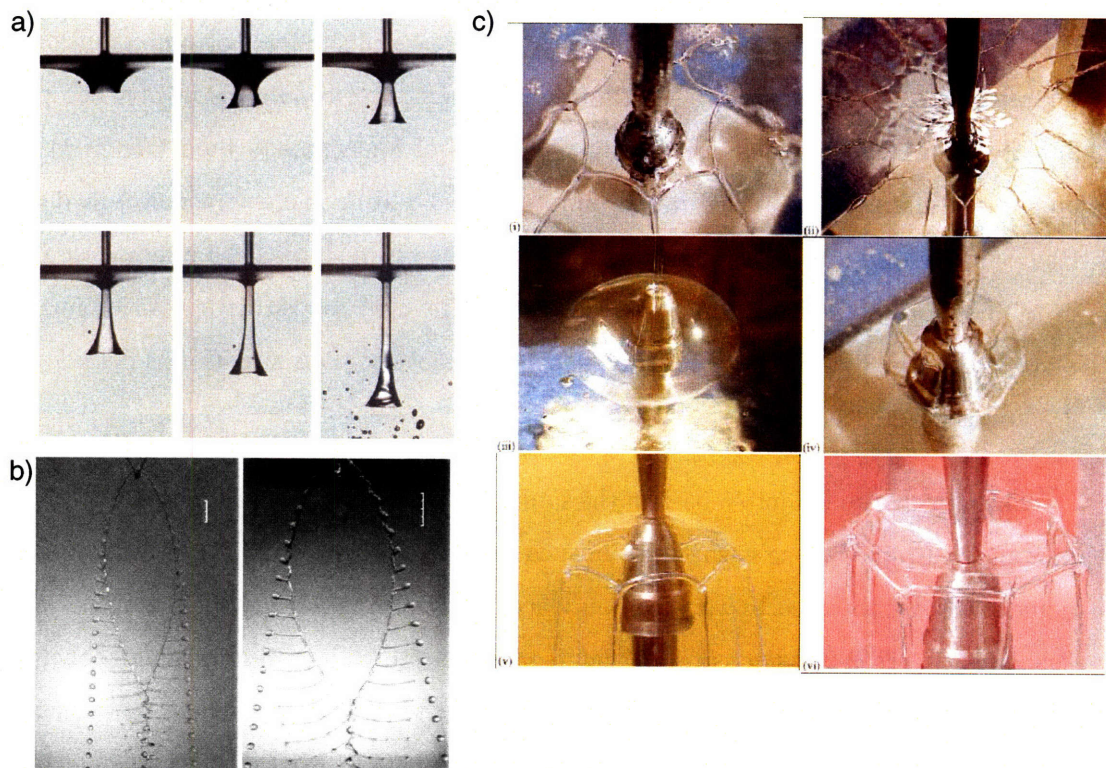
Figure 2-2: a) Jet of silicon oil impacting a bath of silicon oil and entraining air[17]. The pictures show steady situations, with increasing jet velocity from left to right and top to bottom. b) Water "fishbones" obtained from the collision of two liquid jets[18] c) "Polygons" of liquid obtained by extruding a water-glycerin mixture from an annulus[19].

2.1.2 Jets: the different situations

One way to sort the studies related to fluid jets is by looking at the imposed boundary condition. For jets falling from a vertical nozzle, many bottom-end boundary conditions are possible (figure 1-1). Most of the time, the jet is considered to be free falling, accelerating under the influence of gravity, as is the case when capillary breakup is studied. Polymer solutions, because of their capacity of withstanding large axial stresses, can be drawn into fibers by a windup mechanism (figure 1-1 (g)): in the study by Matovich and Pearson[15], the bottom condition is either imposed velocity or imposed driving force. Another set of conditions involve the presence of a bottom surface on which the jet impacts. Jets of low-viscosity fluid (Re > 1) impacting on a plate often create an hydraulic jump (figure 1-1 (e)), a phenomenon first described by Rayleigh[2] with an inviscid theory, while later Watson[16] showed the importance of viscosity in the phenomenon. Jets of more viscous fluids (Re < 1) can either spread uniformly on the plate, or buckle[3] and undergo a time-dependent motion. This situation is detailed on figure 2-1 and is covered below.

The jet can also fall into a bath of the same or a different liquid, and Lorenceau[17] described how air is entrained along with the jet in such a situation (figure 2-2 (a)). A variety of other phenomena can be obtained by varying boundary conditions, two beautiful examples being Bush's fishbones (figure 2-2 (b)) created by having two jets to collide[18], and fluid polygons (figure 2-2 (c)) when jets comes from an annulus[19]. The jet can also be oriented upward, creating an "umbrella" shape[20]. The external medium can be changed from air to vacuum or to a viscous fluid in order to study the influence of specific gravity, as illustrated by Cruickshank[26], or of friction with the external medium[21].

The case of interest in this study is the case when the jet falls on a plate. The jet can either spread on the plate, homogeneously or with a hydraulic jump, or buckle when the compressive stress are too large. Bejan[22] points out that buckling occurs typically with a wavelength on the order of the jet radius, and therefore requires a height of fall at least of the order of the radius to appear. Kimura and Bejan described such a buckling with water[23], on length scale shorter than the capillary length $\kappa^{-1} = \sqrt{\sigma/\rho g}$ in order to avoid capillary breakup. Nevertheless, in the present study, we are interested in downward-pointing jets, with viscous fluids, at low Re
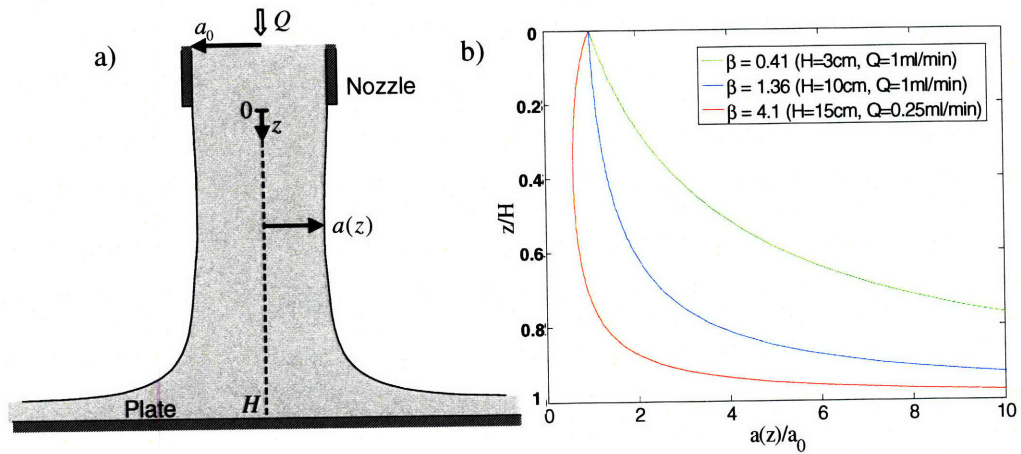
Figure 2-3: a) Situation at low height: the jet is steady, the shape is governed by the balance between gravitational and viscous forces. b) Theoretical jet profiles for different values of β.

and Oh^{-2}, impacting on a flat plate. The main focus is on established regimes rather than transient phenomena, therefore the real condition is a thin layer of viscous fluid covering the bottom plate, rather than the plate alone. We now review in more detail the literature covering this situation.

2.1.3   Shape of steady flows

The figure 2-3 (a) shows the situation at low height, with a round nozzle. The nozzle-plate distance is H, and the fluid exits the nozzle of radius a_0 with an initial flow rate Q. At low height - the precise criteria will be defined in the next section - the jet remains stable and spread homogeneously on the plate. The vertical axis is noted z, from $z = 0$ at the nozzle and $z = H$ at the plate. The problem is axisymmetric, with the jet radius at height z noted $a(z)$, and is reduced to a one-dimensional problem. The fluid velocity is assumed constant throughout any horizontal cross-section, and inertial and surface tension effects are neglected, so the flow is governed by a balance between gravity and viscosity. Cruickshank and Munson[24] have shown that the shape of the jet is given by a transcendental equation depending on the value

15

of $\beta = H/a_0 K$, where K is given by $K^2 = 6Q\nu/ga_0^4$ and g is the acceleration of gravity.

If $\beta = 1$, the shape of the jet is described by

$$\frac{a(z)}{a_0} = \frac{1}{1 - \frac{z}{a_0 K}} \tag{2.3}$$

For $\beta < 1$, then

$$\frac{a(z)}{a_0} = \frac{\sinh(c_1)}{\sinh(c_1 - \frac{z}{a_0 K}\sinh(c_1))} \tag{2.4a}$$

$$c_1 - \beta\sinh(c_1) = 0, \ c_1 \neq 0 \tag{2.4b}$$

For $\beta > 1$, the shape is described by

$$\frac{a(z)}{a_0} = \frac{\cos(c_2)}{\cos(\frac{z}{a_0 K}\cos(c_2) + c_2)} \tag{2.5a}$$

$$\beta\cos(c_2) + c_2 = \frac{\pi}{2}, \ c_2 \neq \frac{\pi}{2} \tag{2.5b}$$

Jet profiles obtained from these equations for different values of β are shown in figure 2-3 b. Note that it is only for $\beta > \pi/2$ (covered by equation (2.5a)) that the jet thins under the influence of gravity instead of monotonically enlarging while spreading on the plate. For typical experimental values, $\nu = 200$ cm^2/s, $Q = 3$ mL/min, $a_0 = 1.25$ mm, this gives $H = 3$ cm. If the height of fall is lower, it does not allow a significant gravitational acceleration, and then the radius remains constant. β is therefore the important factor that controls the onset of gravitational thinning. The onset of gravitational thinning is

$$\beta = Ha_0\sqrt{\frac{g}{6Q\nu}} = \frac{\pi}{2} \tag{2.6}$$

which can be re-arranged into

$$H_{thinning} \sim Q^{1/2} \tag{2.7}$$

This means that when the flow rate is larger, the nozzle must be higher for gravitational thinning to take place.

2.1.4 Gravitational thinning

Fluid particles accelerate along the jet as result of the competition between the effect of gravity and the resisting effects of viscosity. Inertia is negligible since the Reynolds number as defined in equation (2.1) is small. Because of the incompressibility of the fluid, the jet thins from an initial radius a_0 to a final value a_1. Thinning occurs mostly in the tail of the jet, as defined in figure 2-1 (c). The gravitational stress in the tail is the weight of a column of fluid of height l_{VG}, where $l_{VG} = (\nu^2/g)^{1/3}$ is the characteristic length over which gravitational and viscous effects balance each other. The stretch rate is $Q(1/a_1^2 - 1/a_0^2)/H$, therefore the extensional viscous stress is given by $3\eta Q(1/a_1^2 - 1/a_0^2)/H$ for a Newtonian fluid, where η is the dynamic viscosity. The force balance gives

$$3\eta \frac{Q}{H}(\frac{1}{a_1^2} - \frac{1}{a_0^2}) = \rho g l$$

For $a_1 \ll a_0$, this can be simplified into

$$a_1 \sim \sqrt{\frac{3\nu Q}{Hgl_{VG}}} \tag{2.8}$$

Note that this scaling law for a_1 does not refer to a_0: for a height of fall large enough $(\beta \gg \pi/2)$ so that $a_1 \ll a_0$, then the final radius of the jet is entirely determined by the force balance in the tail.

2.1.5 Buckling

The steady jet is actually stable only for a relatively narrow range of parameters(figure 2-1.(a)). At larger heights, even if the solution of equation (2.5a) remains valid, it is no longer stable, and the jet tends to buckle. Any variation sideways of the centerline of the jet gives rise to outward-pointing viscous stresses that push the jet even farther. These problems are a subset of the general subject of flow instabilities, and were classified by Bejan[22] as obstacle-driven instabilities of jets at low-Reynolds number. Taylor[25] and Cruickshank[26] were among the first to study the buckling problem, shown schematically in figure 2-1.(b). Cruickshank and Munson[3] studied jet buckling experimentally in the cases of planar and axisymmetric jets of Newtonian fluids. Theoretical derivations in good agreement with these experimental results

17

were developed by Cruickshank[27] and Tchadarov[28] in the axisymmetric geometry and Yarin and Entov[29] in the planar one.

Cruickshank showed that an axisymmetric jet can buckle according to two modes, azimuthal and non-azimuthal (that we call respectively coiling and folding in this thesis) and derived a critical buckling height for each mode, given by

$$\frac{H}{2a_0} = 7.663 \text{ (coiling)} \tag{2.9a}$$

$$\frac{H}{2a_0} = 4.810 \text{ (folding)} \tag{2.9b}$$

where H is the height of fall and a_0 is the radius of the nozzle. Experiments with Newtonian fluids show that in most cases, the jet transitions directly from stable jet to coiling jet, at a critical height given by (2.9a). A significantly higher critical height was reported (figure 11 in [3]) at low flow rate and high surface tension, respectively characterized by $\nu Q/ga_0^4 < 10$ and $\sigma/\rho g a_0^2 > 1$, where Q is the flow rate, ν is the kinematic viscosity, σ the surface tension, and ρ the density.

However, Cruickshank ([3] and [27]) that above an upper limit on the Reynolds number, as defined in equation (2.1), the instabilities disappear. For cylindircal jets, this limit is Re $= Q/\pi \nu a_0 = 1.2$. He also reports that just below this limit, for $1 < \text{Re} < 1.2$, two transitions from a stable jet to folding and from folding to coiling were observed as the height of fall was progressively increased. The first transition or buckling happens roughly at the critical height predicted by (2.9b), and the height of the folding-coiling transition is approximately given by (2.9a), although this is harder to measure experimentally because of the difficulty at distinguishing between coiling and folding at the low values of $H/2a_0$ at the buckling transition.

The Reynolds number defined at the nozzle exit, $Re = 2Q/\pi a_0 \nu$ must also be sufficiently low, otherwise the jet spreads on the plate, in some case leading to hydraulic jump as in figure 1-1 e). The limits are[3]

$$\text{Re}_{c\ circ} = 1.2 \tag{2.10}$$

18

in the axisymmetric geometry, and

$$\text{Re}_{c\ plan} = 0.56 \qquad (2.11)$$

in the plane case. On the other extreme, at very low flow rate, the fluid does not form a fully continuous jet. It either drips from the nozzle[20] or forms a jet that is destabilized by surface tension before it reaches the bottom plate[1].

Only when all of these conditions are met can fluid buckling occur, which is the reason why it typically happens with viscous fluids such as silicone oil and not with water, although Bejan[22] reminds us that another type of buckling, caused by inertia and the friction with the surrounding medium, happens at large Reynolds numbers and has been observed with water.

In all the above analysis the surface tension parameter $\sigma/\rho g a_0^2$ that compares the thinning processes due to capillarity and to gravity is much smaller than unity. Cruickshank and Munson have reported experimental data for a surface tension parameter slightly larger than one[3], but never to the point that the destabilizing action of the capillary forces breaks the jet into droplets.

2.1.6 After buckling: coiling of Newtonian jets

After buckling, round jets of viscous fluid oscillate periodically in a coiling motion around the vertical axis (figure 2-1.(c)). The coiling motion can be extremely periodic, as can be seen on figure 2-4 (a). Studying this problem requires us to understand the forces at play, as well as predicting the radius of the coils and the frequency of this periodic motion. Other aspects can be studied, for example, Pouligny and Chassandre-Mottin[4] studied the entrainment of air bubbles in the folds of viscous sheets, which is important in problems such as bottle filling, food processing, or nuclear waste disposal.

In the limit of large heights of fall, Mahadevan and co-workers([5] and [30]) derived both expressions for the coiling radius and frequency from a balance between viscous and inertial forces in the coil, the viscous forces arising from the curvature of the jet in that region. Ribe[6] showed that this analysis was a subset of a broader picture, with three distinct regimes, viscous, gravitational and inertial, depending on which forces were dominant. The scaling laws for coiling

19
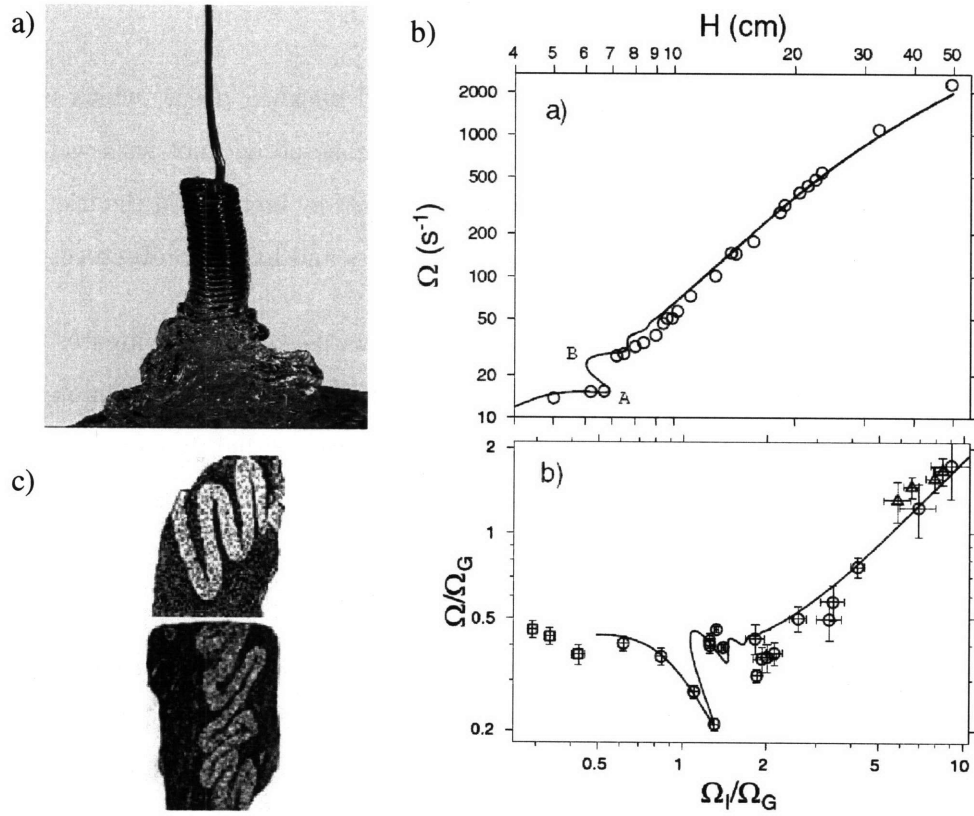
Figure 2-4: a) Coiling of viscous silicon oil, from Mahadevan[5] b) Experimental data (circles) and numerical prediction (line) by Maleki et al. of the coiling frequency at the transition between gravitational and inertial coiling[31] c) Folding patterns in geology, example of folding of sheets of very viscous fluids[32].
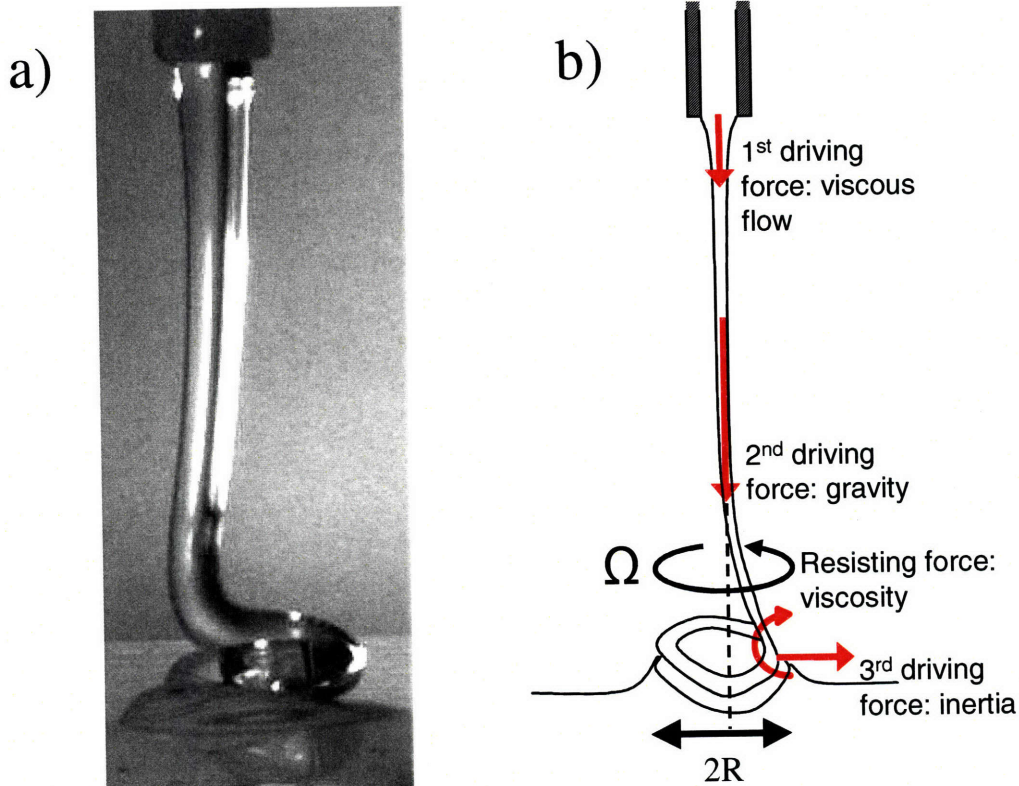
Figure 2-5: a) Coiling jet of Newtonian silicone oil b) Schematic view of the coiling motion of an axisymmetric jet of Newtonian fluid

amplitude and frequency are presented below. His simulations and experiments by Maleki and co-workers of the frequency of coiling as a function of height, for a given flow rate, were in good agreement and showed multi-valued frequencies at the transition between gravitational and inertial regimes[31].

2.1.7 Theoretical analysis of Newtonian coiling

After the onset of buckling of a cylindrical jet, the jet tends to fall vertically, therefore subjecting the outmost part of the buckled region to a buckling torque that pushes it farther away from the vertical axis. This process can be dominated by different forces, either gravity (the weight of the fluid in the tail), the viscous stresses induced by the downward flow that resist sideways motion, and at high coiling frequency, the rotational inertia in the coil can also be the main

buckling force. The curvature of the jet, in return, leads to shear velocity gradients across the jet cross-section that create a viscous torque that resists the deformation, analogous to the strain-induced elastic torque in a bent beam. At the onset of buckling this torque is negligible, and increases with further bending. When it becomes equal to the driving torque, further bending is prevented, and the only way to dispose of the incoming fluid is sideways, in an azimuthal motion (figure 2-5 (a)). The curvature and the torques remain the same in that motion (figure 2-5 (b)), therefore the coiling of Newtonian jet can be studied by balancing the different contributions to the torque at the outmost point of the jet (see [5] and [6] for details).

Forces involved in Newtonian coiling.

One can divide the coiling regime into different subregimes, according to which force drives buckling, therefore leading to a different balance and different scalings for the frequency of the motion and the radius of the coils. Under the assumption that the jet radius is constant in the coil, frequency, coiling radius, and final radius of the jet, are connected by the conservation of volume

$$Q = \pi \Omega R a_1^2 \qquad (2.12)$$

The resisting torque is always due to viscosity. Viscous stresses arise because of the velocity gradient between the inner part of the curved jet where the velocity is smaller and the outer part where it is maximum. The velocity gradient scales like $U_1 a_1 / R^2$, where $U_1 = Q/\pi a_1^2$ is the axial velocity just before the coil In a fashion similar to beam-bending in solid mechanics, the viscous stress $\eta Q/\pi R^2 a_1$ integrated over the jet cross-section vanishes, but the integrated torque remains non-zero and scales like [30]

$$T_{resisting_{coiling}} \sim \frac{\eta Q a_1^2}{R^2} \qquad (2.13)$$

Predictions for amplitude and frequency

Viscous regime At low heights of fall, the whole tail of the jet is bent sideways, and the force controlling the motion is the viscous torque caused by the fixed vertical orientation of the nozzle (the first driving force in the schematic view of figure 2-5 b)). It is also a shear-induced torque, around a characteristic curvature $1/H$, that scales like $\eta Q a_1^2 / H^2$. The torque balance

leads to [6] the scaling laws for the coiling radius R_V and frequency Ω_V given by:

$$R_V \sim H \tag{2.14a}$$

$$\Omega_V \sim \frac{Q}{a_0^2 H} \tag{2.14b}$$

In this regime, the jet motion is controlled by external parameters such as height of fall and imposed flow rate, whereas in the other two regimes the fluid selects its own dynamics through a balance of forces involving intrinsic fluid properties as well as external parameters.

Gravitational regime At larger heights of fall, only the lowest part of the tail is bent, on a length scale of the coiling radius R. The weight of the fluid in this part is of the order of $\rho g R a_1^2$, the lever arm is of order R, so the buckling torque is $\rho g R^2 a_1^2$. Using the scaling (2.8) for a_1, the torque balance gives [6] the scaling laws for the coiling radius R_G and frequency Ω_G:

$$R_G \sim \left(\frac{\nu Q}{g}\right)^{\frac{1}{4}} \tag{2.15a}$$

$$\Omega_G \sim H^2 \left(\frac{g^5}{\nu^5 Q}\right)^{\frac{1}{4}} \tag{2.15b}$$

The transition from viscous to gravitational regime happens [6] for $\Omega_G \simeq 2\Omega_V$, or $H_{VG} \simeq (Q\nu/g)^{5/12} a_0^{-2/3}$. Note that if this height H_{VG} is lower than the buckling height $H_{buckling} = 2 \times 7.663 a_0$, then coiling simply starts in gravitational mode (a schematical view of this situation is provided in figure 5-2). Indeed, for typical experimental values of $\nu = 200$ cm^2/s, $a_0 = 1.25$ mm, and $Q = 3$ mL/min, $H_{VG} \simeq 0.5$ cm while $H_{Buckling} \simeq 1.9$ cm. Note also that a simpler force balance between gravitational and viscous forces, in other words given by $\beta \approx 1$, would have led to a result quite similar of $H \simeq (Q\nu/g)^{1/2} a_0^{-1}$ which shows the consistency of the force balance.

Inertial regime When the rotational inertia in the coil becomes important it can drive the coiling as well. The inertial force in a rotational reference frame scales per unit volume as $\rho \Omega^2 R$, so the torque scales as $\rho \Omega^2 R^3 a_1^2$. The torque balance together with (2.8) and (2.12) leads to

[30] the scaling laws for the coiling radius R_I and frequency Ω_I

$$R_I \sim \nu g \left(\frac{Q}{H^4} \right)^{\frac{1}{3}} \tag{2.16a}$$

$$\Omega_I \sim \frac{1}{\nu^2} \left(\frac{g^5 H^{10}}{Q} \right)^{\frac{1}{3}} \tag{2.16b}$$

This regime becomes the most stable one when $\Omega_I > 2\Omega_G$ [6], i.e. for $H_{GI} \simeq \left(Q\nu^9/g^5 \right)^{1/16}$. For the values used above, this represents $H = 11.0$ cm. Note that for $\Omega_G < \Omega_I < 2\Omega_G$, the system is multivalued, with the solution oscillating between the two possible frequencies, as reported in figure 2-4 (b).

2.1.8   Similar and related problems

Viscous sheets

The case of planar viscous sheets, created using a long slit instead of a round nozzle, has also been studied by Skorobogatiy and Mahadevan[32] and extended by Ribe[33]: in that case, the viscous sheet folds on itself back and forth. A viscous jet that is confined in two dimensions, for example a thread of viscous soap falling on a soap film, or a geological layer flowing under tectonic forces (figure 2-4 (c)) follows the same pattern[32]. Once again, different regimes with different scalings for the amplitude of folds and frequency of motion exist, depending on the respective magnitude of the viscous and inertial forces.

Elastic ropes and sheets

A connected problem with striking similarities has been presented by Mahadevan and Keller for the folding of elastic sheets[34] and the coiling of elastic ropes[35], and has been extensively covered by Habibi and co-workers[36]. The elastic material is continuously fed downward onto a planar surface, with an experimental setup reminiscent of applications such as the folding of drapes and of paper, and the pattern spontaneously formed by a rope that falls on the ground. The force that resists bending is the elasticity of the material, and the elastic bending stiffness in this situation is the direct analog of the viscous one in the fluid case. For elastic ropes of circular cross-section, the best analog of the viscous round jets we have been discussing, Habibi

gives the magnitudes per unit length of the three forces that can play a role:

$$\text{Elastic force } F_E \sim E a_0^4 R^{-3} \tag{2.17a}$$

$$\text{Gravitational force } F_G \sim \rho g a_0^2 \tag{2.17b}$$

$$\text{Inertial force } F_I \sim \rho U^2 a_0^2 R^{-1} \tag{2.17c}$$

where E is the elastic modulus and U is the imposed downward velocity. Three regimes are possible depending on which force dominates. The elastic regime happens at low height, for which the amplitude of the deformation is solely bounded by geometrical constraints. The gravitational regime happens at larger height and moderate velocities, and the inertial regime begins beyond large enough values of height and velocity. The force balances, derived in a way similar to the viscous jet problem, lead to the coiling frequency in each regimes:

$$\Omega_E \sim U H^{-1} \tag{2.18a}$$

$$\Omega_G \sim U(\rho g / E a_0^2)^{1/3} \tag{2.18b}$$

$$\Omega_I \sim U^2(\rho / E a_0^2)^{1/2} \tag{2.18c}$$

The only qualitative difference between the coiling motions of flexible elastic ropes and round viscous jets is the existence of two resonant eigenmodes within the inertial regime of the elastic ropes. The two eigenmodes are the "whirling shaft" in which the rope is totally rigid and the "string" in which its bending resistance is negligible. As a result, Habibi shows that the numerically-simulated frequency as a function of height in the inertial regime oscillates around the predicted value of Ω_I, alternatively entering one of the two eigenmodes.

Kaye effect

A side interest of this problem is to help understand the phenomenon of "leaping shampoo" or Kaye effect, as can be seen in figure 1-1 (i). Jets of some non-Newtonian fluids, including some commercial shampoos, falling on a plate from moderate heights, around ten or twenty centimeters, tend to produce a bouncing jets, an phenomenon first described in 1963 by Kaye[37] and studied by Collyer and Fisher[38] and Versluis and co-workers[39]. The criteria for the

appearance of the secondary jumping jet is a significant shear-thinning character of the fluid, creating a thin lubrication layer on which the jet "slides". Nevertheless, all shear-thinning fluids do not seem to systematically lead to the Kaye effect, and studying the behavior of non-Newtonian jets may help to derive an additional criteria.

2.2 Non-Newtonian fluids

As we have shown above, the instabilities demonstrated by both elastic solids and viscous liquids have a qualitatively similar behavior. A natural route is to investigate what happens when the flowing material is a viscoelastic fluid. Does an "intermediate" material behave the way the two extremes do, or does a different physical mechanism lead to different behavior? Moreover, the range of non-Newtonian properties that can be exhibited by a fluid jet is not limited to viscoelasticity: shear-thinning or thickening behavior, the presence of a yield stress, or thixotropy, are all likely to have a great influence on the regimes shown by jets. In addition, real-life fluids are almost never Newtonian. Pastes and gels are ubiquitous in the healthcare, cosmetic, and food industries. The kitchen and the bathroom are full of examples of rheologically complex fluids, from ketchup and mayonnaise to foaming detergents, skin creams, and hair conditioners. Wormlike micellar fluids are non-Newtonian fluids that have recently attracted a lot of attention for their strong, tailorable viscoelastic properties, their ease of use, and the possibility they offer as model fluids for everyday life products[40]. We now present a brief overview of the main characteristics of non-Newtonian fluids, as well as a deeper description of wormlike micellar fluids.

2.2.1 Newtonian versus non-Newtonian behavior

Newtonian fluids are defined by the fact that they follow Newton's description of viscosity. According to this description, the relationship between the shear stress τ imposed to a fluid and the shear rate $\dot{\gamma}$ at which it deforms (or, reciprocally, the imposed shear rate and the induced shear stress) is linear: $\tau = \eta\dot{\gamma}$. The coefficient of proportionality η is called viscosity. Newtonian fluids tends to be composed of small molecules without significant ordering or supramolecular structures, with common examples such as honey, silicone oil, and water.

Most fluids, nevertheless, do not follow this pattern, or only for a limited range of shear rates and stresses. Fluids that show a deviation from Newtonian behavior in experiments are commonly referred to as non-Newtonian fluids[41].

There are many kinds of non-Newtonian behaviors. Perhaps the simplest departure from linear behavior is Generalized Newtonian Fluid in which the viscosity is a function of shear rate or shear stress. If $\eta(\dot{\gamma})$ decreases with increasing shear rate, the fluid is said to be shear-thinning; if it is increasing, the fluid is shear-thickening. Most dilute polymer solutions are shear-thinning, whereas a concentrated corn starch suspension is a common example of shear-thickening material.

Viscoelasticity means that the material can have solid-like and fluid-like responses to an external stimulus, i.e. that the stress is both a function of the strain and the strain rate. Typically, such a material will respond like a solid when submitted to rapid or short-term experiments, and will flow or creep at long times. Time becomes a critical parameter of an experiment, since viscoelastic fluids are "memory" fluids, with the effect of external actions decaying over time. Soft rubbers and polymer solutions are two examples of viscoelastic materials at the two ends of the solid-fluid continuum.

Yield stress fluids are materials of infinite initial viscosity, which flow with little resistance once the imposed stress overcomes a certain yield value, for example dense pastes such as toothpastes are usually considered yield stress fluids. However, the concept of yield stress is abstract, and $\pi\alpha\nu\tau\alpha\ \rho\epsilon\iota$ - everything flows, as pointed out by Barnes[42] and "Dr. Watson"[43]. In other words, there is only an apparent yield stress, denoting the transition between a power-law regime of very large yet finite creep viscosity at low stresses and a Newtonian regime of lower viscosity at larger stress. In order to avoid the controversy the term "critical stress fluids" may be preferred to cover all fluids with such two viscosity regimes. For example, mayonnaise and ketchup are common critical stress fluids. Thixotropic fluids are yet another type of fluids, in which their history of deformation determines the present response with strong hysteresis.

All of this properties could be of interest from both scientific and industrial point of views. Nevertheless, all non-Newtonian fluids are not equally suited for our study. During jet experiments, many problems arise: yield stress fluids, for example, usually require a lot of energy to

27
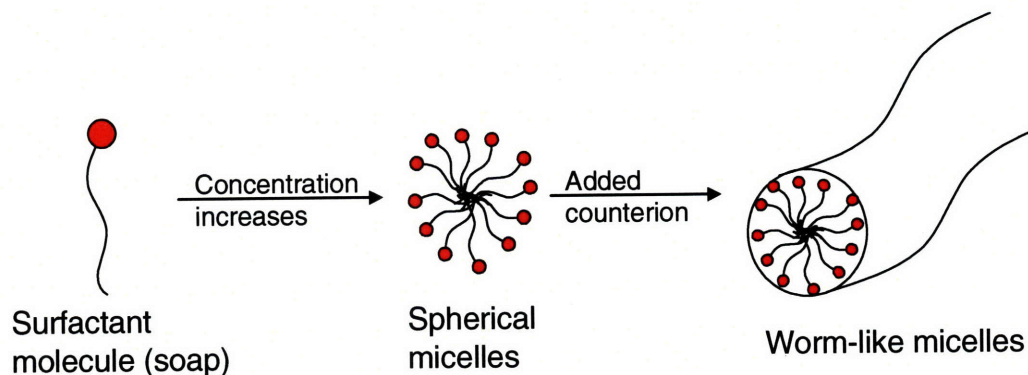
Figure 2-6: Schematic view of the wormlike micelles assembly process

be pumped to flow, they tend to neck and to fall in large drops instead of forming a jet, it is hard to get rid of trapped bubbles in the system, and they form a heap or mound rather than spreading spontaneously on the plate[44]. Shear-thickening fluids are even more troublesome, since they will thicken when pumped to flow, and are often two-phase fluids prone to sedimentation. Thixotropic fluids will be critically affected by the stresses needed to pump them to jet, thus leading to very difficult reproducibility of the experiments

This study focuses primarily on wormlike micellar solutions, both strongly viscoelastic and shear-thinning, and with jetting properties suitable for this study. Their non-Newtonian characteristics make the jet behavior qualitatively different from its Newtonian counterpart. They are also very convenient to use, especially when compared to polymer melts or polymer solutions in organic solvents, and their properties can be easily tuned by varying the concentration of surfactant or salt.

2.2.2 Micellar Fluids

Structure

Wormlike micellar fluids are concentrated aqueous solutions of one or more ionic surfactants, as well as a counter-ion salt (figure 2-6). At very low surfactant concentration, the solution is homogeneous, but when the concentration increases above a critical threshold, the critical

28

micellar concentration or CMC, the surfactant molecules spontaneously assemble in spherical structures. In these spherical micelles of nanometric size the surfactants point their organic tail towards the center and bear their ionic head outside, satisfying both tail segregation and ionic repulsion driving forces. Adding a large enough counter-ion reduces the curvature of the optimal shape, by screening the ionic interactions. The same effect can also be attained by using an additional surfactant of a different length, changing the steric hindrance between the tails. The change of optimal curvature leads, for some combinations of surfactants and counter-ions, to changes in the shape of the assembly[45].

Several shapes can be obtained, and some carefully chosen systems exhibit long linear structures, called wormlike micelles, in some parts of their phase diagrams. Solutions of erucyl bis(2-hydroxyethyl) methyl ammonium chloride (EHAC) were used by Yesilata and co-workers[7], Rothstein[46] used cetyltrimethylammonium bromide (CTAB). Rehage and Hoffmann[40] as well as Berret and co-workers[47]used a solution of CetylPyridinium Chloride (CPyCl) and salicylic salt (NaSal) in brine that is employed in this study.

Properties

Wormlike structures at high enough concentrations in surfactant and salt are long enough to entangle, therefore giving pronounced viscoelastic properties to the solution. Stress relaxation with wormlike micelles can operate along two processes: the first one is reptation, similar to the stress relaxation process of polymers described by de Gennes[48], and the second one is a breakup-recombination process that is unique to living systems. The respective characteristic timescale for each of these relaxation processes are λ_r and λ_b and Cates showed that, for $\lambda_b \ll \lambda_r$, the small oscillation shear rheology is well described by a single-relaxation-time Maxwell model of characteristic time [49]

$$\lambda = (\lambda_r \lambda_b)^{\frac{1}{2}} \tag{2.19}$$

In steady shear flow, wormlike micellar solutions are critical-stress fluids, with a characteristic shear rate $1/\lambda$ and a zero-shear-rate viscosity η_0 that is strongly dependent on the salt concentration. For shear rates above $1/\lambda$, it is found that the shear stress remains constant at

a critical stress of the order of $\lambda \eta_0$.

In addition, both λ and η_0 are observed to be strongly temperature dependent, in an Arrhenius-type dependence with a very large activation energy. The strong variations of rheological properties with temperature comes from two effects acting in the same direction. The first is a polymer-like behavior in which reptation, a thermally activated process, happens faster at higher temperature. The second is specific to supramolecular structures: the breakup rate increases with temperature, which is not only a stress relaxation process on its own, but also tends to shorten the average length of wormlike micelles, thus requiring a shorter length for reptation.

Extensional rheology studies of wormlike micellar solutions have been conducted by capillary breakup experiment (CaBER) ([7], [50]), and showed a significant extension strengthening of the fluid, likely due to the alignment of the wormlike micelles in the extension flow[46], quite like what happens for dilute polymer solutions. For example, in the case of CPyCl micellar solutions, Bhardwaj and co-workers have shown[50] that the fluid first undergoes an initial phase of Newtonian visco-capillary thinning[7]. As the liquid bridge thins, the extension rate, denoted $\dot{\epsilon}$, increases, until the local Weissenberg number $Wi_{mid} = \lambda \dot{\epsilon} = 0.5$. At that point the wormlike micelles are stretched by the flow too rapidly to relax, which lead to extension thickening with elastic stress buildup resisting the breakup of the thin filament. In contrast to polymer solutions however, when the local tensile stress become too large for the micelles to resist, rupture *en masse* of the entangled chains results in filament breakup[46]. In addition, thin liquid bridges and jets have a large area-to-surface ratio, and therefore solvent evaporation can tend to cool the fluid and increase the surfactant concentration, both effects increase the viscosity and lower the thinning rate.

Chapter 3

Experimental methods

Experiments play two important roles in this thesis. The first set of experimental methods presented here are used to characterize the fluids employed in the jetting, which is especially important for non-Newtonian fluids because some of their characteristic properties can vary drastically with the flow conditions and mode of deformation. The second set covers the techniques used to both describe qualitatively the different flow regimes of a jet falling on a plate and study quantitatively the jet behavior.

3.1 Rheological characterization of test fluids

Although the main focus of the study is the behavior of jets of wormlike micellar solutions, several other fluids are also considered. Some fluids such as silicone oils and Boger fluids are used as reference fluids, for qualitative comparison purposes only, but shampoo bases and commercial shampoo are also used to connect the research to industrial applications.

3.1.1   Fluid formulations

Micellar fluid

The type of fluid we use mostly for this study is are solutions of CPyCl and NaSal in brine (100 mM of NaCl salt solution). Following the study in [50], a fluid in the desired range of viscosity and elasticity in obtained with the concentrations [CPyCl] = 100 mM, and [CPyCl]:[NaSal] = 2:1. For the sake of comparison two other fluids were prepared with the same brine and the

same [CPyCl]/[NaSal] ratio but [CPyCl] = 75 mM and [CPyCl] = 150 mM respectively. The three fluids will be denoted CPyCl 100, 75 and 150 in the rest of the study. CPyCl and NaSal were obtained in dry form from MP Biomedicals and Sigma-Aldrich respectively.

Shampoo bases

Another class of fluid we investigate is a range of shampoo products, in order to relate our research to industrial subjects. These products include shampoo bases (shampoo without some of the fragrances and active products added at the end of the industrial process), with different amount of NaCl salt, respectively 1.5, 1.8 and 2.7% wt. These will be referred to as SB 1.5, SB 1.8, and SB 2.7 respectively. Shampoos are, among other components, concentrated surfactant solutions. These surfactants assemble into different types of micelles as they do for CPyCl solutions, often leading to non-Newtonian behavior. As the amount of salt increases, the micelles get longer, thus increasing these effects. The increase in viscosity that results from adding salt is called "trimming" in industrial operations[44].

Reference fluids: silicone oil and Boger fluid

Other fluids of interest were a silicone oil T41 from Gelest, Inc and a Boger fluid, which is a dilute (0.025 wt %) solution of high molecular weight polystyrene in highly viscous styrene. The polystyrene has a molecular weight of 2.25×10^6 g/mol, with a monodispersity index of 1.03. The silicone oil will be used as a reference Newtonian fluid, and the Boger fluid will be used for qualitative comparison purposes, because it is a viscoelastic fluid that is not shear-thinning.

Commercial Shampoos

Two commercial shampoos are used in this study, "Totally Twisted" from Herbal Essence (referred to as Herbal in this study) and Pantene Pro-V "Classic Clean Shampoo and Conditioner" (referred to as Pantene). Because of their complex formulation, with many components on which we have little control, the commercial shampoos will not be used in most of the study. Their use will be limited to investigate some of the aspects of the Kaye effect or leaping shampoo, a spectacular phenomenon which is only partially understood.
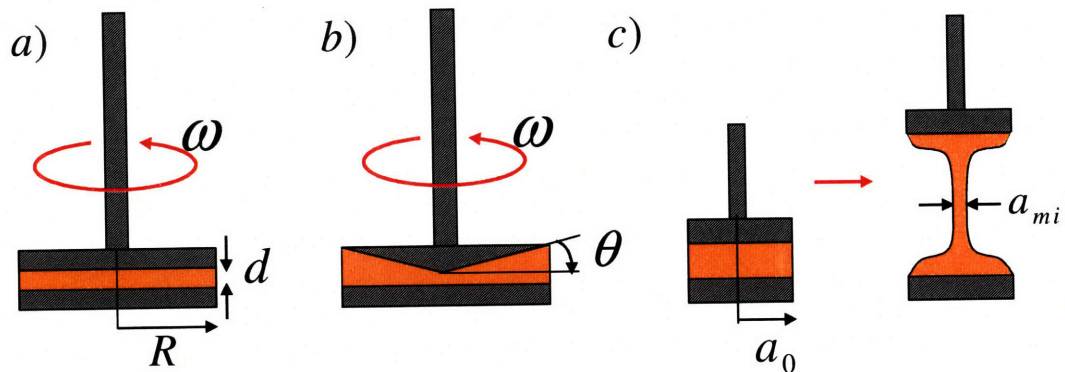
Figure 3-1: a) Diagram of small amplitude oscillatory shear rheology in plate-plate geometry b) Diagram of small amplitude oscillatory shear rheology in cone-plate geometry c) Diagram of Capillary Breakup Extensional Rheology (CaBER).

3.1.2 Shear and extensional rheology tests

Small amplitude oscillatory shear

Small amplitude oscillatory shear rheology tests are easy to set up and to analyze through simple physical models. In the simplest geometry, called the plate-plate geometry (figure 3-1 (a)), the sample, which could be a fluid or a soft solid, is loaded between two plates. An oscillatory shearing motion is imposed on the sample by imposing either an oscillatory angular displacement or torque on one of the plate. The rheometer measures the corresponding sample response, respectively the torque or the displacement. Experiments on homogeneous single-phase fluids are usually conducted with a plate-cone geometry (figure 3-1 (b)), where the use of a truncated cone in place of one of the plates creates a shear rate that is approximately constant throughout the sample. Other geometries such as Couette cells allow the investigation of complex or low viscosity fluids that would otherwise be difficult to analyze in the simplest geometries. The information provided by small amplitude oscillatory shear tests is the magnitude of the in-phase and out-of phase components of the sample response with respect to the input, as a function of oscillation frequency.

For example, if one impose an oscillatory deformation $\gamma(t) = \gamma_0 \sin(wt)$, the fluid response
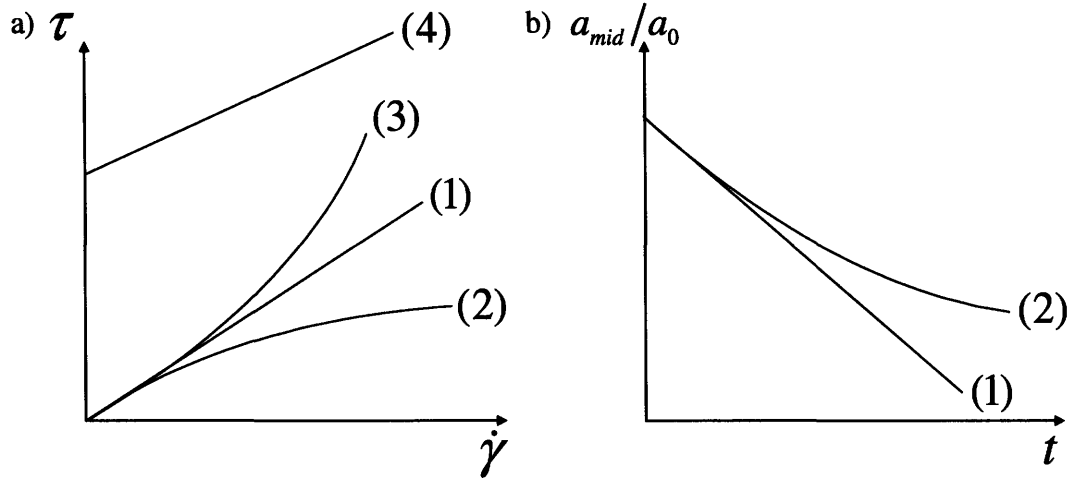
Figure 3-2: Schematic typical result of rheological tests on several class of fluids. a) Typical result of steady shear rheology tests on Newtonian fluids (1), shear-thinning fluids (2), shear-thickenning fluids (3), and fluids with a yield stress. b) Typical results of CaBER tests on Newtonian fluids (1) and dilute polymer solutions (2).

is the stress $\sigma(t)$, which in the linear limit can be written $\sigma(t) = G' \sin(wt) + G'' \cos(wt)$. G' and G'' are respectively called the storage and loss moduli, as they represent the amount of energy respectively stored elastically and lost through viscous dissipation. In addition, the dependency of $G'(w)$ and $G''(w)$ with the oscillation frequency also gives valuable insights into the fluid properties. Purely elastic materials are characterized by $G'' = 0$, whereas purely viscous, Newtonian fluids are characterized by $G' = 0$. In the simple Maxwell model for viscoelastic fluids, the fluid response is modelized by a spring of modulus G_0 and a dashpot of viscosity $\eta_0 = G_0\lambda$ in series. In this model, λ is an important parameter with the dimension of a time: it is called the characteristic relaxation time of the fluid, and has a critical importance in the onset of non-Newtonian phenomenon. In this model, G' and G'' are simply given by

$$G'(w) = G_0 \frac{(\lambda w)^2}{1 + (\lambda w)^2} \tag{3.1a}$$

$$G''(w) = G_0 \frac{\lambda w}{1 + (\lambda w)^2} \tag{3.1b}$$

Experimentally, it is very simple to find λ with fluids following the Maxwell model: the curves of $G'(w)$ and $G''(w)$ cross for $w = 1/\lambda$.

Steady Shear

Steady shear tests often use the cone-plate geometry, but impose a continuous, unidirectional shear on the sample. What is tested is not the linear viscoelastic response but the fluid viscosity as a function of the shear rate $\dot{\gamma}$ or shear stress τ imposed. In the case of the cone-plate geometry, the shear rate is given by the rotation frequency ϖ and the small cone angle θ by $\dot{\gamma} = \varpi \sin(\theta) \simeq \varpi\theta$. Note that in the cone-plate geometry the shear rate is independent of the radius. For the plate-plate geometry, the shear rate depends on the radial distance r, with $\dot{\gamma}(r) = rR/d$. The viscosity is simply given by $\eta = \tau/\dot{\gamma}$.

In the case of Newtonian fluids, the viscosity is constant and is commonly denoted η_0 (figure 3-2 (a) line (1)). Fluids for which the viscosity decreases with shear rate are called shear-thinning (figure 3-2 (a) line (2)). Most dilute polymer solutions have a plateau viscosity at low shear rate, and are shear-thinning at high shear rate. The critical shear rate is often found to be $\dot{\gamma}_c = 1/\lambda$, which can also be written as the critical dimensionless Weissenberg number Wi $= \dot{\gamma}_c \lambda = 1$. It is also possible that the viscosity is constant at η_0 under a given critical shear stress, and drops by many orders of magnitude above this shear stress. In terms of shear rate, this means that the viscosity approaches a plateau below a given shear rate and decreases like $\eta \sim 1/\dot{\gamma}$ above this rate. In that case, the shear stress is approximately constant during the shear-thinned portion and is equal to $\tau_c = \eta_0 \dot{\gamma}_c$. If the viscosity increases with the shear rate, such as concentrated suspension of corn starch, the fluid is said to be shear-thickening (figure 3-2 (a) line (3)). For materials with a yield stress, the viscous stress increases with the shear rate in an affine fashion $\tau = \eta_0 \dot{\gamma} + \tau_c$ where τ_c is the yield or critical stress (figure 3-2 (a) line (4)).

CaBER

Capillary Breakup Extensional Rheology (CaBER, figure 3-1 (c)) experiments provide insights in the transient extensional behavior of fluids, which may be very different from the shear rheology in the case of non-Newtonian fluids[7]. The fluid sample is initially loaded between

two circular plates. Then, an elongational step strain is imposed to the fluid, by quickly raising the top plate (usually in 30 to 50 ms). The fluid forms a liquid bridge between the two plates, which thins under the influence of surface tension. The thinning process is balanced by viscous resistance, and, in the case of viscoelastic fluids, by elastic stresses in the elongating filament. The mid-filament radius a_{mid} is measured by a laser micrometer, which gives the local extension rate[7]

$$\dot{\epsilon} = -\frac{2}{a_{mid}} \frac{da_{mid}}{dt} \tag{3.2}$$

The local and time-dependent extensional viscosity η_E is defined by the approximate force balance[7]

$$\dot{\epsilon}\eta_E \simeq \frac{\sigma}{a_{mid}} \tag{3.3}$$

Combining (3.2) and (3.3) leads to a simple measurement for the extensional viscosity[7]

$$\eta_E = -\frac{\sigma}{2\frac{da_{mid}}{dt}} \tag{3.4}$$

For Newtonian fluids, Trouton[53] showed that the extensional viscosity is constant and is simply given by kinematic considerations by $\eta_E = 3\eta_0$. The ratio η_E/η_0 is called the Trouton ratio, and is equal to 3 for Newtonian fluids. In this case, substituting this constant viscosity in (3.4) leads to the result that the mid-filament radius thins linearly (figure 3-2 (b) line (1)),

$$\frac{a_{mid}(t)}{a_0} = 1 - \frac{t}{t_{visc-cap}} \tag{3.5}$$

where a_0 is the initial radius and $t_{visc-cap}$ is a time characteristic of the visco-capillary thinning process . The precise expression for this timescale is given by Papageorgiou[11]:

$$t_{visc-cap} = 14.1 \frac{a_0 \eta_0}{\sigma} \tag{3.6}$$

While the shear and extensional viscosity are directly related one to each other for Newtonian fluids through the Trouton ratio, the case of non-Newtonian fluids is more complex, not only because their extensional behavior can be dramatically different from Newtonian fluids, but also because it is often not correlated with shear rheology. A well-known example of such non-

Newtonian extensional behavior is the extreme extension-strengthening of polymer solutions, up to the point that many polymers like Nylon can be drawn into fibers. Extension-strengthening is often caused by the alignment and extension of polymer molecules along the flow that creates an additional elastic stress that helps resisting the extension[15]. Additional phenomenon such as solvent evaporation, because of the diverging area-to-volume ratio, and intermolecular secondary interactions, may also increase the jet resistance to extension. On the other hand, yield stresses or extension-thinning behaviors would accelerate breakup. As a result, two fluids can have a misleadingly close shear behavior and be very different in extension. For example, among the test fluids that are presented below, CPyCl solutions and commercial shampoos have a similar behavior in shear (both are shear-thinning) but, in CaBER experiments, the former tends to form long threads while the latter breaks faster (because of differences in extensional viscosity).

Among the possible types of non-Newtonian flow behaviors, the extensional response of viscoelastic fluids in CaBER experiments has been described by Entov and Hinch[54] and studied by Anna and McKinley[14]. After the first phase of viscous thinning, the ever-increasing extension rate become larger than the polymeric relaxation rate. The molecules are stretched by the flow, leading to elastic stresses and a new elasto-capillary balance. The Trouton ratio becomes very large, typically several orders of magnitude larger than for Newtonian fluids, and the radius thins exponentially[54] as

$$\frac{a_{mid}(t)}{a_0} \sim e^{-t/3\lambda} \tag{3.7}$$

Therefore the characteristic breakup or thinning time scales as λ, the elastic relaxation time (figure 3-2 (b) line (2)). A thin thread is formed that resists the capillary thinning process. Ultimately, depending on the fluid properties as well as the rate of solvent evaporation compared to the thinning rate, it eventually breaks up or forms a solid fiber, as in fiber-drawing[15].

3.1.3 Rheological properties

We now cover the different rheological tests applied to the test fluids in order to characterize them. The linear viscoelastic properties were performed on all fluids on an ARG2 rheometer,

in a cone-plate geometry of 40 mm diameter, at 22.5^oC. We obtain the values of important fluid parameters such as the zero-shear rate viscosity η_0 and the characteristic relaxation time λ, which are summarized in Table 3.1.

Micellar fluid

Shear Rheology The CPyCl solutions exhibited a strong viscoelastic behavior, that is well characterized in oscillatory experiments at low frequencies by a single-mode Maxwell model as figure 3-3 (a). The relaxation time λ in this model is directly related to the characteristic times of the stress relaxation processes in wormlike micellar solution, reptation (λ_r) and breakup (λ_b) as shown in equation (2.19).

All the solutions were also strongly shear-thinning (figure 3-3 (b)), which translates into a clear critical or plateau shear stress (figure 3-3 (c) shows the example of CPyCl 100). This plateau stress corresponds to the stress level that is sufficient to break the intermolecular bonds holding the surfactant molecules in the wormlike micelles, leading to their breakup in smaller aggregates. This apparent strong shear-thinning, with $\eta \sim 1/\dot{\gamma}$, actually signals the onset of shear banding, as predicted by Spenley and co-workers[55] and verified by Berret and co-workers[56]. As can be seen on figure 3-3 (b), below the critical shear rate of the order of $\dot{\gamma}_c \simeq 1/\lambda$, CPyCl solutions show a plateau or zero-shear-rate viscosity, which is the value reported in Table 3.1.

Another non-Newtonian effect is the first normal stress difference that arises because the shear flow tend to align the wormlike micelleswhich leads to a streamline tension resulting in a normal stress difference[41]. The figure 3-3 (d) shows that the first normal stress difference increases approximately linearly with the shear rate. At low shear rate, where the first normal stress difference is expected to scale quadratically with the shear rate[41], the measured value are below the sensitivity threshold of the ARG2 rheometer.

Extensional rheology The sequence of snapshots shown on figure 3-4 a shows a typical CaBER experiment conducted on a CPyCl 100 solution. The diameter of the plates is 6mm, and they are initially separated by 1.2mm. A step-strain is imposed, pulling the plates apart in 50ms to 4.8mm, which represent a Hencky strain $\epsilon = \ln(4.8/1.2) = 1.4$.
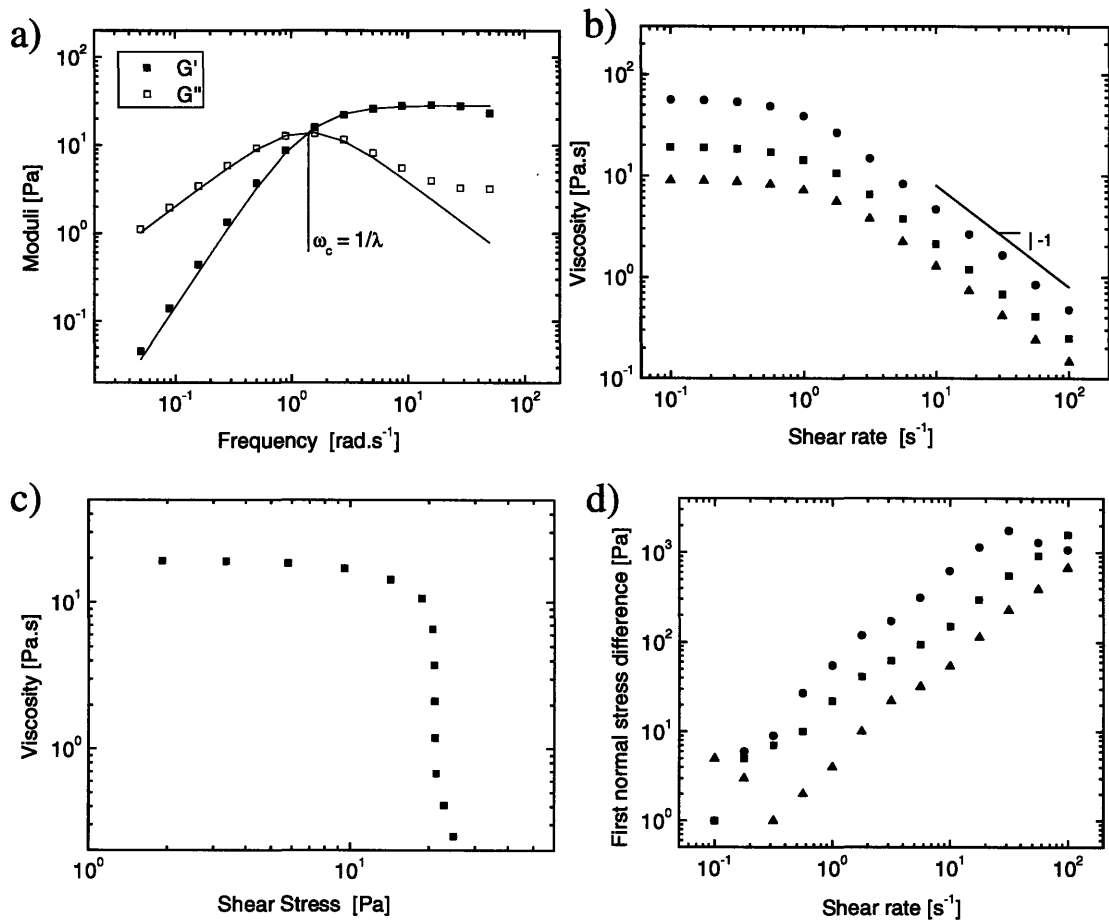
Figure 3-3: Rheological properties of micellar solutions. a) Small amplitude oscillatory test on CPyCl 100, fit by a single-mode Maxwell model (similar fit were found for CPyCl 75 and CPyCl 150) b) Steady shear viscosity of CPyCl 75 (▲), CPyCl 100 (■) and CPyCl 150 (●), as a function of shear rate. c) Steady shear viscosity of CPyCl 100, as a function of shear stress. d) Steady shear first normal stress difference as a function of shear rate.

a) $a_0 = 3\,mm$

Initial state $t = 0$ $t = \dfrac{1}{4}\tau_{\text{Break}}$ $t = \dfrac{1}{2}\tau_{\text{Break}}$ $t = \dfrac{3}{4}\tau_{\text{Break}}$
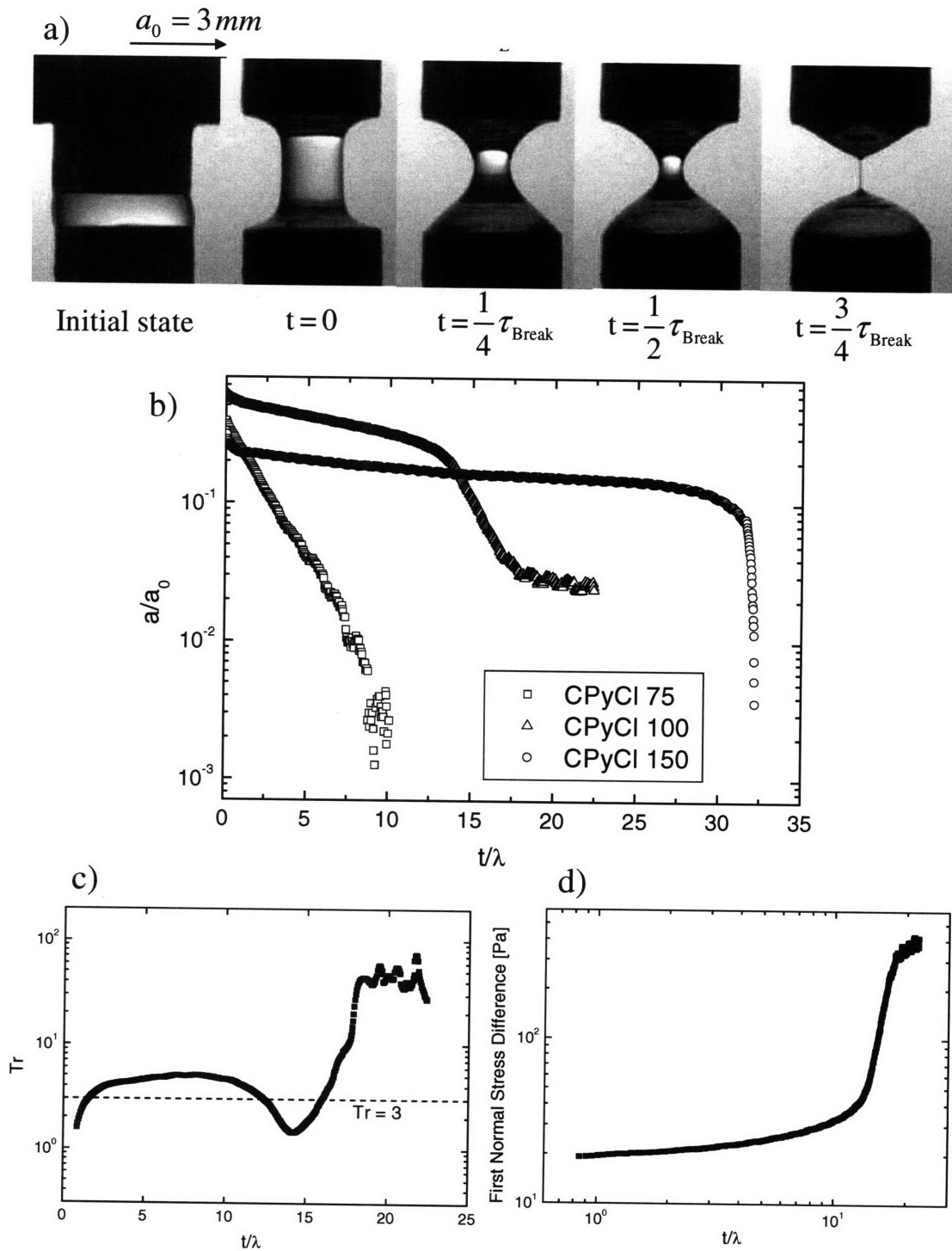
Figure 3-4: Capillary Breakup Extensional Rheology (CaBER) experiments, with plates of 6mm of diameter and a imposed Hencky strain of 1.4 a) Side view of an experiment with CPyCl 100. $\tau_{Break} = 15.8\ s$. b) Evolution of the diameter against time scaled by the solution relaxation time measured in shear and reported in table 3.1, for CPyCl 75, 100, 150. Each solution behave in a qualitatively different fashion. c) Trouton ratio for CPyCl 100. d) First normal stress difference for CPyCl 100

40

As shown in figure 3-4 (b), the three solutions behave in a qualitatively different pattern in this experiment. CPyCl 75 has such a small viscosity that it almost immediately enters an regime of elasto-capillary exponential thinning. At the other end of the spectrum, CPyCl 150 is almost gel-like, and the liquid filament is sustained for an extended period of time. Breakup eventually occurs but usually not at the midplane[50], thus the typical analysis used in CaBER is not applicable. The CPyCl 100 fluid shows the most interesting pattern for our jetting experiment of a viscoelastic fluid with strong non-Newtonian effects, although with a viscous component allowing jets to form and flow.

The first part of the thinning is dominated by a balance between capillary and viscous effects. The midplane diameter thins linearly in time. As this diameter decreases; the extension rate increases, until it starts triggering non-Newtonian effects. The wormlike micelles become increasingly aligned by the extension flow, building up elastic stresses, which lead to extension-thickening. The Trouton ratio $Tr = \eta_E/\eta_0$ versus time is plotted in figure 3-4 (c). The main features are the Newtonian behavior ($Tr = 3$) during the first part of the experiment, and the extensional thickening ($Tr > 30$) that follows. Since thin filaments and very large extension rates are required for extension-thickening to take place, it will only play a limited role in jetting experiments described in Chapter 4. More precisely, extensional viscosity will be only taken in account near the jet breakup limit, at low flow rates, and the precise criteria for this limit will be derived below in Chapter 5.

Temperature dependence The rheological properties of wormlike micelles solutions are very dependent on temperature, for two reasons. The first one is the evolution with temperature of the two characteristic timescales of the relaxation processes, λ_r and λ_b. λ_r refers to the reptating motion of the chain segments and λ_b represents a thermally-activated breakup process. Everything else held constant, both decrease exponentially with temperature. The second source of dependency is the variation of the characteristic length of the micelles, which are dynamic structures. Their average length depends exponentially on the thermally-activated processes of association/dissociation of the surfactant molecules at the ends of the micelles[49]. This affects λ_r through a power law dependency according to the reptation theory of de Gennes[48]: if we denote L_e the characteristic length of the micelles, λ_r scales as $L_e^{3.4}$. The
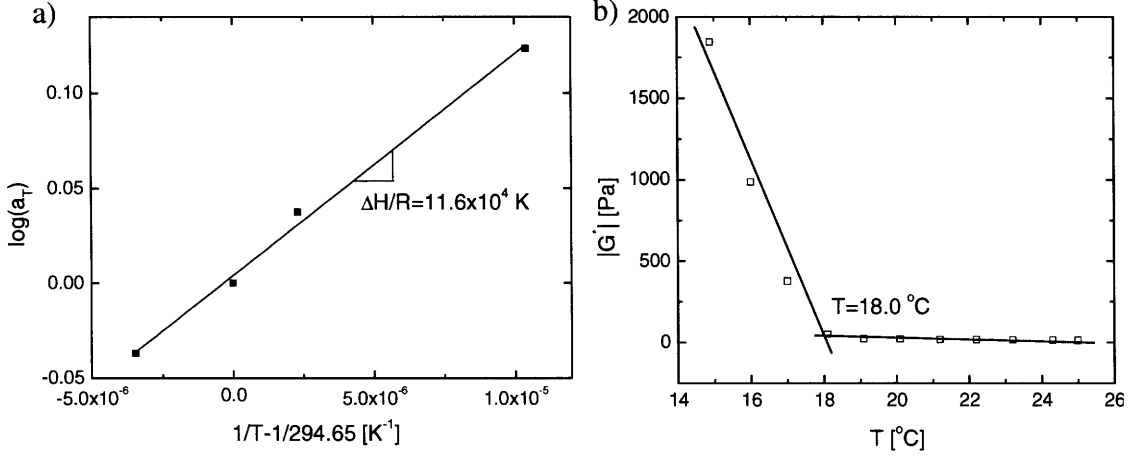
Figure 3-5: Temperature dependence of CPyCl 100. a) Shift factors with $T_{ref} = 294.65\ K$. b) Krafft transition at $T = 18^oC$ shown as change of slope of the complex modulus $|G^*| = \sqrt{G'^{\ 2} + G''^{\ 2}}$ as a function of T, in an oscillatory shear experiment at a frequency of $1\ \mathrm{s}^{-1}$

temperature dependency of both timescales are compounded into λ, the Maxwell model fit parameter of figure 3-3 (a), through the connection given by equation (2.19) $\lambda = (\lambda_r \lambda_b)^{\frac{1}{2}}$.

The temperature dependency of λ can be fitted with an Arrhenius equation of the form

$$\lambda(T) = \lambda_T = \lambda_{Tref} \exp\left(\frac{\Delta H}{R}\left(\frac{1}{T} - \frac{1}{T_{ref}}\right)\right) \tag{3.8}$$

The ratio $a_T = \lambda_T / \lambda_{Tref}$ is called the shift factor. In figure 3-5 (a) we show with $T_{ref} = 21.5^\circ C$ that the temperature dependency of the shift factors follows the Arrhenius model with a very large activation energy. This in turns leads to a large temperature dependency of the viscosity of the fluid.

In first approximation, the viscosity of a viscoelastic fluid such as CPyCl 100 is related to its elastic modulus and longest relaxation time by $\eta_0 = G_0 \lambda$. Provided that the length of the micelles is long enough for them to entangle, the elastic modulus depends mostly on the surfactant concentration. Rubber elasticity theory suggests that G_0 varies only linearly with temperature[57]. An estimate of G_0, the norm of the complex modulus $|G^*| = \sqrt{G'^{\ 2} + G''^{\ 2}}$,

42

is indeed found to be approximately constant with temperature, as can be seen on the right-hand side of figure 3-5 (b). As a result, the zero-shear-rate viscosity of the solution varies exponentially with temperature. This is experimentally found to be true, with an exponential factor of the same order as the elastic relaxation time. CPyCl 100 viscosity drops from 25.2 Pa.s at $20°C$ to 9.3 Pa.s at $25°C$. This means that in order to get meaningful experiments with this type of fluid, the temperature must be either carefully controlled, or measured for each experiment in order to adapt the fluid properties in accordance with equation (3.8).

Another effect of the temperature can be seen in capillary breakup and filament stretching experiment, as well as during the breakup of the jet falling on a plate at very low flow rate. In these cases, the liquid, initially transparent at ambient temperature $(22\text{-}23°C)$, becomes white. Direct temperature measurement with a thermocouple immersed in the small mound of white liquid falling on the bottom plate shows that its temperature can be as low as $16°C$. This suggests the explanation that the whitening is caused by the Krafft transition, that is, the precipitation of surfactant from the solution when the temperature becomes lower than a critical temperature called the Krafft temperature[58]. The Krafft temperature is not to be confused with the Krafft point, which is a temperature that depends on concentration, at which the surfactants start assembling into micelles. The Krafft temperature can be measured either by visual observation of turbidity or by the drastic change in most physical properties when the precipitation occur. Figure 3-5 (b) offers one example of such measurement, with the abrupt change of the slope of the norm of the complex modulus $|G^*|$ in a small-oscillation test when plotted against T. This leads to a Krafft temperature for CPyCl 100 of 18.0^oC, which is consistent with estimates from direct visual observations.

The cooling in itself is likely due to the evaporative cooling of water, which has a strong effect on the temperature of thin filaments because of their diverging area to volume ratio. The smaller radius also increases the local capillary pressure, which is turn make the chemical potential of the solvent higher and accelerates evaporation. Another possibility connecting evaporation and visual appearance of turbidity could simply be that the filament dries, leaving only solid surfactant. In any case, these extreme cooling and drying effects tend to appear only the limit of very large jet height and low flow rates (for example $H = 25$ cm, $Q = 2$ mL/min).
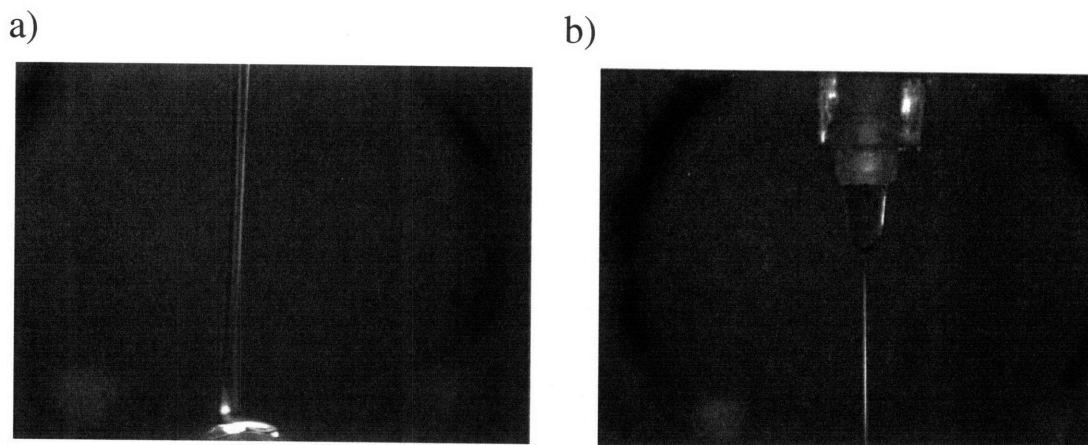
a)

b)

Figure 3-6: Jets of CPyCl 100 from a height of $H = 4$ cm observed through crossed polarizers. a) Continuous jet ($Q = 3$ mL/min), mostly black except for some effects of curvature: there is little alignment of the micelles along the flow. b) Thin micellar filament just before breakup. The filament whitens, suggesting a significant alignement of the micelles under the strong extensional flow.

Nevertheless, even out of the range of whitening transition, evaporation-driven cooling and concentration increase leads to large increase in viscosity when the residence time of a fluid particle in the jet becomes of the order of the typical time for the temperature change to take place. In other words, as the height of fall increases and the flow rate decreases, the variability in the local viscosity increases.

Birefringence A way to directly visualize the non-Newtonian properties of wormlike micellar solutions is to look at them through crossed polarizers. This experimental technique reveals the difference between isotropic regions and zones with a significant level of order in transparent materials placed between the polarizers. Isotropic zones remain black, whereas the ordered zones appear brighter as the degree of order increases. Therefore, observing micellar jets through crossed polarizers can reveal whether a significant orientation and alignment of the micelles by the flow takes place[46]. The large photo-elastic coefficient of wormlike micellar solutions[59] allows good results with minimal experimental constraints. Nevertheless, in the case of jets of circular cross-section, this technique is limited to qualitative understanding of the wormlike alignment process in extension flow, because curvature effects are difficult to take into account
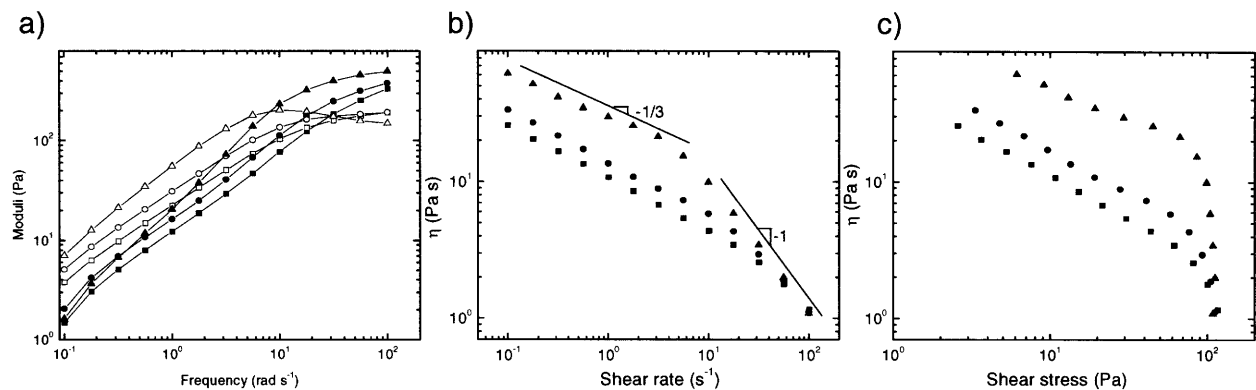
Figure 3-7: Shear rheology experiments on three industrial shampoo bases with various amount of salt. ■ SB 1.5 ● SB 1.8 ▲ SB 2.7. a) Small amplitude oscillatory shear experiments. Full symbols: G'. Empty symbols: G" b) Steady shear experiments: viscosity against shear rate c) Steady shear experiments: viscosity against shear stress. Experimental results are gathered in table 3.1.

quantitatively[60].

The images in figure 3-6 show two examples of birefringence experiments. Figure 3-6 (a) shows a jet from a moderate height ($H = 4$ cm) and a sufficient flow rate ($Q = 3$ mL/min) so that acceleration of gravity is negligible with respect to the velocity of the flow. The image is essentially dark, except for some effects of curvature near the jet edges, which is a hint that little ordering is taking place. The extension rate $\dot{\epsilon}$ is of the order of $Q/\pi a_0^2 H = 0.17$, and from CaBER experiments (figure 3-4) the extensional viscosity at that extension rate is similar to what would be observed for a Newtonian fluid, with $Tr \approx 3$. Figure 3-6 (b), on the opposite, shows a very white and bright thin filament. In this case, extension-strengthening is at its maximum, and elastic stresses resist the filament breakup.

Shampoo bases

The three shampoo bases SB 1.5, SB 1.8, SB 2.7 display weak non-Newtonian effects. SAOS experiments (figure 3-7 (a)) show that the characteristic relaxation time for each solution is significantly shorter than for CPyCl solutions. Unlike the CPyCl solutions, the shampoo bases could not be fit satisfactorily by a single-mode Maxwell model, and required a multiple-mode
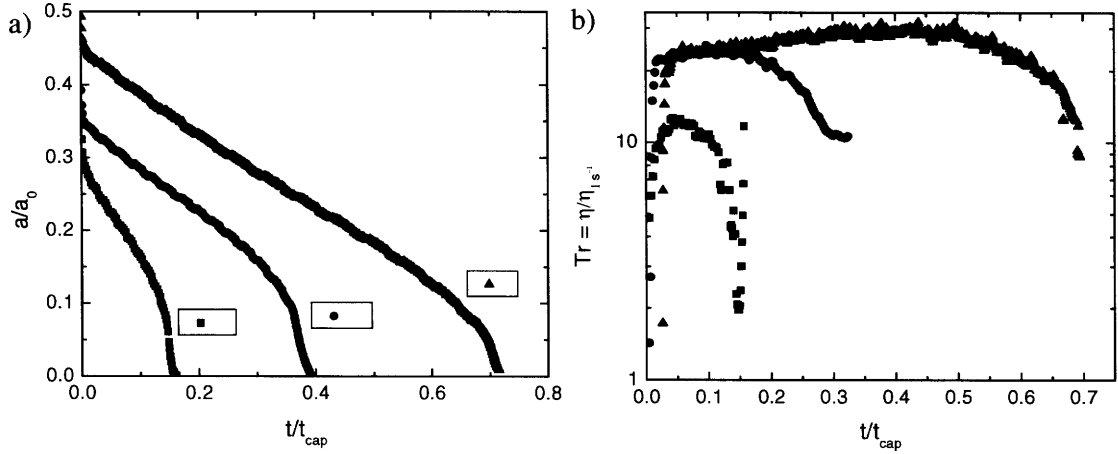
Figure 3-8: Shear rheology experiments on three industrial shampoo bases with various amount of salt. ■ SB 1.5 ● SB 1.8 ▲ SB 2.7. a) Midplane diameter as a function of time b) Trouton ratio as a function of time.

analysis. The fit given by TA Analysis software used six modes, with a set of relaxation times λ_i and the associated modulus G_i. The characteristic time λ reported in Table 3.1 is the weighted average $\lambda = \sum \lambda_i G_i / \sum G_i$. The fact that shampoo bases are complex fluids with many more components than CPyCl solutions explains why this more complicated analysis is required, nevertheless, shampoo bases remain qualitatively similar to weakly viscoelastic fluids such as dilute polymer solutions. For example, the value of $1/\lambda$ is of the order of the crossover between the storage and loss moduli curves on figure 3-7 (a).

Steady shear experiments show that the shampoo bases are shear-thinning fluids, for which the viscosity does not plateau even at the lowest shear rates attainable in the ARG2 rheometer. The three shampoo bases used here show consistently that the viscosity scales as $\eta \sim \dot{\gamma}^{-1/3}$ at low shear rates, and $\eta \sim \dot{\gamma}^{-1}$ once they reach a critical shear rate (figure 3-7 (b)). The critical shear rate is of the order of $1/\lambda$, as expected. As the salt content of each solution increases, the viscosity increases, a behavior likely due to the increase in length of the micellar structures as salt screens the repulsive interactions between the surfactant head groups. In terms of shear stress, all solutions have a critical shear stress close to 100 Pa (figure 3-7 (c)), which is once again understood as the critical stress at which the average micellar structures are broken.

46

CaBER experiments show that all solutions behave as expected for Newtonian fluids. The midplane radius thins linearly in time, without forming a long-lasting filament (figure 3-8 (a)), and with no significant extension-strengthening (figure 3-8 (b)). This, along with the very short relaxation times observed in shear rheology, suggests that the micellar structures within the shampoo bases are much shorter than for CPyCl solutions.

The fact that shampoo bases do not reach a plateau viscosity at low shear rates means that it is difficult to define a characteristic viscosity that could be used in dimensional analysis. A solution is to arbitrarily choose the viscosity for a shear rate of $1s^{-1}$, at which none of the solutions has reach the critical stress. This is the viscosity $\eta_{1s^{-1}}$ that is reported as characteristic viscosity in Table 3.1.

Reference fluids

Figure 3-9 shows shear and extensional properties for two comparison fluids used in this study as baselines to which CPyCl solutions and shampoo bases are compared. One is silicone oil, a purely Newtonian fluid, and the other one is a Boger fluid, a dilute solution of high molecular weight polymer that does not shear-thin. Figure 3-9 (a) shows the steady shear rheology of both fluids which, as expected, have a constant viscosity. In addition, it can be noted that both are fairly viscous fluids, with values of viscosity of the same order as CPyCl 100, which make them suitable for jetting experiments. Figure 3-9 (b) shows the evolution of midplane diameter in CaBER experiments for both fluids, which are typical of the two rheological categories. The silicone oil filament thins linearly in time, as expected from (3.5), while the Boger fluid is fitted by an exponential curve. The fitting parameter is the elastic relaxation time given in Table 3.1, and is much larger than for CPyCl solutions or shampoo bases.

Commercial shampoos

Figure 3-9 (c) shows rheological properties of two different shampoos. Despite being from different brands, and of different types (one is a shampoo only, the other one is shampoo and conditioner) they have very similar rheological properties in shear. They are both moderately viscous fluids, with strong shear-thinning behavior ($\eta \sim \dot{\gamma}^{-1}$, which is related to a plateau shear stress of the order of $\eta_0 \lambda$) starting at a similar shear rate. It is likely that both formulation
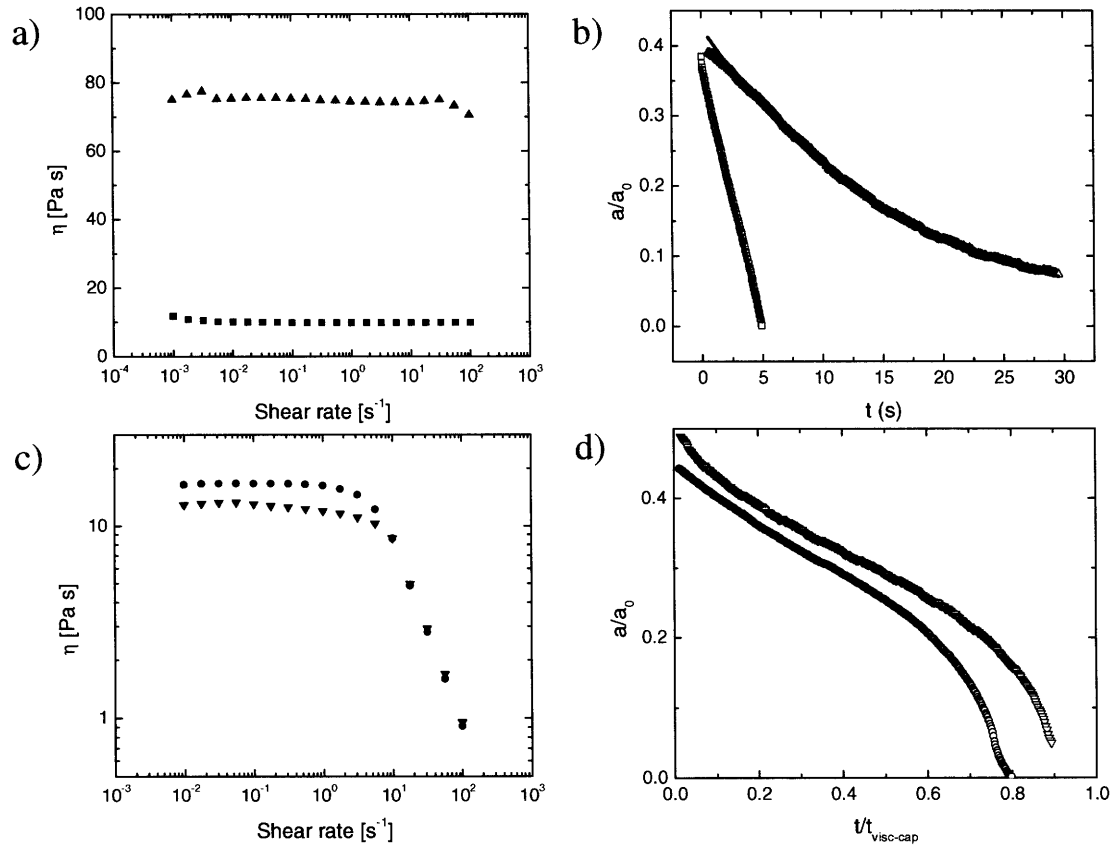
Figure 3-9: Rheology data for Boger fluid (▲), silicone oil T41 (■), Herbal Essence shampoo (●) and Pantene ProV shampoo (▼). a) Steady shear data, showing that both Boger fluid and silicone oil are highly viscous and not shear-thinning. b) Caber experiment, with a linear fit for silicon oil and exponential fit for Boger fluid, with the fit parameter $\lambda = 5.48$ s. c) Steady shear data, showing that both commercial shampoos have very similar shear rheology, and are strongly shear-thinning after a plateau viscosity. d) Caber experiment on commercial shampoos, showing very similar pattern after rescaling.

have been adjusted in a similar fashion with additives in order to meet identical consumer preferences.

Caber experiments on commercial shampoos (figure 3-9 (d)) do not discriminate between the shampoos as well. Once scaled for the slight difference in zero-shear viscosity, both experiments show a very similar pattern. The midplane radius thins linearly with time as Newtonian fluids do, and show an acceleration of thinning just before breakup. This can be connected to the shear thinning properties of both shampoos: as the radius thins, the extension rate increases, until it reaches the point where the viscosity of the shampoos drop, leading to an acceleration of thinning.

CPyCl solutions	CPyCl 75	CPyCl 100	CPyCl 150
λ (s)	0.606	0.722	0.898
η_0 (Pa.s)	8.98	18.8	54.0
E_g	13.3	12.4	10.9
Shampoo bases	**SB 1.5**	**SB 1.8**	**SB 2.7**
λ (s)	0.118	0.146	0.193
$\eta_{1s^{-1}}$ (Pa.s)	10.8	13.5	29.6
E_g	2.45	2.80	2.86

Reference fluids	silicone oil	Boger fluid
λ (s)	0	5.48
η_0 (Pa.s)	99.7	751
E_g	0	59.9
Commercial shampoos	**Herbal**	**Pantene**
λ (s)	0.0707	0.0479
η_0 (Pa.s)	16.7	12.8
E_g	1.27	0.940

Table 3.1: Rheology data for the three CPyCl solutions and the three comparison fluids used at 22.5 $^\circ$C.

3.2 Experimental setup for jet analysis

Two setups were used for the jetting studies in this research. The first setup simply involves the fluid being pumped to a nozzle, from where the jet falls onto a plate. Direct observation
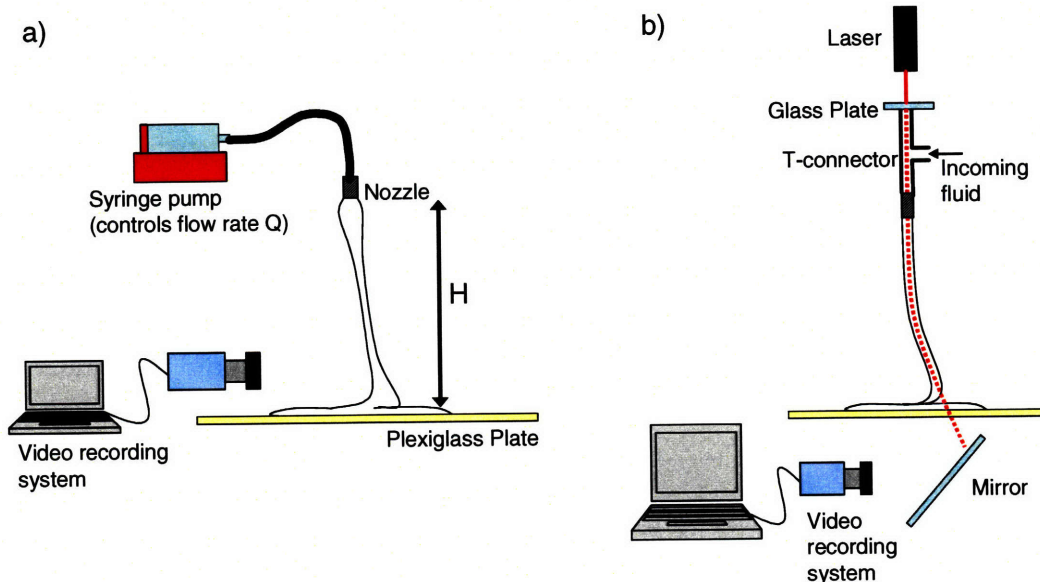
Figure 3-10: Experimental setups. a) Experimental setup for regime diagram and quantitative measurements. b) Experimental setup for trajectory visualization.

of the jet profile and dynamics is sufficient to obtain the flow regime, and a video camera is used for quantitative measurements. The second setup is more subtle and helps to precisely understand the motion of the jet, by using a laser shining along the jet. Several problems that prevented this second setup from providing accurate quantitative measurements are discussed along with the description. Another point discussed in this section is the precise definition and possible variants of the bottom plate condition.

3.2.1 Direct observation

The fluid is pumped by a Stoelting flow rate controller from a 60 mL syringe through a flexible plastic tube into a nozzle. The nozzle is attached vertically to a vertical-axis stage controller, and the liquid falls onto a plate below the nozzle (figure 3-10 (a)). The plastic tube is approximately 20cm long, which leads to a residence time of fluid particles in the tube between 10 and 20 secondes, exceeding greatly the relaxation times listed in Table 3.1. This ensures the relaxation of any stress occurring at the exit of the syringe. We mostly report results obtained with a

circular nozzle of diameter $a_0 = 1.25$ mm, but the influence of the nozzle radius as also been investigated with two additional sizes, $a_0 = 0.775$ mm and $a_0 = 2.40$ mm. The behavior of the jets has been recorded using a BlueFox digital videocamera at a frame rate of 30 to 50 fps. Frequency measurements were done by frame counting, and amplitude measurement were done with the image analysis software ImageJ using an image of a ruler as reference. A high-speed videocamera Phantom V from Vision Research has been also used to capture rapid phenomena such as jet breakup and the Kaye effect, at frame rates of 500 to 800 fps.

3.2.2 Trajectory tracking with laser

Another setup was used to follow the trajectory of the jet, inspired from an experimental technique used by Versluis[39]. A red laser beam shines through the jet using a T-shape nozzle and is guided along the jet like in an optic fiber (figure 3-10 (b)). A camera records it through the bottom plate, using a mirror at a 45° angle, and an image analysis code then evaluates the precise position of the spot. The technique allows for the qualitative understanding of the trajectory of the jet in folding motion, including the tracking over many periods that reveals the stability of the folding regime. Its shortcoming are that the liquid jet is an imperfect waveguide, and therefore let the laser beam shine through the free surface of the jet when the angle of incidence is too large, which happens at large amplitude. On the other hand, at small amplitude, the jet motion does not affect the position of the laser spot. This means that quantitative measurements from these experiments could not be obtained.

3.2.3 Discussion of the bottom-plate condition

Two questions regarding the bottom-plate conditions must be addressed to ensure that the problem is correctly defined. First of all, the jet does not fall directly on the plate, but on a thin layer of fluid that is covering the plate. We are only interested in well established regimes, for which the jet falls on a layer of fluid, as opposed to the jet falling on a clean plate that is transitory. The thickness of that layer is "chosen" by the fluid, to balance the viscous stresses between the upper, free layer and the no-slip plate-fluide interface with the incoming flow rate. This thickness is taken in account in the measurement of the height of fall, which is defined as the distance between the fluid layer and the nozzle. The spreading fluid is either allowed to

fall in a secondary reservoir when it reaches the end of the plate, or the plate is cleaned before being totally covered.

The second point is that other geometries than the plate could be envisioned and be relevant to industry. The jet could fall on a bath of the same or of a different fluid, on an inclined plane, or on a curved surface. Different plate sizes or evacuation mechanisms could also influence how fast the fluid layer drains into the secondary reservoir. In the present study, we are interested in planar geometries. The evacuation mechanism does not play a significant role, because of the fact that the layer thickness is taken into account for the measurement of the height of fall, and the short duration of the measurement. The liquid bath, in the end, is the only alternative that could lead to dramatically different behavior such as air entrainment[17], at least at large incoming speed. Nevertheless, for the moderate jet speeds involved in most parts of the parameter space studied in this thesis, all phenomenon of interest such as jet motion occur on timescales shorter than the spreading time for the viscous fluids used. As a result, the jet dynamics studied in our experiments always take place on a small mound of fluid that has not spread completely.

Chapter 4

Experimental Results

The experimental exploration in this chapter aims at understanding the specific aspects of non-Newtonian jets, and is based on a dimensional analysis that helps in comparing one experiment to another. After describing the dimensionless variables characterizing the experiments, two types of results are presented. First of all, a qualitative description of the different flow regimes is important because some of these types of flow are new with respect to the existing studies on Newtonian fluids. These regimes are mapped onto the space of dimensionless parameters, with special attention to transitions between flow regimes, and compared to theoretical expectations for Newtonian fluids. The second type of result is the quantitative measurements of jet shape and motion in order to understand some of the novel and specific features of non-Newtonian jets.

4.1   Dimensional analysis

4.1.1   Purpose

Dimensional analysis is the process of identifying a set of relevant variables (experimental parameters, fluid properties, measurement outputs) of the problem, and combining them in order to *scale* them and compare their relative importance in a systematic way. This means nondimensionalizing the variables with relevant, characteristic values for the problem. This allows direct comparison between different experiments with different fluids, as well as the derivation of meaningful scaling laws. Without this step, the relevance of experimental or

theoretical results would be confined only to the precise set of experimental conditions for which they were derived or measured.

The practical way to create a nondimensionalization scheme is to use Buckingham's Π-theorem[62]. With N independent variables expressed in terms of P fundamental physical dimensions, a set of $K = N - P$ dimensionless groups is sufficient to describe the experiment. The dimensionless groups can be done by any combination of the initial variables, although physically meaningful groups are more useful and understandable.

We use three types of variables (some of them will be defined later):

- The external parameters (figure 3-10 (a)):

    - The imposed flow rate Q (in m^3/s)

    - The height of fall H (in m)

    - The nozzle radius a_0 (in m)

    - The acceleration of gravity g (in m/s^2)

- The fluid properties (Table 3.1):

    - The fluid's kinematic viscosity ν_0 (in m^2/s)

    - The fluid's density ρ (in kg/m^3)

    - The fluid's characteristic relaxation time λ (in s)

    - The fluid's surface tension σ (in kg/s^2)

- The measured outputs (figure 2-1 (c) and (d). :

    - The jet radius above the swell a_1 (in m)

    - The jet radius after the swell a_2 (in m)

    - The amplitude of folding L (in m)

    - The frequency of folding f (in s^{-1})

We keep the notation R and Ω used in the literature, for example in [6], for respectively the radius and frequency of coiling. All variables being either expressed in terms of time, length, mass, or combinations thereof, we need $12 - 3 = 9$ dimensionless groups to characterize the experiments performed.

4.1.2 Nondimensionalization scheme

The first step is to define relevant (i.e., meaningfully related to processes taking place in the experiment) length and time scales with some of the variables, and use them to nondimensionalize the rest of the variables. The forces in balance along the flow in the jet (i.e. the *tail*, as localized in fig 2-1 (c) and (d)) are the gravity that tends to accelerate and stretch the jet, and viscosity that resists the process. This competition can be characterized by a time scale $t_{VG} = (\nu_0/g^2)^{\frac{1}{3}}$ and a length scale $l_{VG} = (\nu_0^2/g)^{\frac{1}{3}}$, where ν_0 is the zero-shear-rate kinematic viscosity. These scalings will typically be relevant as long as extension-strengthening does not happens, which is true in most cases (figure 3-4). On length and time scales larger than these estimates, the jet thins by an amount determined by the balance of the two forces. Therefore, it is reasonable to adimensionalize the experimental parameters with these scales to obtain dimensionless heights and flow rates:

$$H^* = \frac{H}{l_{VG}} = H \left(\frac{g}{\nu_0^2}\right)^{\frac{1}{3}} \tag{4.1}$$

$$Q^* = \frac{Q \, t_{VG}}{l_{VG}^3} = Q \left(\frac{g}{\nu_0^5}\right)^{\frac{1}{3}} \tag{4.2}$$

The ratio of the elastic relaxation timescale to this gravito-viscous timescale gives an elasto-gravitational number. Non-Newtonian effects arise in the jet when the stretch rate, driven by gravity and resisted by viscosity, becomes larger than the relaxation rate of the wormlike micelles. Therefore, the elasto-gravitational number characterizes the magnitude of these effects

$$E_g = \frac{\lambda}{t_{VG}} = \lambda \left(\frac{g^2}{\nu_0}\right)^{\frac{1}{3}} \tag{4.3}$$

In a similar fashion, the radius of the jet at points along its stream ($i = 0, 1, 2$) (as localized

in fig 2-1 (d)) can be scaled by the same length scale

$$a_i^* = \frac{a_i}{l_{VG}} = a_i \left(\frac{g}{\nu_0^2} \right)^{\frac{1}{3}} \tag{4.4}$$

In the folding regime, the dimensionless outputs to measure are scaled in the same fashion

$$f^* = f \, t_{VG} = f \left(\frac{\nu_0}{g^2} \right)^{\frac{1}{3}} \tag{4.5}$$

$$L^* = \frac{L}{l_{VG}} = L \left(\frac{g}{\nu_0^2} \right)^{\frac{1}{3}} \tag{4.6}$$

Capillary effects are characterized by the Ohnesorge number that has already been defined in (2.2):

$$Oh^{-2} = \frac{\sigma}{\rho} \frac{a_0}{\nu_0^2} = \frac{\sigma a_0 \rho}{\eta_0^2} \tag{4.7}$$

The nondimensional framework is now complete and sufficient with nine dimensionless groups (equation (4.4) defines three groups). Nevertheless, we can define additional relevant, although redundant, parameters: the Reynolds number defined in (2.1), and the aspect ratio, defined by

$$Re = \frac{Q}{a_0 \nu} = \frac{Q^*}{a_0^*} \tag{4.8}$$

and

$$\epsilon = \frac{a_0}{H} \tag{4.9}$$

The jets are slender body with $\epsilon \ll 1$. This dimensionless group will be mostly used in this thesis as a dimensionless height, under the form $\epsilon^{-1}/2 = H/2a_0$, reminiscent of equation (2.9a) and (2.9b).

Capillary thinning processes happening on a time t should also be scaled by the characteristic time for visco-capillary breakup[11] $t_{visc-cap} = 14.1 a_0 \rho \nu / \sigma = 14.1 Oh^2 a_0^2 / \nu$ rather than t_{VG} :

$$\frac{t}{t_{visc-cap}} = t \frac{\nu}{14.1 Oh^2 a_0^2} \tag{4.10}$$

56

4.2 Regime diagrams

The first type of results we seek in this study is a complete exploration and qualitative description of the different behaviors the jet can take. This will be the aim of the first part of this section. The subsequent parts are devoted to the second aim of this section, mapping these regimes, for the different fluids of interest, with respect to dimensionless axes defined in the previous section. Experimental maps are established for silicone oil, shampoo base SB 1.8, the micellar fluid CPyCl 100 and commercial shampoo jets. A specific interest is devoted to the boundaries between the different jet regimes of CPyCl 100, with the objective to find scaling laws governing the transitions.

4.2.1 Description of the different regimes

In this part we systematically explore and compare qualitatively the different flow regimes for the different fluids. This is a phenomenological review that will be used in the next parts to draw regime maps for the different test fluids.

Steady jet

In this regime, the jet is steady over time, and the fluid spreads homogeneously on the plate, as shown on figure 2-1 (a). The shape of the jet is well described by the equations (2.3), (2.4a) or (2.5a). This regime happens when the jet is not buckled, which means at low height of fall, and is similar for all the test fluids.

Non-continuous jets

In this regime, that happens at low flow rate, the jet is non-continuous. This means, most of the time, that the fluid will drip from the nozzle rather than form a jet; however for viscoelastic fluids with large extensional viscosity, it may also mean the formation of persistent thinning filaments between the nozzle and the plate with beads of fluids periodically sliding down the filament. The figure 4-1 illustrate several situations for different fluids being dispensed in the non-continuous jet regime. This transient situation is a direct application of CaBER experiments, and is also reminiscent of the beads-on-a-string[51] and gobbling phenomena[61].
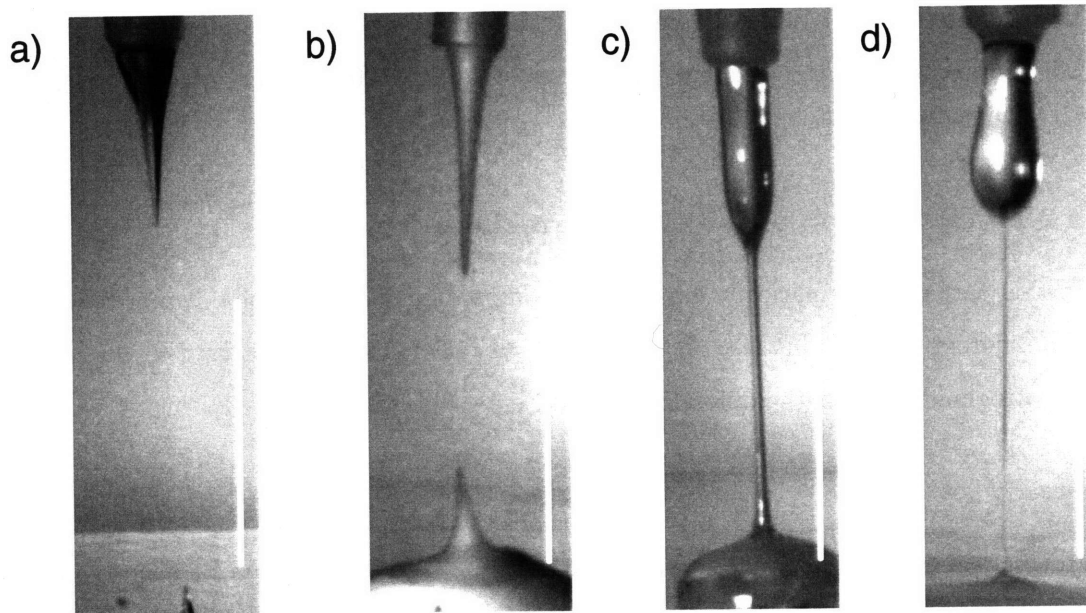
Figure 4-1: Typical views of the non-continuous regime at low flow rates for several fluids. a) Silicone oil b) SB 1.8 c) Boger fluid d) CPyCl 100. Silicone oil and SB 1.8 are viscous fluids which develop little extensional stresses, and encounter visco-capillary breakup at low flow rate. The shear-thinning property of SB 1.8 also enhance breakup through necking. The first stage of capillary thinning is similar for Boger fluid and CPyCl 100, but elastic stresses eventually grow, leading to a thin thread. White bars are 1 cm high.

Figure 4-2: Typical views of coiling regime for several fluids. a) Silicone oil, $H^* = 1.0$, $Q^* = 3.1 \times 10^{-4}$ b) SB 1.8, $H^* = 3.2$, $Q^* = 1.4 \times 10^{-4}$ c) Boger fluid, $H^* = 1.0$, $Q^* = 8 \times 10^{-6}$ d) CPyCl 100, $H^* = 0.9$, $Q^* = 1.3 \times 10^{-4}$. Note especially that CPyCl is the only jet that remains straight until the contact point with the fluid layer. White bars are 1cm high.
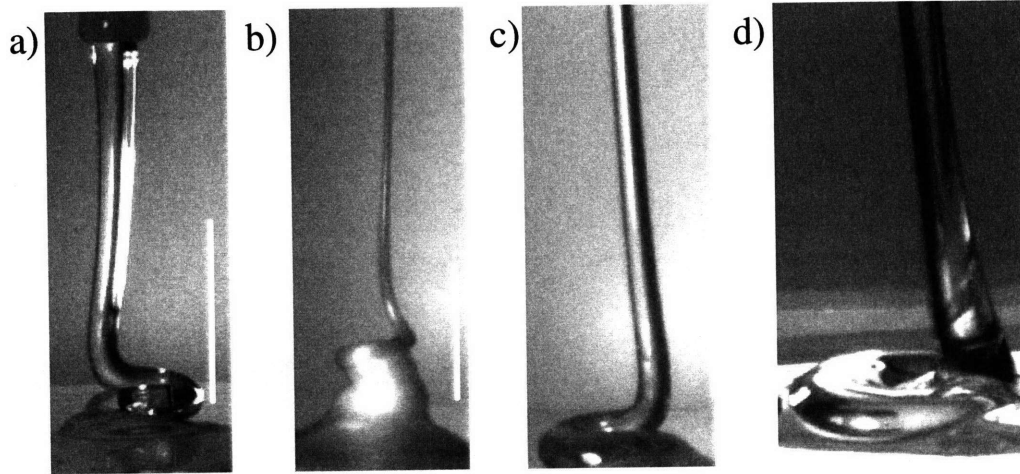
Coiling

Coiling is a type of periodic motion exhibited by a buckled jet. After buckling the jet is pushed sideways by the incoming flow, until it reaches a radius R. At that point the preferred motion that minimizes the viscous stresses is azimuthal (figure 2-5 (b)). The contact point between the jet and the plate then describes circles. Figure 4-2 shows pictures of coiling for several fluids - note especially that the jet of CPyCl 100 is the only one to remain straight until the point of contact with the fluid layer on the bottom plate, a situation allowed by the rheological properties of CPyCl solutions, and specifically their strongly shear-thinning viscosity. All the other jets are significantly twisted or buckled above the fluid layer, a feature that renders previous analysis for the coiling of Newtonian fluids only marginally applicable to CPyCl jets because of the way viscous stresses are localized.

Folding

The folding regime is also defined by an oscillatory motion of the buckled jet, but contrary to coiling, the jet remains confined in a plane. This motion is similar to the folding motion of
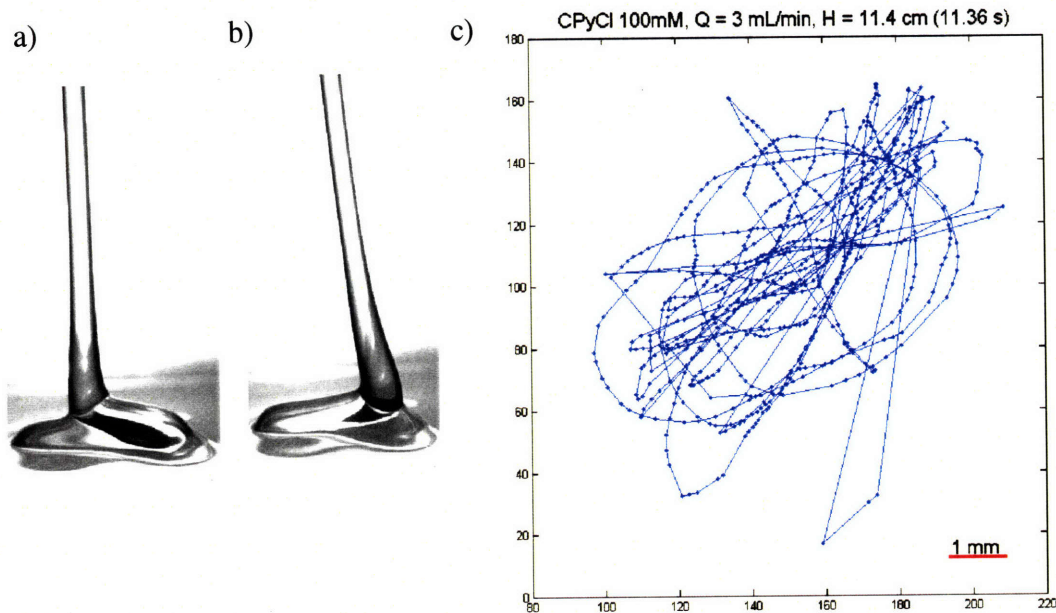
Figure 4-3: Different views of folding motion a) Folding jet as it reaches the central vertical position. b) The same jet at its farthest position, at the onset of buckling under the jet's weight. c) An example of trajectory obtained for a jet of CPyCl 100, from a height $H = 11.4$ cm ($H^* = 3.86$), with a flow rate $Q = 3$ ml/min ($Q^* = 1.06 \times 10^{-4}$). The values of the Reynolds and Ohnesorge number Re $= 10^{-3}$ and $Oh^2 = 10^{-4}$ are typical of the jetting experiments in this thesis.

viscous jets either confined in two dimensions, or exiting a long slit, as described in Skorobogatiy and Mahadevan[32], although in the present case it happens even for a cylindrical jet free to move in all directions. To our knowledge, such a 2D motion for an axisymmetric nozzle and a round jet has not been described before. The only reference to such a folding motion from cylindrical jet we found was in the work of Cruickshank and Munson[3], in a limited window of large flow rates and small height of fall:

$$1 < Re = \frac{Q^*}{a_0^*} < 1.2 \text{ and } 4.810 < \frac{\epsilon^{-1}}{2} = \frac{H}{2a_0} < 7.663 \tag{4.11}$$

In the folding regime, the buckled jet of wormlike micellar fluid moves sideways (figure 4-3 (a)) until it reaches a maximum amplitude L (figure 4-3 (b)), and then folds back on itself . The plane of oscillation sometimes rotates around the vertical axis. This rotation happens when the fluid is rather viscous, the falling jet forming a small heap before spreading away. During the back-and-forth folding motion, the jet sometimes falls from the heap, thus initiating a fold in a different plane. This can sometimes trigger a rotational coiling motion, especially close to the boundary between the two regimes. The jet is truly in the folding regime if it tends to go back to folding in these cases, otherwise it may be classified as a bistable regime.

Figure 4-3 (c) shows an example of the jet trajectory obtained by the laser tracking system. One can see the oscillatory motion primarily in a fixed plane, thus justifying the concept of folding. We can also see the events of coiling, that occurs when the fluid builds up a secondary mound from which the jet tends to be deflected. Nevertheless, after two coils, the jet comes back to its folding motion, because this regime is more stable under these specific experimental conditions.

Bistable regime

In this regime the jet either coils or folds, depending on the history of the flow and the lower boundary conditions. Small perturbating events, such as the presence of a heap of fluid, can trigger the switch between the regimes. In this case both regimes are stable and the system can be forced from one to another.
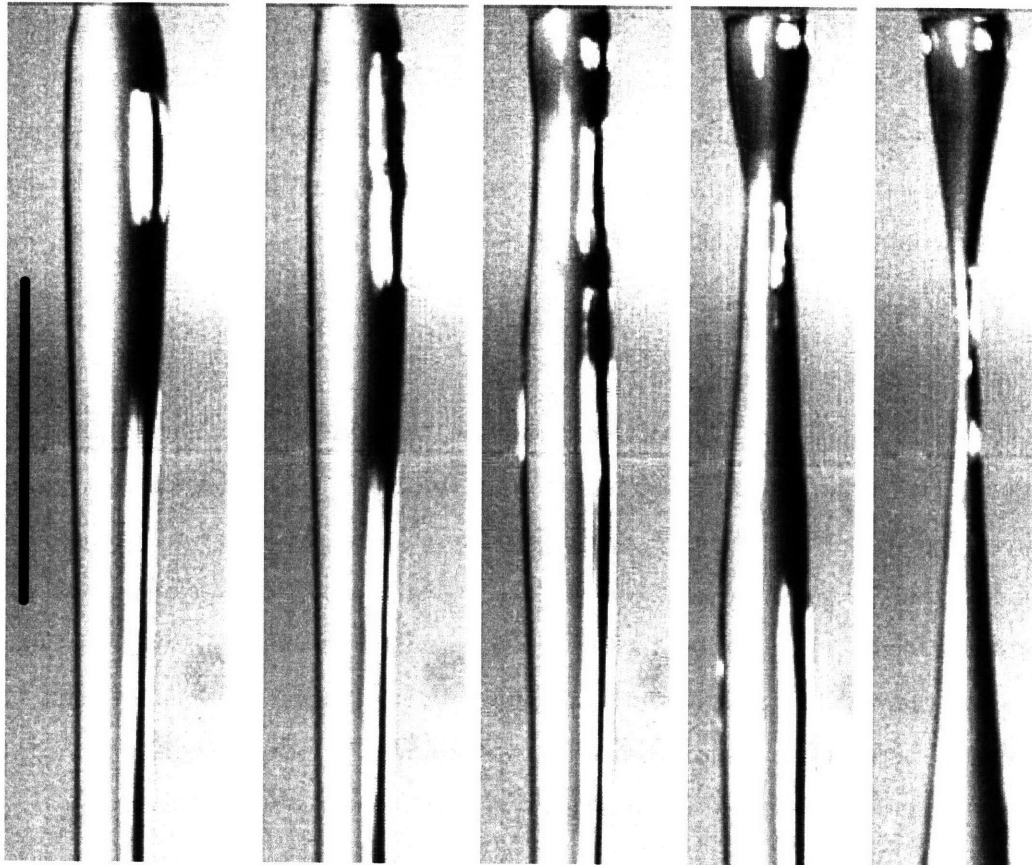
Figure 4-4: Successive views of the high-flow-rate rupture of a jet of CPyCl 100, at $H^* = 4.8$ and $Q^* = 2.7 \times 10^{-4}$ ($H = 16$ cm, $Q = 10$ mL/min). All snapshots are separated by 24 ms, and the black bar is 1cm high.

High-flow-rate rupture

At large flow rates and high extension rate, micellar fluids tend to break in a rubber-like ductile failure[46]. This happens when the weight of the fluid column pulling on a particular cross-section of the jet, usually close to the nozzle, becomes larger than the stress the micelles can sustain. As a result, the micelles break locally, leading to a local weakening of the jet, in return leading to rupture of the entangled micelles. This creates a fracture pattern reminiscent of rubbery failure in solid mechanics, as can be seen in figure 4-4. Since the weight of the column of fluid is the driving force of this mode of jet breakup, it happens at large flow rate and height

Figure 4-5: Example of jet behaviors at large jet inertia, ie at large height of fall and flow rate. a) Inertial folding of CPyCl 100, in which the jet remains straight and vertical down to the folded part, as opposed to s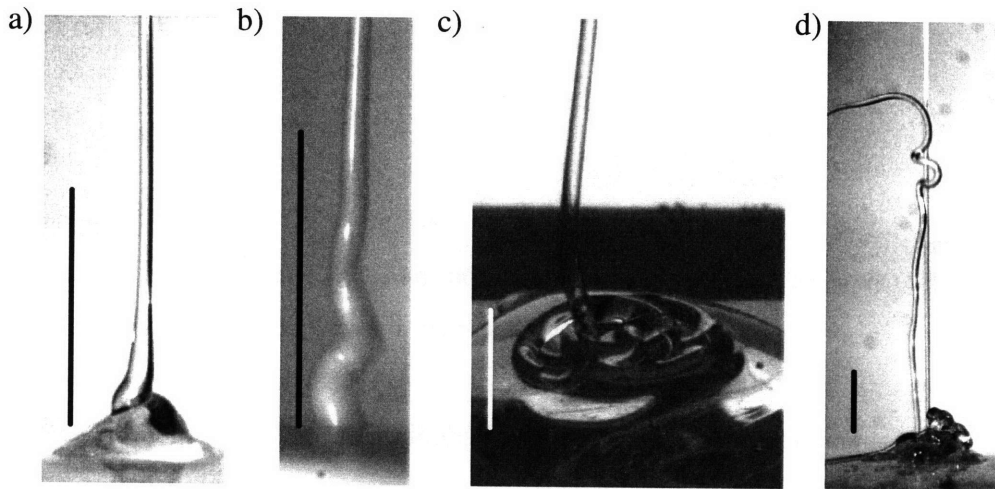ideway motion in gravitational regime. , $H^* = 6.0$, $Q^* = 1.6 \times 10^{-4}$ b) High-velocity impact and buckling of SB 1.8 jet, as opposed to growth of buckling instability from stable jet at lower velocities. This is a transient phenomenon. $H^* = 3.8$, $Q^* = 2.8 \times 10^{-4}$ c) Chaotic motion of commercial shampoo. As the jet inertia increases, commercial shampoo coiling evolves from regular coiling to chaotic motion through period-doubling, precession, and isolated events of large-amplitude motion. $H^* = 1.9$, $Q^* = 6.5 \times 10^{-5}$ d) At even larger inertia, a jet of Herbal Essence commercial shampoo "jumps", a phenomenon called the Kaye effect. $H^* = 7.8$, $Q^* = 8.2 \times 10^{-4}$. Black or white bars are 1cm high (approximately for a), b), and c)).

of fall. A more precise analysis of this condition will be done below in Chapter 5.

Inertial regime behaviors

Jet behaviors at large height of fall and flow rate, that is at large jet inertia, are qualitatively different from what is seen at more moderate experimental parameters. In case of CPyCl jets (figure 4-5 (a)), the jet remains straight and vertical and only the very end of the jet is deflected to the side, as opposed to the entire jet being pushed sideways in gravitational regime. In this regime, the long travel time through the air, coupled with the very large surface to volume ratio, makes the cooling effects due to evaporation very important: in addition to the associated increase in viscosity, this sometimes leads to a Krafft transition with a solid-like

jet falling and breaking. The slightest air current also makes the jet oscillate, which is why quantitative measurement of frequency and amplitude in this regime are difficult for CPyCl jets.

The large velocity of the impacting jet can also lead to more extreme behaviors. Figure 4-5 (b) is a jet of SB 1.8 impacting the bottom plate and buckling in several places at once. Nevertheless, this is only a transient phenomenon, and the established regime in this case is simply coiling. Figure 4-5 (c) and (d) show jets of commercial shampoo at large inertia, which offer good examples of other extreme behaviors. As the height of fall increases, the coiling motion of the shampoo jet goes through period doubling and "figure of eight" patterns, and eventually becomes chaotic (figure 4-5 (c)). At even larger heights of fall, the jet sometimes slides on the liquid layer, a thin layer of locally shear-thinned fluid acting as lubricant. These large-amplitude events eventually turn into "leaping shampoo" as the height of fall in increased still further. The Kaye effect happens for shampoo jets (as well as other non-Newtonian fluids as described by Kaye[37] and Collyer[38]) falling on a plate. At large enough heights of fall and flow rate a spectacular secondary jet emerging out of the liquid layer, for example the figure 4-5 (d) shows the leaping jet of Herbal Essence shampoo.

4.2.2 Regime diagram for Newtonian fluids

We know map the different regimes into the parameter space for the different test fluids. This requires to use dimensionless parameters so that it is possible to draw general conclusions from different fluids, and especially for the two external parameters H, the height of fall, and Q, the imposed flow rate. The group for the flow rate is $Q^* = Q(g/\nu^5)^{1/3}$ as defined in equation (4.2), but two groups can be used for the height of fall, $\epsilon^{-1}/2 = H/2a_0$ or $H^* = H(g/\nu^2)^{1/3}$. The former is suited for low-height phenomenon, where the geometry constrains the jet dynamics, while the latter is more suited to larger heights when gravitational thinning takes place. We choose to draw the regime maps using $\epsilon^{-1}/2$ because it relates to the buckling criteria (2.9a) and (2.9b) from Cruickshank and Munson[3].

Figure 4-6 (a) is a regime map of silicone oil T41, for which only three regimes are typically observed: steady jet, dripping, and coiling. Note that sub-classification of coiling in viscous,
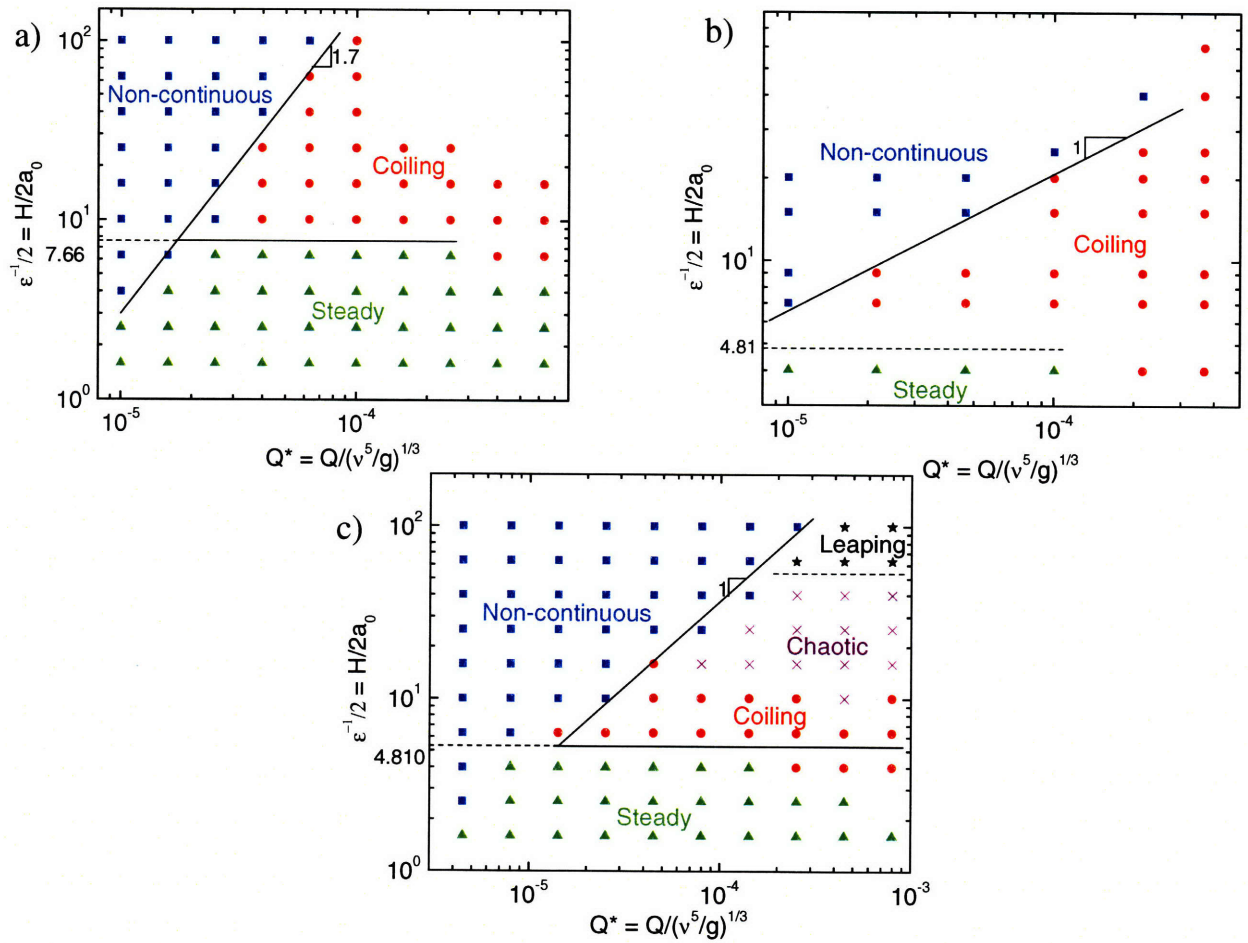
Figure 4-6: Regime maps for silicone oil (a), shampoo base SB 1.8 (b) and Herbal Essence commercial shampoo (c). The first two fluids show only three behaviors in the ranges of height and flow rate investigated; steady jet (▲), dripping (■), and coiling (●). Herbal Essence shampoo also shows chaotic coiling (X) and leaping jet (★). Solid lines are guide to the eyes for regime transitions, while the dashed line is Cruickshank's prediction for buckling transition ((2.9a) for (a) and (2.9b) from (b) and (c)).

gravitational and inertial regimes is not taken in account here, since it is hard to determine without actually measuring the coiling frequency. This can be done by frame counting using the setup of figure 3-10 a), and it is the object of the studies by Ribe[6] The buckling transition at moderate flow rates are consistent with (2.9a) (dashed line). At large flow rates, the increased compressive stress favors buckling, and the transition happens at a lower height.

The dripping-jetting transition (solid line) is observed to be given by the scaling law $\epsilon^{-1} \sim Q^{*1.7}$. In other words and using (4.2) and (4.9), the flow rate required to maintained a continuous jet increases with height of fall and scales as

$$Q \sim H^{1/1.7} \simeq H^{0.6} \tag{4.12}$$

4.2.3 Regime diagram for shampoo bases and commercial shampoo

The regime map for SB 1.8 is presented in 4-6 (b), and maps for other shampoo bases are qualitatively comparable. SB 1.8 undergoes the same behaviors as silicone oil, although several features are slightly different. The regime map for Herbal Essence commercial shampoo is shown in figure 4-6 (c) and despite being quite similar to the regime map for SB 1.8 in most of the parameter space, presents two additional jetting regimes. As the jet inertia is increased, at larger heights and flow rates, the coiling motion becomes increasingly chaotic, as shown on figure 4-5 (c), before the onset of the Kaye effect (figure 4-5 (d)).

For both fluids, the buckling occurs at a lower height than Newtonian fluids, $\epsilon^{-1}/2 \simeq 5$ rather than $\epsilon^{-1}/2 \simeq 7.5$, possibly because shear-thinning facilitates buckling. The dripping transition happens at a height scaling as $H \sim Q$. This means that dripping is favored with SB 1.8 and Herbal Essence shampoo compared to Newtonian fluid, which is not surprising since shear-thinning is expected to favor breakup, by a mechanism similar to necking in plastic deformations.

4.2.4 Regime diagram for CPyCl 100

Figure 4-7 shows the experimental regime map for CPyCl 100. Several features can be noted in comparison to the Newtonian diagram of figure 4-6 (a). Among the features that are somewhat

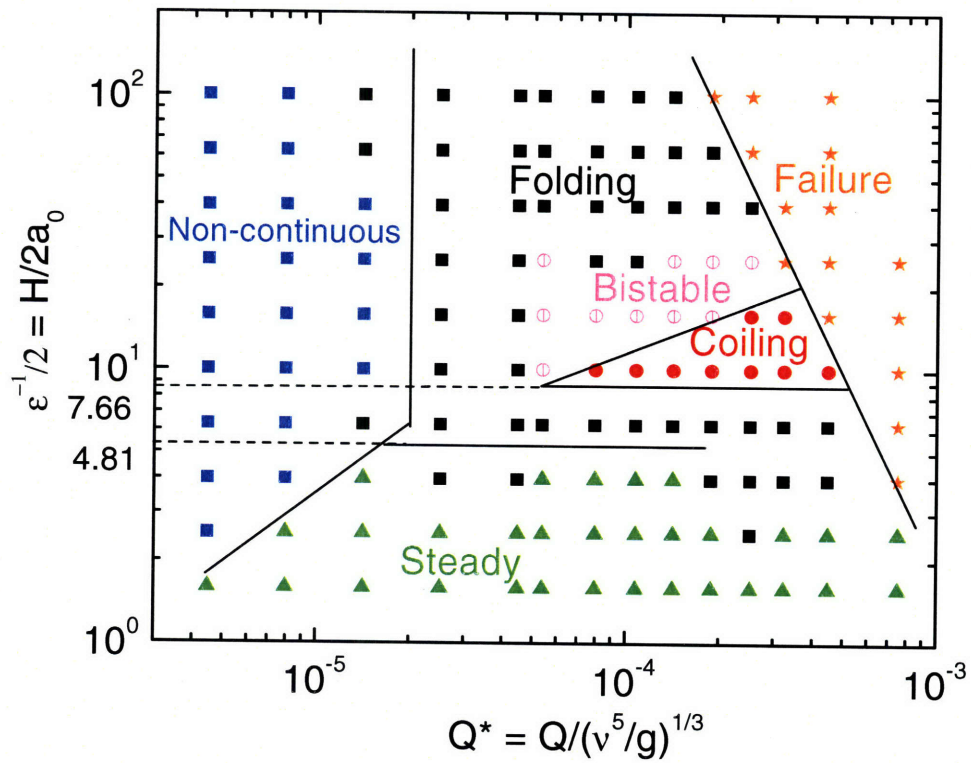Figure 4-7: Experimental regime map of CPyCl 100 in the $\epsilon^{-1}/2$ and Q^* space. The regimes are: steady (▲), non-continuous flow (■), coiling (●), folding (■), bistable coiling and folding (∅), elastic rupture (★). The lines are guides to the eyes.

similar to the Newtonian map, stable, axisymmetric jet is maintained at low heights of fall, non-continuous jet happens at low flow rate, and most of the parameter space is occupied by time-dependent buckled jets. Nevertheless, significant changes are visible, such as the existence of the folding regime, the ductile failure at large flow rates, the coexistence of folding and coiling regimes, and the different slope of the dripping-jetting transition. CPyCl 75 and 150 have a behavior similar to CPyCl 100. A more precise study of CPyCl 100 regimes boundaries is presented below.

4.2.5 Regime diagram for the Boger fluid

For experimental reasons it has not been possible to obtain a full regime map for the Boger fluid. In general terms, the Boger fluid tend to follow the Newtonian pattern, displaying only coiling in the buckled part of the regime space. The main departure from Newtonian behavior appears at low flow rate, where its strong elasticity resists capillary breakup in a fashion similar to CPyCl solutions. No folding dynamics has been observed with a cylindrical jet of Boger fluid.

4.2.6 Experimental scaling laws for the regime transitions of CPyCl solutions

Detailed investigation of the transition between regimes has been conducted for various CPyCl solutions and experimental conditions (flow rate, height of fall, and nozzle size). The various graphs of figure 4-8 present the data for one transition each, with respect to the most relevant axes at that transition. The horizontal axis is always $Q^* = Q(g/\nu^5)^{1/3}$, which scales for the effect of viscosity and allows the direct comparison between the different solutions. The vertical axis is either $\epsilon^{-1}/2 = H/2a_0$ or $H^* = H(g/\nu^2)^{1/3}$, depending on which allows the collapse of the data set. $\epsilon^{-1}/2$ is expected to be more relevant at low heights, whereas H^* should be better at larger heights when gravitational thinning takes place. The nozzle radius was corrected using the equation (5.16) to take into account the die-swell effect which will be covered in Chapter 5. Jets of non-Newtonian fluids tend to swell as they exit a nozzle, and the correction for this phenomenon is especially important at large flow rates and small nozzle radii
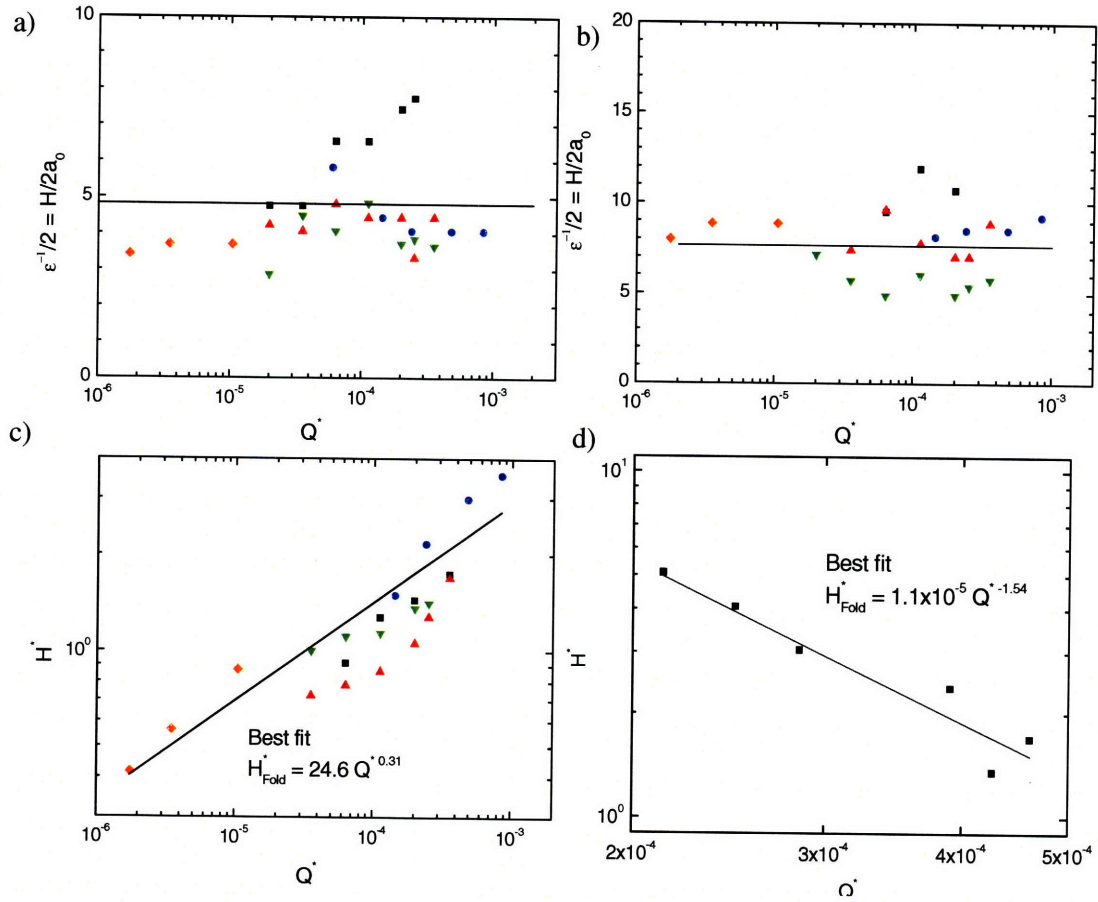
Figure 4-8: The transitions between different flow regimes with CPyCl 100 and $a_0^* = 2.6 \times 10^{-2}$ (■); CPyCl 75 and $a_0^* = 4.2 \times 10^{-2}$(●); CPyCl 100 and $a_0^* = 4.2 \times 10^{-2}$(▲);CPyCl 150 and $a_0^* = 4.2 \times 10^{-2}$(◆); and CPyCl 100 and $a_0^* = 8.1 \times 10^{-2}$(▼). a) Critical condition for transition between steady axisymmetric flow and folding (buckling) at $\epsilon^{-1}/2 = 4.8 \pm 2$ b) Transition from folding to coiling when the height of fall is increased from a low height for a given flow rate at $\epsilon^{-1}/2 = 7.6 \pm 1$ c) Transition from folding to coiling when the height of fall is decreased from a large height for a given flow rate. d) Appearance of jet rupture event when increasing flow rate for a given height of fall.

Buckling limit

Figure 4-8 (a) shows that when the aspect ratio $\epsilon^{-1}/2 = H/2a_0$ reaches a critical value close to 4.81, the prediction given by (2.9b) (solid line), the jet buckles and starts folding. A strong hysteresis between stable and folding regimes when the height of fall is varied continuously explains in part the scatter of the data. Nevertheless, the transition happens for $3 < \epsilon^{-1}/2 < 8$ when Q^* is varied across three orders of magnitude. Newtonian fluids buckle at a higher value of ϵ^{-1}, $\epsilon^{-1}/2 \simeq 7.66$ as given by (2.9a).

First Folding-Coiling transition

Above the limit given by (2.9a), the jet switches to the azimuthal mode of instability and begins to coil (figure 4-8 (b)). This is the limit at which Newtonian jets usually buckle and start coiling. This immediately suggests that the analysis that led to the limits (2.9a) and (2.9b) for the Newtonian fluids is still valid for the CPyCl solutions, although in the case of CPyCl solutions the folding mode is stabilized by mechanisms that do not exist in the Newtonian case. A complete discussion will be presented in the Chapter 5.

Experiments show that the transition between the folding and coiling occurs over a rather ill-defined range of height for which the two modes alternate, the switching between the two being triggered by random events such as the jet falling from a heap of liquid that has not evenly spread out. Cruickshank[27] also noted this problem in the narrow parameter range where folding was observed with Newtonian fluids. It is interesting to note that when the ambient temperature was closer to $25°C$, so that the viscosity was lower, the heaps of liquid were less pronounced, and the frequent switching was replaced by a bistable region, leading to a large hysteresis in the transition. Overall, there is some scattering around the predicted value of $\epsilon^{-1}/2 \simeq 7.66$ for that transition, with $4 < \epsilon^{-1}/2 < 12$, but once again this remains valid over three orders of magnitude for Q^*.

Second Folding-Coiling transition

When the height of fall was raised even more, a second transition occurs (figure 4-8 (c)), from coiling back to folding, with an even more pronounced bistability than the first transition, as

can be seen on the regime map of figure 4-7. Because of it, we measured the transition from coiling to bistable folding and coiling. In other words, from the coiling regime and for a given flow rate, we raised the height until we saw the first events of folding. For this transition, the parameter that allowed the best collapse of the data was the dimensionless height of fall H^* rather than ϵ^{-1}. In contrast to the measurements of the previous two boundaries, the critical height for this transition varies with the flow rate. Experimentally, the scaling dependency is close to $H^* \sim Q^{*1/3}$

Jet rupture at large flow rate: ductile failure

At very large flow rates, the wormlike micelles cannot sustain the axial stresses anymore and break *en masse*, leading to the solid-like failure of the jet (figure 4-8 (d)). The flow rate required to observe jet rupture decreases with height, and scales as $Q^* \sim H^{*-1/1.54} = H^{*-0.65}$. There is an overlap between the coiling and jet rupture zones, for which the jet has enough time to coil a few times before breaking.

Dripping-Jetting transition at low flow rates

Instead of Newtonian dripping (figure 4-1 (a)), the non-continuous regime for CPyCl 100 was observed to consist of long, thin filaments prevented from breakup by elastic forces (figure 4-1(d)). A significant difference with the Newtonian regime map is that the transition between the non-continuous and continuous jet happens for almost all heights at a constant flow rate, $Q^* > Q^*_{min}$. Since the elasticity of the entangled micelles holds the thread and prevents breakup, a continuous jet is sustained above a threshold flow rate.

4.3 Quantitative measurements

The second step of the experimental part of this study is the quantitative measurement of several features of non-Newtonian jets. These include both the study of the jet profile and of motion of CPyCl jets in folding regime, because both are qualitatively different from the shape and motion of Newtonian jets or shampoo jets. The influence of the viscoelastic properties of Boger fluids on gravity-driven jets properties has been studied by Chai and Yeow[63], but to
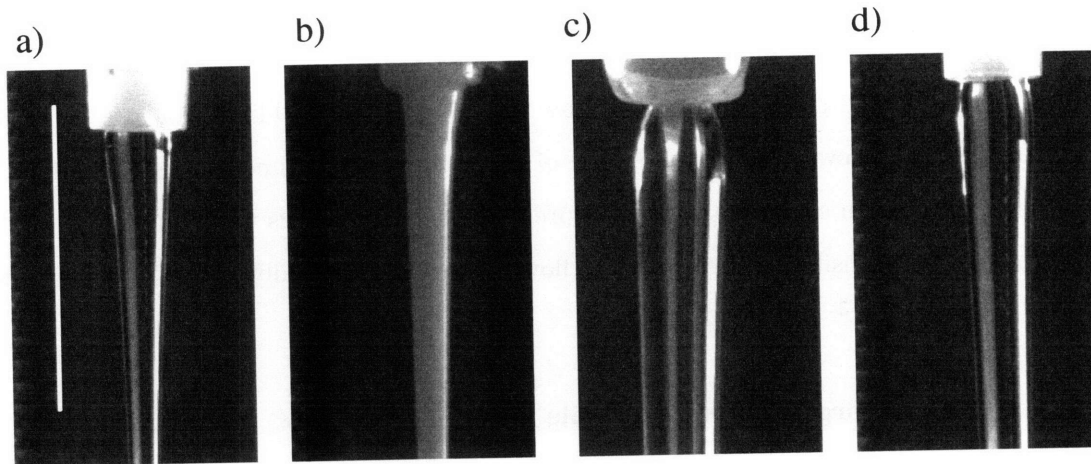
Figure 4-9: Close view of jet exiting nozzle at large flow rates. The white bar is 1cm high. a) Silicone oil, $Q^* = 5.7 \times 10^{-4}$ b) SB 1.8, $Q^* = 3.7 \times 10^{-4}$ c) Boger fluid, $Q^* = 6.9 \times 10^{-5}$ d) CPyCl 100, $Q^* = 2.7 \times 10^{-4}$

our knowledge, the specific features of jets of CPyCl solutions have not been described before. A qualitative comparison with the other fluids of interest will also be provided.

4.3.1 Jet shape

Die swell

Some viscoelastic fluids, for example most dilute polymer solutions, swell when exiting a nozzle. This is a well-known effect[52], taken into account in problems such as fiber drawing. Figure 4-9 shows qualitatively the extent of this phenomenon for the different fluids of interest at comparable dimensionless flow rates. Newtonian silicone oil and weakly viscoelastic SB 1.8 do not show any noticeable swell at the nozzle, Boger fluid shows a large swelling, and CPyCl 100 shows moderate swelling.

Gravitational thinning

Newtonian jets falling from a sufficient height (equation (2.5a)) thin continuously under the acceleration of gravity, until a balance between gravitational and viscous forces is reached. After that point the radius is constant, even in the coil. CPyCl jets undergo at first the same
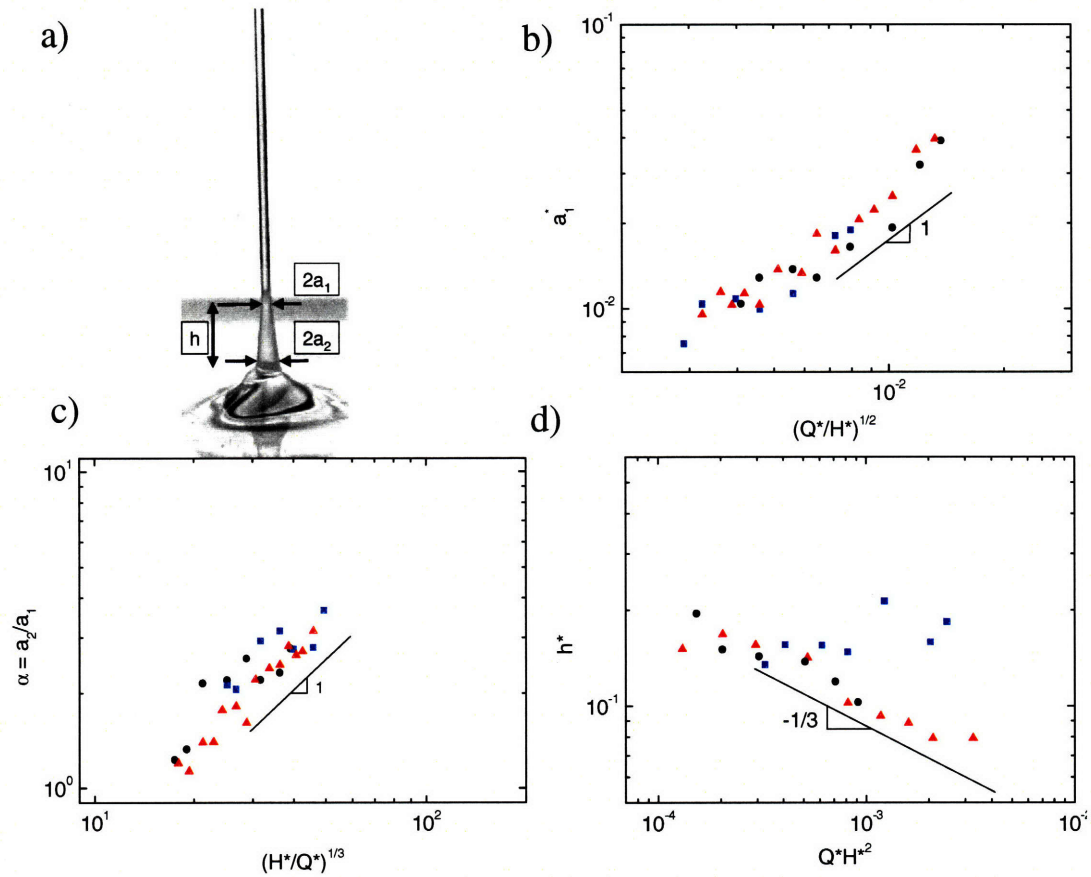
Figure 4-10: Quantitative measurements of the dynamics in the tail, with $Q^* = 7.1 \times 10^{-5}$, $0.4 \leqslant H^* \leqslant 6.8$ ($\blacktriangle$); $H^* = 1.7$, $2.8 \times 10^{-5} \leqslant Q^* \leqslant 3.2 \times 10^{-4}$($\bullet$); and $H^* = 3.4$, $2.8 \times 10^{-5} \leqslant Q^* \leqslant 2.1 \times 10^{-4}$($\blacksquare$). a) Definition of the measured variables. For this jet $H^* = 2.4$, $Wi = 29.8$ b) Dimensionless radius just above the swell c) Swelling ratio $\alpha = a_2/a_1$ d) Height of the swollen region.
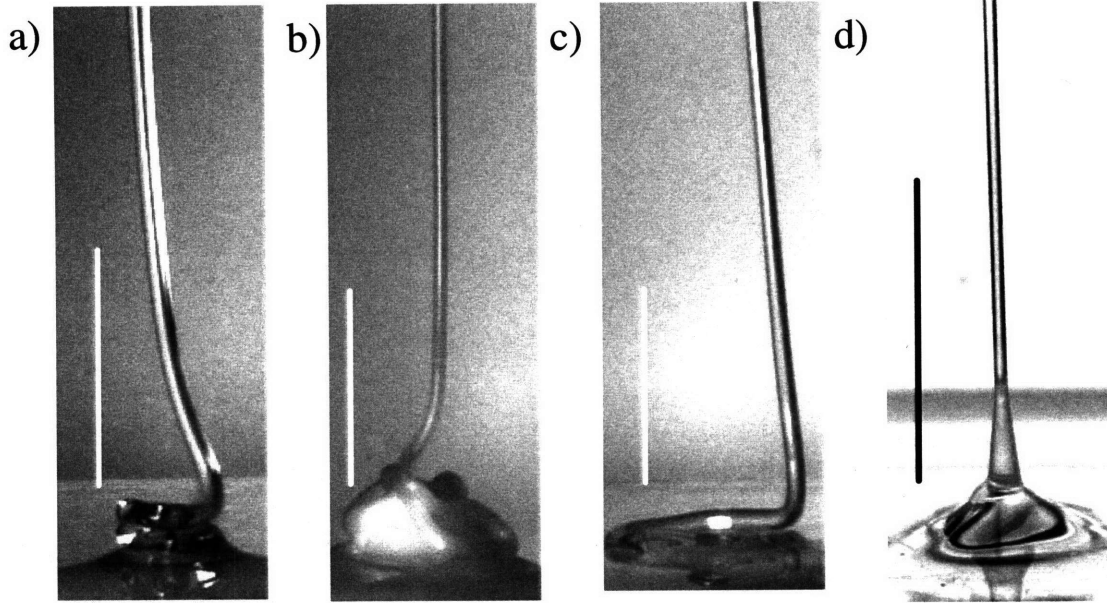
Figure 4-11: Typical view of bottom part of the jet at large height, showing that only CPyCl solutions show reverse die swell among the studied fluids. White or black bars are 1cm high a) Silicone oil, $H^* = 3.9$, $Q^* = 2.3 \times 10^{-4}$ b) SB 1.8, $H^* = 3.2$, $Q^* = 1.4 \times 10^{-4}$ c) Boger fluid $H^* = 3.0$, $Q^* = 8.0 \times 10^{-6}$ d) CPyCl 100 $H^* = 4.7$, $Q^* = 5.3 \times 10^{-5}$

process of gravitational thinning followed by gravito-viscous steady state. This steady-state radius is a_1, as defined on figure 4-10 (a), or $a_1^* = a_1/l_{VG} = a_1(g/\nu^2)^{1/3}$ in dimensionless terms (equation (4.4)). This gravity-thinned radius was measured experimentally from snapshots obtained in the setup described in figure 3-10 (a). The results that are shown on figure 4-10 (b) reveal that in dimensionless form, this radius scales as

$$a_1^* \sim \left(\frac{Q^*}{H^*}\right)^{1/2} \tag{4.13}$$

Reverse swell

Figure 4-11 show typical views of the bottom part of jets of several fluids, at a large height of fall ($H^* > 3$). In this regime the jet is significantly thinned with respect to the original diameter, the amount of gravitational thinning being given experimentally by equation (4.13). Of all the fluids shown (silicone oil, shampoo base, Boger fluid, and CPyCl 100) only CPyCl

74

100 does not maintain a constant diameter as it approaches the fluid layer. CpyCl jets instead differ significantly by widening at their base (figure 4-11 (d)) just before reaching the fluid layer. The final radius a_2, as defined on figure 4-10 (a), can be up to three times larger than a_1. We call this widening *reverse swell*, because it is reminiscent the die-swell effect. In both cases, non-Newtonian jets widen as they relax stored elastic normal stresses. To our knowledge, this novel feature of CPyCl jets has not been mentioned in existing literature.

Contrary to die swell phenomenon, reverse swell of CPyCl jets is not related to the upper boundary condition. The swelling does not happen at a position determined from the nozzle, but rather at a height h above the lower plate and fluid layer. On this length scale h, the jet widens from a radius a_1 to a larger value a_2. The amount of swelling is characterized by the swelling ratio $\alpha = a_2/a_1$. Experimental measurements shown on figures 4-10 (c) and (d) show that α and $h^* = h/l_{VG} = h(g/\nu^2)^{1/3}$ scale as

$$\alpha \sim \left(\frac{H^*}{Q^*}\right)^{1/3} \tag{4.14a}$$

$$h^* \sim \left(H^{*2}Q^*\right)^{-1/3} \tag{4.14b}$$

4.3.2 Jet dynamics

The folding regime of CPyCl jets is studied in detail because it is qualitatively different from the dynamical motion of Newtonian jets. Viscous Newtonian fluids coil regularly over a wide range of heights of fall, and have been studied extensively ([5], [6]). Newtonian fluids only show folding with sheets flowing from a slit or, with round nozzles, in very specific and limited conditions[27] such as using a bath of fluid of matching density to suppress the effect of gravity. In the case of CPyCl jets, folding is easily accessible with round nozzles (figures 4-3 (a) and (b)). The variations of folding frequency f and amplitude L with respect to experimental parameters are presented in figure 4-12.

Multiple series of experiments were performed to fully capture the folding dynamics, in two sets. In the first one, three series of amplitude and frequency measurement were made using the setup described on figure 3-10 (a), with a fixed flow rate and varying height. The imposed
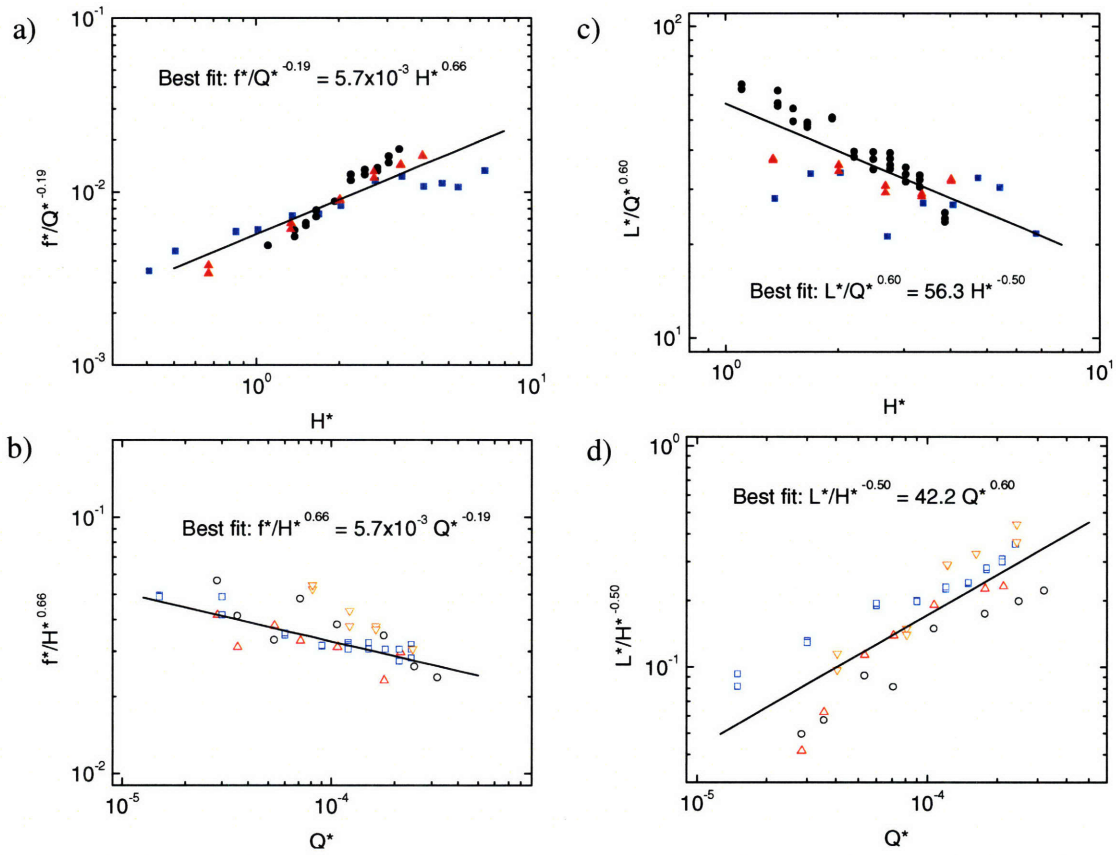
Figure 4-12: Quantitative measurements of folding properties, frequency (a and b) and amplitude (c and d). First set of experiments with fixed flow rate (a and c): $Q = 2$ ml/min ($Q^* = 4.3 \times 10^{-5}$) ($\bullet$); $Q = 2$ ml/min ($Q^* = 7.1 \times 10^{-5}$) ($\blacksquare$); $Q = 5$ ml/min ($Q^* = 1.7 \times 10^{-4}$) ($\blacktriangle$). Second set of experiments with fixed height of fall $H = 5$ cm ($H^* = 1.7$) ($\circ$); $H = 6$ cm ($H^* = 1.9$) ($\square$); $H = 9$ cm ($H^* = 3.2$) ($\triangle$); $H = 10$ cm ($H^* = 3.4$) ($\triangledown$).

flow rate was $Q = 2$ mL/min for the first two series and $Q = 5$ mL/min for the third one. The series of tests were conducted at different ambient temperatures, 22.5^oC, 20.6^oC, and 21.5^oC respectively, which also affects the viscosity of the fluid, leading to three values of imposed dimensionless flow rates: $Q^* = 4.3 \times 10^{-5}$, $Q^* = 7.1 \times 10^{-5}$, and $Q^* = 1.7 \times 10^{-4}$. For each series, the flow rate was held constant, while the fall height of the jet was varied from 1.2 to 20 cm ($0.4 < H^* < 6.7$). Note that amplitude data were difficult to collect at low values of H^* and are therefore given over a smaller range than frequency data. In the second set of tests, four series of experiments were performed with a fixed height of fall and varying flow rate. The heights of fall H were 5, 6, 9 and 10 cm (with temperatures of 22.5^oC, 21.3^oC, 21.8^oC, and 22.5^oC and dimensionless height H^* of 1.7, 1.9, 3.2, 3.4 respectively), with a flow rate Q varying between 0.5 and 9 mL/min ($1.5 \times 10^{-5} \leqslant Q^* \leqslant 2.1 \times 10^{-4}$). All experiments were made using the CPyCl 100 fluid, because it is the CPyCl solution most suited for studying jets as was discussed from figure 3-4 (b), and because it helps in eliminating other possible dependencies, especially regarding fluid rheology. The elastogravitational number for this fluid at 22.5^oC is $E_g = \lambda \left(g^2/\nu_0\right)^{\frac{1}{3}} = 12.4$, which means that significant elastic effects are expected to take place at sufficient fall heights, when gravitational thinning is important.

Experimental results and associated scaling laws are shown on figure 4-12. Graphs a and b show the frequency measurements, while c and d display the amplitude data. Graphs a and c show the first set of experiments with fixed flow rate, while b and d show the second set with fixed height of fall. Data points for each set of experiments were collapsed using experimental scaling laws obtained from the other set. In the cases where the collapse of data changed slightly the scaling exponent, by less than 1% and largely within the experimental error, the collapse of the data of the other set were adjusted with the new exponent. Eventually, the experimental scaling laws for folding motion are found to be

$$\text{For frequency, } f^* \quad \sim \quad H^{*0.66}Q^{*-0.19} \tag{4.15a}$$

$$\text{For amplitude, } L^* \quad \sim \quad H^{*0.50}Q^{*0.60} \tag{4.15b}$$

where, as defined in the nondimensionalizing scheme, $H^* = H(g/\nu^2)^{1/3}$, $Q^* = Q(g/\nu^5)^{1/3}$, $f^* = f(\nu/g^2)^{1/3}$, and $L^* = L(g/\nu^2)^{1/3}$. The power laws (4.15a) and (4.15b) are obtained

from global regression of all experiments taken together, but each series of experiments gave dependencies that differs sometimes significantly from the overall trend. The causes for these variations are difficult to control and result from experimental parameters, such as effect of temperature on extensional viscosity, effect of ambient humidity on evaporation and cooling, or rheological aging of the solution. These parameters are constant for a given series of experiments, but vary from series to series, therefore statistical analysis based on the hypothesis of stochastic deviation from a trend is not applicable. It is only possible to give the range of scaling exponents obtained from different series, which are provided in Table 4.1.

	Overall exponent	Range of exponents
H^* dependency of f^*	0.66	$0.4 - 1.2$
Q^* dependency of f^*	-0.19	$-0.18 - -0.5$
H^* dependency of L^*	-0.50	$-0.1 - -0.7$
Q^* dependency of L^*	0.60	$0.45 - 0.8$

Table 4.1: Range of scaling exponents obtained for various series of experiments, compared to global scaling exponents obtained from regression to full data set.

Chapter 5

Analysis

The theoretical analysis in this chapter is focused on the experimental results obtained for wormlike micellar solutions, with the purpose to derive scaling laws of their non-Newtonian features with respect to external parameters and fluid properties. First, the dynamics in the jet as it falls are investigated, as they governs the jet's shape. Wormlike micellar jets share some common behavior with Newtonian jets, and at the same time display some strong deviations due to elastic and extension-stiffening properties. Next, the jet motion is investigated, and especially the novel folding motion. A theoretical mechanism is provided, and scaling laws are derived from it and compared with experimental results. This mechanism and other physical consideration are used, at last, to provide criteria that describe the experimentally observed transitions between regimes.

5.1 Dynamics in the tail

5.1.1 Die swell

Tanner[52] gives the die-swollen radius a_{swell} (figure 2-1 (d)) as a function of shear stress τ_S and the shear compliance J_S:

$$a_{swell} = a_0 \left(1 + \left(0.13 + \frac{1}{2}(J_S\tau_S)^2 \right) \right)^{\frac{1}{6}} \tag{5.16}$$

where the term 1.13 is a correction for purely Newtonian swell effects. For a constant

viscosity Boger fluid, τ_S is proportional to flow rate, $\tau_S = \eta(Q/a_0^3)$. Therefore, a_{swell} scales as $a_{swell}/a_0 \sim Q^{1/3}$ in the limit of large flow rates. With a shear-thinning fluid such as CPyCl wormlike micellar solution, $J_S = 1/G_0 = \lambda/\eta_0$, and τ_S is the smaller of η_0/λ and $\eta_0 Q/\pi a_0^3$, since we know from figure 3-3 (b) that the shear stress is bounded. Therefore, a_{swell}/a_0 is limited to 1.085 in most experiments, i.e. no more than 8% of die swell, and this minor correction does not scales significantly with problem parameters. The following scaling analysis will all use a_0 as initial radius, and a_{swell} will be used only when quantitatively comparing experimental values to predictions.

5.1.2   Gravitational thinning of CPyCl jets

While the balance of gravitational and viscous forces that is used to derive the expression for a_1 in equation (2.8) has been made for Newtonian fluids, the dynamics in the tail are, to the first order, the same for viscoelastic jets. The figure 4-10 (b) shows that the dependency $a_1^* \sim \sqrt{Q^*/H^*}$ still holds for CPyCl jets. The elastic stress is negligible with respect to the viscous stress, and therefore does not affect significantly the thinning process, or at least its dependency on Q and H. For gravitational thinning to occur, the fall height of the jet must be sufficiently large, and the imposed flow rate sufficiently low, in order to let gravity significantly accelerate the fluid particles during their residence time in the jet. As we stated in equation (2.6), gravito-viscous thinning occurs for $\beta = H a_0 \sqrt{g/6Q\nu} > \pi/2$, or, in dimensionless terms and omitting the multiplying constant, for

$$H_{thinning}^* > \frac{Q^{*1/2}}{a_0^*} \tag{5.17}$$

5.1.3   Reverse swell

The reverse swell (figure 4-10 (a)) is a very peculiar feature of jets of wormlike-micellar jets, in which the jet widens at its base, becoming between two to three times wider than the thinnest part of the tail, on a height scale of around a centimeter. For Newtonian jets, the jet is constantly thinning down to the coil region, where the radius is constant. In the case of CPyCl micellar jet, this reverse swell effect arise from the non-Newtonian viscoelastic character of the liquid. As the fluid accelerates under the effect of gravity, the fluid elements stretch, the wormlike

80

micelles get aligned and store elastic energy. When the stretch rate becomes weaker, because of the deceleration imposed by the presence of the plate, the stretched molecules recoil, which leads to the dilation in the horizontal plane. A noticeable reverse swell is therefore possible for a Weissenberg number $Wi_{stretch} = \lambda(U_1 - U_0)/H = E_g(H^* - Q^*/a_0^{*2})$ greater than one. Note that this condition requires $H^* \geq Q^*/a_0^{*2}$, which means that the fluid particles must be accelerated during the fall. For practical purposes (in order to get a measurable reverse swell), the condition is more realistically $H^* \gg Q^*/a_0^{*2}$, which simplifies the condition for reverse swell to

$$Wi = E_g H^* \gg 1 \tag{5.18}$$

For example, the jet used in figure 4-10 (a) is characterized by a large value of $Wi = 29.8$ and a significant reverse swell.

The reverse swell is reminiscent of the die-swell phenomenon, and a derivation similar to that given by Tanner[52] can be used to predict the amount of swelling. The assumption is that no external force acts on the fluid elements over the length scale of recoil h, thus we neglect gravity on the scale of $h \ll l_{VG}$ as well as the reaction of the bottom plate. If N_1 is the first normal stress difference in the fluid just before the swell, P the hydrostatic pressure in the jet, I the identity matrix, and $\alpha = a_2/a_1$ is the swell ratio, the force balance can be written as

$$-PI + \begin{pmatrix} 3G & 0 & 0 \\ 0 & 3G & 0 \\ 0 & 0 & 3G + N_1 \end{pmatrix} \begin{pmatrix} \alpha^2 & 0 & 0 \\ 0 & \alpha^2 & 0 \\ 0 & 0 & \frac{1}{\alpha}^4 \end{pmatrix} = 0$$

This corresponds to three equations with four unknowns. Eliminating P among these equations leads to

$$\alpha = \left(1 + \frac{N_1}{3G}\right)^{\frac{1}{6}} \tag{5.19}$$

The viscoelastic fluid elements will be considered as purely elastic during the stretch process in the tail of the jet. This does not imply that the elastic component of the tensile stress is more important that the viscous part, which would not be true, but only that the elastic part does not relax during the time of fall, which is legitimate for moderate residence time in the jet and $Wi \gg 1$. We can therefore equate N_1 to the tensile stresses from rubber elasticity theory,

given by

$$N_1 = 3G\left(\left(\frac{a_0}{a_1}\right)^4 - \left(\frac{a_1}{a_0}\right)^2\right) \tag{5.20}$$

We have already assumed that $a_1 \ll a_0$ (significant thinning), therefore the first order approximation of (5.20) combined with (5.19) gives

$$\alpha = \left(\frac{a_0}{a_1}\right)^{\frac{2}{3}} \tag{5.21}$$

In dimensionless form, and using the value for a_1 given by (2.8), one finds that the swell ratio α should vary as

$$\alpha = \frac{a_2}{a_1} \sim \left(a_0^{*2}\frac{H^*}{Q^*}\right)^{\frac{1}{3}} \tag{5.22}$$

The data in figure 4-10 (c) shows a good agreement between the experiments and the scaling behavior predicted by (5.22). The equation (2.8), which was $a_1 \sim (Q/H)^{1/2}(\nu/g^2)^{1/6}$ when omitting the multiplying constant, can be rewritten in dimensionless terms as

$$a_1^* \sim \sqrt{\frac{Q^*}{H^*}} \tag{5.23}$$

This scaling law is verified on figure 4-10 (b). Combining (5.22) and (5.23) also leads to the following scaling for the final radius a_2:

$$a_2^* \sim \left(a_0^{*\,2}\sqrt{\frac{Q^*}{H^*}}\right)^{\frac{1}{3}} \tag{5.24}$$

In dimensional terms, this is

$$a_2 \sim \left(a_0^2\sqrt{\frac{Q}{H}}\right)^{\frac{1}{3}}\left(\frac{\nu_0}{g^2}\right)^{1/18} \tag{5.25}$$

Note that, rigorously speaking, the elongation-free state taken as reference occurs after the normal stresses built up in the nozzle are relaxed, that is, at the die swell, rather than at the nozzle. This means that the occurrences of a_0 in equations (5.20) to (5.24) ought to be

modified using (5.16) to use a_{swell}. Nevertheless, as already mentioned, the error is bounded by the strong shear-thinning properties of CPyCl 100, and does not affect the dependency of the final swell radius a_2 on H^* and Q^*.

In addition, the reverse swell process takes place on a height h, determined by the balance between the characteristic speed for the flow downward in the swollen region, which can be averaged to $Q/\pi a_1 a_2$, and for the upward propagation of viscous effects, ν/h. Using (5.24), this leads to the following dimensionless expression for h

$$h^* = \frac{h}{l_{VG}} \sim \left(\frac{a_0^{*4}}{H^{*2}Q^*} \right)^{1/3} \tag{5.26}$$

which is verified for most series of experiments figure 4-10 (d). This can be written in dimensional term as

$$h \sim \left(\frac{a_0^4}{H^2 Q} \right)^{1/3} \left(\frac{\nu_0^7}{g^2} \right)^{1/9} \tag{5.27}$$

Everything else being equal, h scales as $\nu_0^{7/9}$. This means that low-viscosity viscoelastic fluids will display a sharp reverse swell, whereas for very viscous viscoelastic fluids it will not be really noticeable. For example, for $a_0 = 1.25$ mm, $H = 9$ cm, $Q = 2$ mL/min (which are typical values at which reverse swell is seen with CPyCl 100) and the viscosity values given in Table 3.1, the height of the reverse swell is of the order of 5 mm for CPyCl 100 and 1.6 cm for Boger fluids. Since the lateral extent of the swell, given by $a_2 - a_1$, is of the order of the millimeter, the swell is not visible within experimental error for Boger fluids. Another way to say the same thing is to derive the swell slope, $s = (a_2 - a_1)/h$, using (5.25) and (5.27). In the limit of $a_2 \gg a_1$ (which is a rather strong approximation) we obtain

$$s = (a_2 - a_1)/h \sim \frac{(HQ)^{1/2} g^{1/9}}{a_0^{2/3} \nu_0^{13/18}} \tag{5.28}$$

Equation (5.28) has a limited validity because of the assumption $a_2 \gg a_1$ is not true in most cases, however, it underlines that experimentally noticeable reverse swell require a fluid with a viscosity as low as possible. Since elasticity is important as well from the condition (5.18), fluids such as CPyCl 75 or CPyCl 100 are ideally suited to observe reverse, in contrast with high viscosity fluids such as the Boger fluid or low elasticity fluids such as commercial

83

shampoos.

In addition, a larger value of h means that an increased time in the swell is available for the macromolecules to relax, which may invalidate the purely elastic recovery assumption used to derive (5.21). As a result, it is not possible at the present time to be certain whether very viscous viscoelastic fluids such as Boger are not prone to reverse swell at all, or if it is simply not experimentally noticeable. For example, Chai and Yeow[63] studied the shape of jets of Boger fluid and found a small widening at the base, although the bottom boundary condition is a bit different from here: the jet was falling straight into a pool of the same liquid and was not buckled. Testing the mechanism described in this section would rather require the use of a fluid different from CPyCl but with comparable features of significant elasticity, especially large elastic component of extensional stress, and moderate or low viscosity.

5.2 Scaling laws of jet motion

5.2.1 Folding mechanism

The mechanism of folding of CPyCl wormlike micellar solution has different roots from Newtonian coiling. Even when the jet is pushed sideways, experimental observations show that it remains relatively straight (figure 5-1 (a)), whereas Newtonian jets were bent and twisted over a significant height from the bottom plate. This is allowed by the shear-thinning properties of the fluid which limit the shear stress in the curved region, as shown on figure 5-1 (c), and it is likely that shear banding takes place in that process. The shear stress $\eta(\dot{\gamma})\dot{\gamma}$ in the curved region is bounded by η_0/λ, as shown on figure 3-3 (c), regardless of the curvature, whereas it scaled with the curvature squared in the Newtonian case (equation (2.13)). The point of contact of the jet with the lower layer of fluid can therefore be in line with the centerline of the jet, and moves at the same pace as the rest of the jet. Since it is not twisted the jet does not coil and follows a straight motion.

As the jet translates further and further sideways the weight of the inclined jet tends to pull it back toward the vertical axis. This creates a bending torque within the jet, and it is resisted by a viscous torque that appears when the lower part of the jet bends (figure 5-1 (d)).
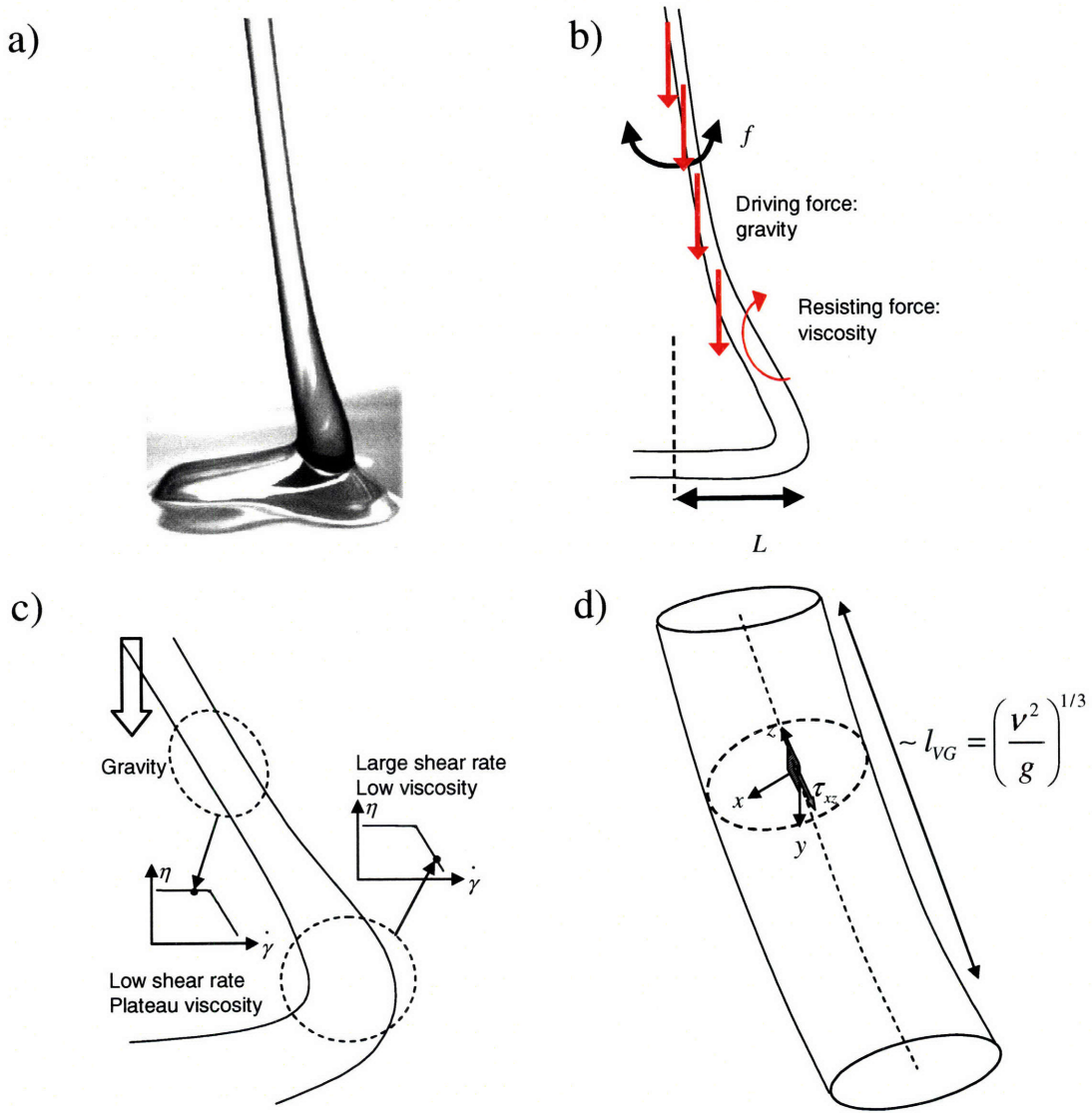
Figure 5-1: Different views of folding mechanism. a) View of a CPyCl jet at the farthest position. b) Schematic view of folding mechanism: the jet tends to fall vertically under its own weight, which is resisted by a viscous torque c) At the farthest position of the oscillation, just at the onset of buckling of the main part of the jet under the weight of the jet, the fluid is not sheared, whereas the contact zone with the fluid layer is in highly shear-thinning or shear-banding conditions. d) Close-up of the buckled region of the jet, in which curvature induces shear stress τ_{xz}

When the jet reaches its maximum amplitude L, the gravitational torque becomes larger than the viscous torque, and the jet buckles back toward the center line. Such a situation is shown on figure 5-1 (b). The jet then makes a new contact point with the layer of liquid, continues its movement because of the steady incoming flow of fluid, and the process repeat itself. It is now possible to analyze what happens at the extremal point of this motion in order to derive scaling laws for the amplitude and frequency of folding. This analysis is similar to the scaling laws developed in Skorobogatiy and Mahadevan (2000)[32], except that here, the fact that the jet is straighter changes slightly the relevant scales.

5.2.2 Theoretical folding scaling laws

Connection between amplitude and frequency

The maximum amplitude of folding is given by the balance between a driving torque that tends to bend the jet, and a viscous torque that resists it. The frequency of folding is directly linked to the amplitude through the horizontal velocity U_3 of the contact point of the jet with the fluid layer by $fL \sim U_3$. This horizontal velocity U_3 can be roughly estimated as the horizontal component of $U_2 = Q/\pi a_2^2$: it is approximately zero when the jet is vertical, and largest when it approaches L. This feature can be checked on the laser trajectory of figure 4-3 (c): two successive points on the trajectory are approximately separated by the same amount of time, and they are much closer in the center of the trajectory than on its sides, thus confirming a lower horizontal velocity close to the vertical axis. This lower velocity is the most relevant to characterize U_3, and it scales as $U_2 a_2/L$. As a result f and L are linked by

$$fL \sim U_2 \frac{a_2}{L} \Rightarrow f \sim \frac{Q}{L^2 a_2} \tag{5.29}$$

Various regimes exist depending on which force dominates in the jet. The possible driving forces are either viscosity, gravity, or inertia. The resisting force is always viscosity. Table 5.1 summarizes the influence of H^* and Q^* in all cases encountered, theoretically as well as experimentally. It also provides a reminder of the scaling laws for Newtonian coiling in nondimensional terms, in order to compare the two types of motion.

Viscous regime

As for Newtonian fluids, at low heights of fall, the driving force for folding is the viscous stress in the fluid near the nozzle. As for viscous coiling, the range of heights of fall of viscous folding will be limited by both buckling height and transition to gravitational folding, and may not be observable. In the cases where viscous folding occurs, no gravitational stretching occur, so $a_0 = a_1 = a_2$. In this regime the jet amplitude is geometrically constrained by the nozzle-plate distance H, which means that

$$L_V \sim H \tag{5.30}$$

The expression for frequency is found using (5.29):

$$f_V \sim \frac{Q}{H^2 a_0} \tag{5.31}$$

In the viscous regime the motion of the jet is therefore totally constrained by the external parameters of the experimental setup, rather than fluid properties.

Gravitational regime

For larger heights of fall, the driving torque is a gravitational torque acting on an arm given by the extremal position L. This torque scales as

$$T_{driving} \sim \rho g H a_1^2 L_G \tag{5.32}$$

At the maximum amplitude L the jet falls backward, bending on the length scale l_{VG} typical of the opposing influence of gravity and viscosity. The typical curvature of the jet just at that moment is of the order of $\kappa = 1/L$, and this leads to shear motion within the curved region, with viscous stresses that develop between the outer region of larger velocity and the inner region. The viscous stress in this situation, τ_{xz}, is the direct analog of the elastic stress in beam bending: it vanishes in the middle of the jet and increases linearly along the cross-section. Following this analogy in the fashion developed in [32], the stress is written

$$\tau_{xz} = \eta_0 \dot{\gamma} \sim \eta_0 x \dot{\kappa} \sim \eta_0 \frac{x}{L_G} \frac{Q}{a_1^2 l_{VG}} \tag{5.33}$$

Note that at the very onset of bending, the liquid is not sheared, therefore the zero-shear viscosity is used. As expected the viscous force $d^2F_V = \tau_{xz}dxdy$ integrated over the jet cross-section vanishes. The elementary viscous torque, $\delta^2T_V = x\tau_{xz}dxdy$, nevertheless, remains non-zero after integration. Approximating the cross-section to a square, the resulting torque is

$$T_{resisting} \sim \int_{-a_1}^{a_1}\int_{-a_1}^{a_1} x\tau_{xz}dxdy = \eta_0\frac{a_1^2Q}{l_{VG}L_G} \tag{5.34}$$

The balance between the two torques gives a scaling law for the amplitude of folding

$$L_G \sim \left(\frac{\nu_0Q}{l_{VG}gH}\right)^{1/2} \tag{5.35}$$

In dimensionless form, we obtain the following scaling law

$$L_G^* \sim \left(\frac{Q^*}{H^*}\right)^{1/2} \tag{5.36}$$

The expression for a_2 in (5.29) is found using (5.24), which leads to a dimensionless expression for the frequency in this regime:

$$f_G^* \sim \frac{\left(Q^{*5}H^*\right)^{1/6}}{a_0^{*2/3}L_G^{*2}} \tag{5.37}$$

We can then derive the dimensionless folding frequency in gravitational regime:

$$f_G^* \sim \frac{1}{a_0^{*2/3}}\left(\frac{H^{*7}}{Q^*}\right)^{1/6} \tag{5.38}$$

The transition between viscous and gravitational regimes takes place for $\beta = Ha_0\sqrt{g/6Q\nu} > \pi/2$ from equation (2.6). For CPyCl 100, $a_0 = 1.25$ mm, and $Q = 3$ mL/min, this is equivalent to $H = 3.3$ cm. Once again, at low flow rate, the jet may transition directly from steady flow to gravitational coiling, as will be shown in the next section in figure 5-3.

Inertial regime

In contrast to the inertial regime for coiling ([5] and [6]), the type of inertia that drives folding is not the centrifugal (rotational) inertia but the linear, axial inertia. The fluid in the jet tends to travel along a vertical path, witch provides a restoring force returning the folded part of the jet toward the center. The inertial force per unit length is $\rho Q^2 / a_1^2$, which leads to a torque that scales as

$$T_{driving} \sim \frac{\rho L_I Q^2}{a_1^2} \tag{5.39}$$

In this regime the length of the bent region is much smaller than for the gravitational regime, and scales with L rather than l_{VG}. This leads to a viscous torque that scales as

$$T_{resisting} \sim \eta_0 \frac{a_1^2 Q}{L_I^2} \tag{5.40}$$

This leads to a folding amplitude that scales as

$$L_I \sim \left(\nu_0 \frac{a_1^4}{Q} \right)^{1/3} \tag{5.41}$$

In dimensionless terms and using (5.23), this is written

$$L_I^* \sim \left(\frac{Q^*}{H^{*2}} \right)^{1/3} \tag{5.42}$$

The equation (5.37) is once again used to obtain the scaling for folding frequency:

$$f_I^* \sim \frac{H^{*3/2} Q^{*1/6}}{a_0^{*2/3}} \tag{5.43}$$

The inertial regime is expected to appear at large heights, of the order of heights required to have $\rho Q^2 / a_1^2 \sim \rho g H a_1^2$ or, with CPyCl 100 values, $H \approx 9\nu_0^2/(gl^2) = 26.5$ cm. In addition, the inertial force $\rho Q^2 / a_1^2$ scales as HQ (using (2.8)): the inertial force is therefore increasing toward the upper right-hand-side corner of the regime diagrams such as figure 4-7. Nevertheless, at these heights, thermal effects are very important, which affects dramatically the viscosity. For this reason, no systematic quantitative measurement has been conducted in this regime.

Qualitatively, the jet shown on figure 4-5 (d) is a good example of inertial regime, with a straight, vertical jet and a very small folding amplitude.

5.2.3 Comments and comparison with experimental results

The dependency on the height of fall, flow rate, and nozzle radius of the measured variables of the jet motion dynamics are summarized in Table 5.1. The frequency and radius for the coiling motion of Newtonian jets has been gathered from the equation (2.14a) to (2.16b), while the frequency and amplitude for the folding motion of CPyCl jets is taken from the equations (5.30) to (5.43). The last row of Table 5.1 is the experimental scaling law found for the folding of CPyCl 100 in gravitational regime.

The first point to make from the observation of Table 5.1 is that motion in coiling and folding share overall the same trends. Despite being based on quite different mechanisms, both modes see their frequency and amplitude evolve in the same direction with respect to either height of fall or flow rate in most cases, even if the values of the scaling exponents are different. One of the main difference between coiling and folding in the influence of height of fall within the gravitational regime: whereas coil radius does not change significantly with height of fall, the fold amplitude decrease as the square root of height of fall.

Folding experiments performed for this study fall mostly within the gravitational regime. At the larger heights required for the inertial regime, significant evaporation cools the fluid and substantially underestimates the scaling of viscosity by ν_0; in many experiments we see that the fluid dries or undergoes surfactant precipitation which leads to a brittle fracture. The viscous regime is constrained between buckling and transition to gravitational folding, and the low heights involved makes both frequency and amplitude measurements imprecise. In the gravitational regime, a large scatter was observed between the scaling exponents of the various series of experiments, due to the sensitivity of CPyCl solutions to several external factors difficult to control. One of the most important source of variation is possible pre-shear in the syringe, the tube, and the nozzle, and pre-shear is known to have a significant impact on extensional rheology for micellar solutions [64]. Other factors include the ambient temperature and relative humidity which control evaporation, possible aging of the solutions

used, and variations in fluid preparation from batch to batch. Despite these limitations, the overall scaling dependency, obtained from the collapse of all the data at the same time in figure 4-12 and reported in Table 5.1, is in fairly good agreement with theoretical predictions, which fall within the ranges of experimental exponents given in Table 4.1.

	Frequency	Radius/Amplitude
Viscous Coiling	$H^{-1}Qa_0^{-2}$	H
Gravitational Coiling	$H^2Q^{-1/4}$	$Q^{1/4}$
Inertial Coiling	$H^{10/3}Q^{-1/3}$	$H^{-4/3}Q^{1/3}$
Viscous Folding	$H^{-2}Qa_0^{-1}$	H
Gravitational Folding	$H^{7/6}Q^{-1/6}a_0^{-2/3}$	$H^{-1/2}Q^{1/2}$
Inertial Folding	$H^{3/2}Q^{1/6}a_0^{-2/3}$	$H^{-2/3}Q^{1/3}$
Experiments Folding	$H^{0.66}Q^{-0.19}$	$H^{-0.50}Q^{0.60}$

Table 5.1: Theoretical scaling laws for the different motions and regimes, with respect to height of fall, flow rate and radius.

5.3 Analysis of regime maps

5.3.1 Newtonian fluids

Based on previous studies and experimental map of figure 4-6 (a), we can draw a schematic two-dimensional regime map for circular jets of Newtonian fluids (figure 5-2). The line (a) is the buckling transition, and our experimental data are consistent with the prediction by Cruickshank[27] given in equation (2.9a).

The dripping-jetting transition for a jet falling on a plate from a distance H (line (b)), has not been considered in the literature, to our knowledge. It is, for example, different from the dripping-jetting transition at the nozzle without taking into account what happens downstreams considered by Clanet and Lasheras[10]. The transition happens because of the destabilizing effect of surface tension, which tend to increase the amplitude of any perturbation on the jet radius. In all generality, it requires that the residence time of any fluid particle in the jet be larger than the timescale on which the destabilization takes place. Based on this idea, it is possible to derive a criteria for the dripping transition, by approximating the jet falling on a
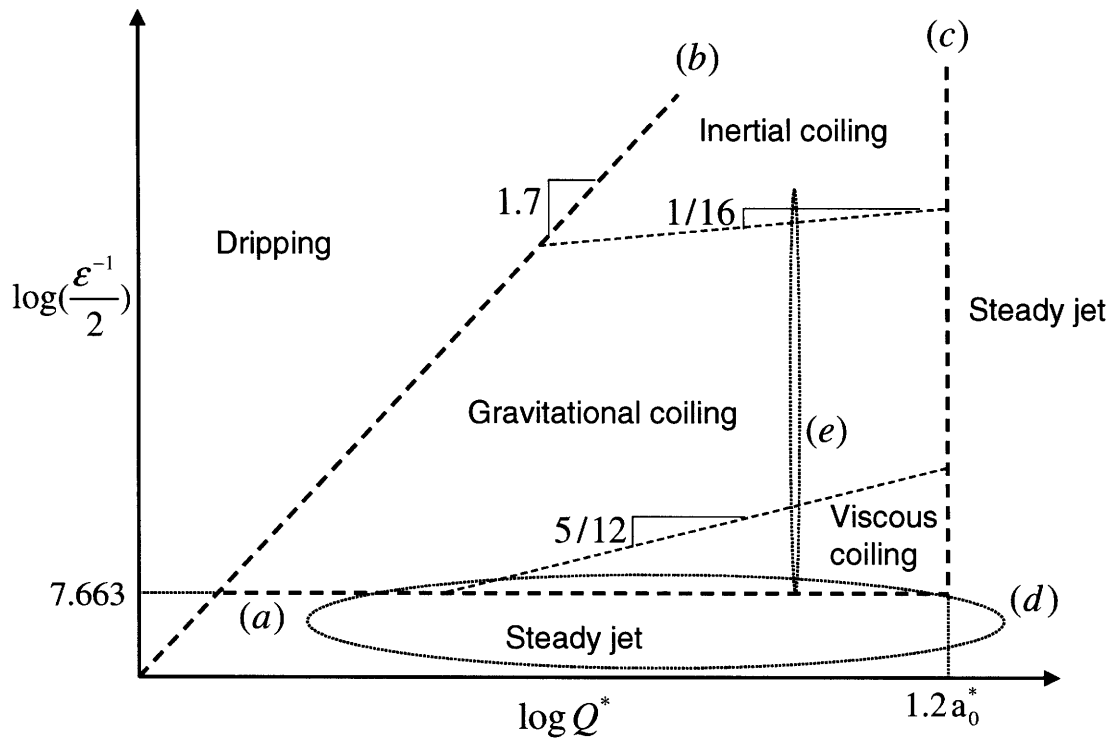
Figure 5-2: Schematic regime map for a circular jet of Newtonian fluid, for a given value of $a_0^* = a_0(g/\nu^2)^{1/3}$, in the space of the parameters $Q^* = Q(g/\nu^5)^{1/3}$ and $\epsilon^{-1}/2 = H/2a_0$.

plate from a height H to the upper portion of length H of a free-falling jet. If destabilization happens during the time required for the jet to flow on that length, then the jet falling on a plate can be considered destabilized as well. Note that both the destabilizing effect of the lower part of the free-falling jet, that pulls fluid out of the upper part, and the stabilizing effect of the bottom plate, that has the opposite effect, are neglected in this approximation. Therefore, it is expected that the following scaling laws will tend to *favor* the dripping regime in comparison to experiments.

This transition can take place along several lines depending on which forces resists the destabilization process. In the case of viscous silicone oil, the residence time of a fluid particle in the jet is of the order of $a_0^2 H/Q$, while the characteristic time before capillary instabilities break the jet into droplets is $t_{visc-cap} = 14.1a_0\eta_0/\sigma$. Omitting the multiplying constant, an estimate for this transition is therefore

$$\frac{a_0^2 H}{Q} \sim \frac{a_0 \eta_0}{\sigma}$$

$$H \sim \frac{Q\eta_0}{\sigma a_0} \tag{5.44a}$$

This can be re-arranged in dimensionless terms:

$$\epsilon_{dripping}^{-1} \sim \frac{Q^* Oh^2}{a_0^*} \tag{5.45}$$

This indeed overestimates the dripping: the required flow rate for continuous jet scales here as $H \sim Q$, compared to $H \sim Q^{1.7}$ experimentally.

The line (c), given by equation (2.10), represent the maximum flow rate above which no instability arises because inertia dominates over viscous effects. One a side note, the "stable jet" regime is of industrial importance, because it avoids any problematic instability.

The zone (d) of the map is the area of the parameter space covered by studies on steady jetting[24] and jet buckling[3]. The zone (e) shows the area covered by investigations of coiling behavior as a function of height of fall ([5], [6])

The slope of the two lines separating the viscous, gravitational and inertial regime of coiling

have been calculated as Ω_G/Ω_V and Ω_I/Ω_G being held constant, using scaling expressions derived by Ribe[6] and listed in equation (2.14b) to (2.16b). The transition between viscous and gravitational coiling is given by

$$\frac{\Omega_G}{\Omega_V} \sim H^3 a_0^2 \left(\frac{g}{\nu Q}\right)^{5/4} = \text{constant}$$

$$H \sim \frac{1}{a_0^{2/3}} \left(\frac{\nu Q}{g}\right)^{5/12}$$

$$\epsilon^{-1} \sim \frac{Q^{*5/12}}{a_0^{*5/3}} \tag{5.46}$$

The transition between gravitational and inertial coiling regimes occur at a larger height of fall, that scales with flow rate according to the following scaling law:

$$\frac{\Omega_I}{\Omega_G} \sim \frac{H^{4/3} g^{5/12}}{\nu^{3/4} Q^{1/12}} = \text{constant}$$

$$H \sim \left(\frac{\nu^9 Q}{g^5}\right)^{1/16}$$

$$\epsilon^{-1} \sim Q^{*1/16} \tag{5.47}$$

Nevertheless, no experimental confirmation for these boundaries has been made in this thesis, and only the coiling regime is reported on figure 4-6 (a). The transition between the coiling regimes has been studied by Ribe[6], including the multivalued frequency at the gravito-inertial transition[31] Note that it is also possible that the jet transitions directly from steady jet to gravitational coiling, especially at low flow rate, as can be seen on the schematic map of figure 5-3.

5.3.2 CPyCl solutions

Based on the experimental data gathered on the experimental the map (figure 4-7) and quantitative measurements (figure 4-8), we can draw a schematic regime map for CPyCl jets, shown on figure 5-3.

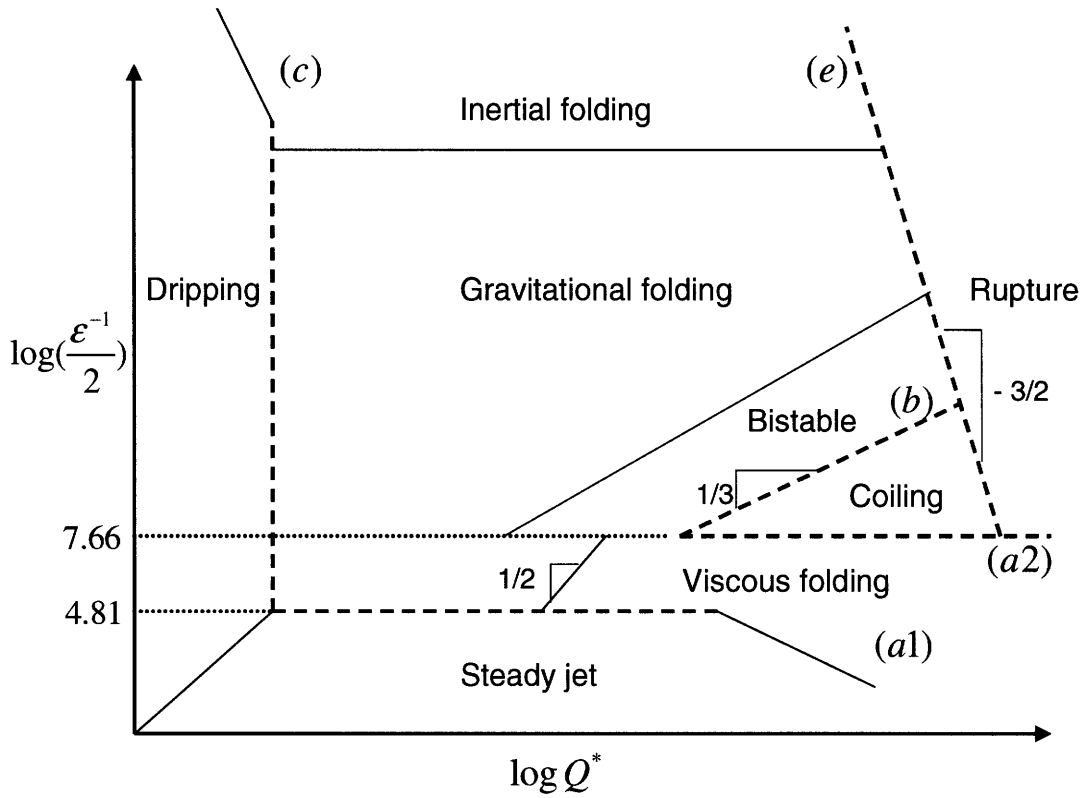Figure 5-3: Schematical regime space for a circular jet of CPyCl jet, for a given value of $a_0^* = a_0(g/\nu^2)^{1/3}$, in the space of the parameters $Q^* = Q(g/\nu^5)^{1/3}$ and $\epsilon^{-1}/2 = H/2a_0$. Thick, dashed lines are regime transitions based on figure 4-7 and the scaling laws of figure 4-8. Thin, continuous lines are less-investigated transitions or based on theoretical predictions only.

Buckling transition

In our experiment the buckling transition, shown on the schematic map 5-3, line (a1), always happens from stable jet to folding when height is increased, and for a critical height close to the prediction of equation (2.9b) established for Newtonian fluids, as shown on figure 4-8 (a). For Newtonian fluids, this transition from stable jet to folding was observed either in a transient fashion or in a narrow range of conditions listed in equation (4.11), whereas it takes place in all three solutions CPyCl 75, 100 and 150, and for the three sizes of nozzle. We understand it by incorporating the effect of shear-thinning that stabilizes folding by reducing the viscous torque in that geometry. Non-Newtonian effects in this situation can be characterized by a Weissenberg number $Wi_{buckling} = \lambda Q / \pi a_0^3$. Since $Wi_{buckling} \approx 1 - 10$ for the range of experiments studied here, shear thinning indeed takes place.

The small value of the aspect ratio ϵ^{-1} at this transition makes it important to take into account the die-swell effect, therefore, the vertical axis of the figures 4-8 (a) and (b) are the aspect ratio redefined as $\epsilon^{-1} = H/a_{swell}$, where a_{swell} is calculated with (5.16). Despite that correction, we still note that for CPyCl 100 and the smallest nozzle (symbols ($\square$) in figure 4-8 (a)), the required aspect ratio for the transition from steady jetting to buckling increases with the flow rate.

First coiling-folding transition

A second transition between folding and coiling mode happens when the height of fall is increased (figure 5-3, line (a2)). As was mentioned in [27], the measurement of that transition is complicated by the large range of aspect ratios for which the jet is bistable and switches back and forth between the two modes. Nevertheless, despite the scattering of the data, it appears clearly on figure 4-8 (b) that the transition happens roughly at the aspect ratio predicted by (2.9a). The standard deviation on the buckling aspect ratios is below 50%, while at the same time Q^* changes by three orders of magnitude.

Second folding-coiling transition

At an even larger height, another transition happens (figure 5-3, line (b)), from coiling back to folding mode (figure 5-3, line (b)). Experimental results are presented in figure 4-8 (c). The respective stability of the two periodic regimes can be obtained by comparing the two viscous torques that would occur in each case, forming their ratio K. For $K < 1$, coiling is favored, otherwise folding is dominant. The folding torque is already known from (5.34). The coiling torque must be written using the folding amplitude L_G, or, in other word, we consider the viscous torque that would develop if the *folding* jet at its maximum amplitude L_G initiated a *coiling* motion. The expression for K is therefore :

$$K = \frac{T_{resting_{coiling}}}{T_{resting_{folding}}} = \frac{\eta_0 Q a_1^2 / L_G^2}{\eta_0 a_1^2 Q / l_{VG} L_G} = \frac{l_{VG}}{L_G} = \frac{1}{L_G^*} \tag{5.48}$$

Using equation (5.36), we obtain the following scaling for the folding-coiling transition

$$K \sim \left(\frac{Q^*}{H^*}\right)^{1/2} \tag{5.49}$$

The transition happens for $K \approx 1$, or for

$$H^*_{folding-coiling} \sim Q^* \tag{5.50}$$

This simple, first order model does not take into account the specificity of coiling of CPyCl jets. For example, because of the straighter jet allowed by shear thinning, the viscous stress in a coiling micellar jet may be different from what has been developped for Newtonian coiling. As a result, it does not capture very well the trend of the transition which scales as $H^*_{Transition} \sim Q^{*\,1/3}$, as measured on figure 4-8 (c).

Dripping-jetting transition

It is understood, as described in the experimental section, that the dripping-jetting transition does not necessarily means jet breakup, because viscoelastic fluids tend to leave thin connecting threads that resist breakup. In case of viscoelastic solutions forming long threads, the transition to non-continuous phase is triggered when the flow rate is not sufficient to overcome the elasto-

capillary thinning (figure 5-3, line (c)). In this case, the thinning rate is given by $1/3\lambda$ (from equation (3.7)), while the characteristic residence time is given by $\tau_{res} \sim Ha_{thread}^2/Q$, where a_{thread} is the radius of the filament. For moderate values of ϵ^{-1}, this can be found by picturing a drop of fluid existing the nozzle of volume a_0^3, being stretched into a filament of volume Ha_{thread}^2. This leads to a residence time $\tau_{res} \sim a_0^3/Q$. The timescale balance leads to a dripping-jetting transition independent of height of fall:

$$Q_{continuous} \sim a_0^3/\lambda \tag{5.51}$$

This crude estimate captures the transition from dripping to jetting at a constant flow rate in the case of CPyCl solutions. As the elasticity of the solution increases, a progressively lower flow rate is required. Nevertheless, it is expected that at large height of fall, evaporation cooling will slow down breakup, thus requiring even less fluid flow. Indeed, this trend can be seen on figure 4-7.

Large-flow rate ductile failure

Large flow rate jet breakup (figure 5-3, line (e)) happens at the nozzle, and the required flow rate decreases with the height of fall. This suggests that breakup occurs when the weight of the fluid in the jet becomes larger than the maximum stress that the micelles are able to sustain. The weight of fluid in the jet is of the order of $a_{swell}a_1 H\rho g \sim \sqrt{HQ}$. This leads to a scaling of the required flow rate for breakup that scales with height of fall as

$$Q_{failure} \sim H^{-1} \tag{5.52}$$

This is a slightly more pronounced dependency than the experimental scaling from figure 4-8 (d) of $Q_{failure} \sim H^{-0.65}$. It is possible that neglecting dynamic effects such as gravitational acceleration and shear banding at the nozzle at large flow rate has diminished the importance of the flow rate on the stress at the nozzle. Taking them into account may lead to an exponent closer to experimental values.
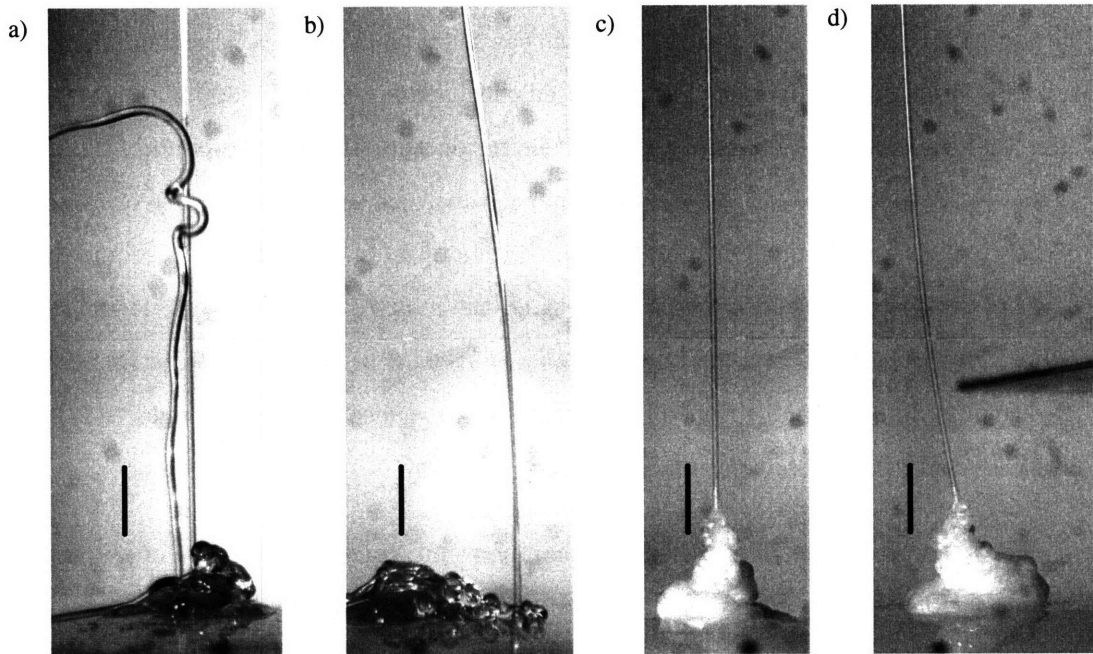
Figure 5-4: Views of jets of commercial shampoos (Herbal Essence (a, b) and Pantene Classic (c, d)) at large height of fall and flow rate, $Q = 25$ mL/min, $H = 24$ cm ($Q^* = 8.2 \times 10^{-4}$, $H^* = 7.8$ for Herbal, $Q^* = 13 \times 10^{-4}$, $H^* = 9.4$ for Pantene). Herbal shampoo shows Kaye effect (a) whereas Pantene Shampoo & Conditioner does not (c). Both jets are deviated when approaching a ruler rubbed on a cloth and charged with a static charge (b, d). Black bars are 1cm high.

5.3.3 Shampoo and shampoo bases

Dripping transition of shampoo bases

The dripping transition of SB 1.8 (figure 4-6 b) is similar to what happens for Newtonian fluids, although with a smaller slope. The dripping-jetting limit is given by $Q^* \sim H^*$, which means that dripping is favored in comparison to Newtonian fluids such as silicone oil, which can be understood as the destabilizing effect of shear-thinning

Kaye effect

In the Kaye effect, the expelled jet is actually the continuation of the incoming jet, "sliding" on a thin layer of fluid of low viscosity and turning upward on the side of liquid heap. As can

be seen on figure 4-6 (c), the Kaye effect takes place at large values of ϵ^{-1} and Q^*, that is, at large terminal jet velocity. Shear-thinning has been identified by Versluis and co-workers[39] as a required fluid property. The proposed mechanism was that jets of viscous fluids would first build a mound, followed by the jet sliding on the side on the mound. The momentum of the impacting jet would dig a spoon shape, which causes the trajectory of the outgoing jet to reach higher and higher heights. In this mechanism, shear-thinning is required to create a layer of low-viscosity fluid between the jet and the mound, acting as a lubricant. Nevertheless, other fluid properties or experimental conditions may be necessary as well, because not all shear-thinning fluids undergo the Kaye effect. Intense shear-thinning should thus be viewed as a necessary but not sufficient condition.

For example, while Herbal Essence shampoo and Pantene Classic shampoo & conditioner have extremely similar shear and extension rheology (figure 3-9 c and d) and characteristic fluid properties (Table 3.1), the former does undergo the Kaye effect (figure 5-4 a) but the latter does not (figure 5-4 c). A tentative hypothesis could have been that because of slight differences in chemical formulation, one jet would get electrostatically charged with static as it travels through the air, and that electrostatic repulsion near the mound would help starting the Kaye effect. In this hypothesis, electrostatics would be involved in this onset of the Kaye effect, while shear-thinning would be the required condition for sustaining it. Nevertheless, direct voltage or static charge measurements or grounding are difficult because of the small dimension and the fluid nature of the jet, and a simple electrostatic attraction with a plastic ruler rubbed on a cloth shows no difference between the two jets (figure 5-4 b and d).

The last hypothesis to explain why Pantene 2-in-1 shampoo and conditioner do not leap despite having the same rheological properties as Herbal shampoo is the existence of a damper in conditioner formulation that would dissipate incoming kinetic energy.

Chapter 6

Conclusion

After presenting the existing knowledge on jets of Newtonian fluids and describing non-Newtonian fluids and especially the wormlike micellar fluids, we have underlined the strong industrial interest for the investigation of the behavior of non-Newtonian fluids falling on a plate. Rheological properties of wormlike micellar solutions were characterized, along with other fluids, a silicone oil as a Newtonian reference, a viscoelastic but not shear-thinning Boger fluid, and a number of industrially relevant shampoo products. Two experimental setups were described for the study of jets and, with the help of a suitable nondimensionalizing scheme, we obtained several types of results. First a number of jetting regimes were qualitatively described, and the influence of the rheological properties of the different fluids on their jetting behavior was made clear. These regimes were mapped in the appropriate parameter space with a special emphasis on the transitions between regimes. Subsequently, the novel features of non-Newtonian wormilke micellar jets were investigated quantitatively, especially their shape, with a reverse swell that does not exist for Newtonian fluid, and their dynamics, with a folding regime that is not observed with cylindrical jets of Newtonian and Boger fluids. Theoretical mechanisms were suggested in each case, and the scaling laws derived from them compared well with experimental results, thus providing a good understanding of a several features of non-Newtonian jets.

We also investigated the Kaye effect, in which a jet of shampoo "leaps" sometimes up to heights two orders of magnitude larger than the jet radius. We showed that the shear-thinning criteria proposed by Versluis[39] is a required, but not sufficient, condition for the Kaye effect

to take place. Two commercial shampoos with very similar rheological properties in both shear and extension showed different behavior: one was very prone to leaping while the other one.was not. Therefore, additional mechanisms different from rheological arguments seem to be needed to fully explain the Kaye effect.

6.1 Jets of wormlike micelles

Jets of non-Newtonian fluids impacting on a plate are shown to behave in a qualitatively different fashion from their viscous analog. Wormlike micellar solution jets especially have a distinct shape, with a reverse swell that, to our knowledge, has never previously described. Jet motion was also qualitatively different, with a back-and-forth folding motion obtained from a round jet, which has only been observed previously in naturally 2D systems such as a planar jet or a jet confined in a plane.

Wormlike micellar fluids falling on a plate can undergo several different jetting behaviors. At low flow rates, the jet is not continuous, and the increased extensional viscosity over Newtonian fluids leads to the creation of a thin thread that resists breakup (figure 4-1 (d)). As long as the imposed flow rate is sufficient to prevent the eventual, the jet will appear continuous, regardless of the height of fall. This is in marked difference with Newtonian fluids where the required flow rate increased with height.

At low aspect ratios, the jet is steady, as is observed for Newtonian jets [24]. The buckling transition between the low-height, axisymmetric situation, and the time-dependent regime, is interpreted in terms of the Newtonian perturbation analysis developped by Cruickshank[27]. The transition between steady jet and periodic motion happens in a folding mode that was not stable in most cases with Newtonian fluids, but that is stabilized by the effect of the shear-thinning property of the solution.

After buckling, the motion of wormlike micellar jets is different from Newtonian jets, which only show coiling around the vertical axis ([3], [5] and [6]). Wormlike micellar fluids above the buckling limit can either coil or fold back and forth in a pendular motion confined to an axial plane (figure 4-3), depending on the experimental conditions. This can be rationalized by the

shear-thinning property of the solution, which allows for a straight jet without twisting torques leading to coiling in the Newtonian case. The scaling analysis provided in Chapter 5 captures well the evolution of folding frequency and amplitude with experimental parameters. As the height of fall is progressively raised from the steady jet regime above the buckling transition, the jet begins by folding. At a larger height, a second transition between the folding and coiling mode happens at a critical aspect ratio that is similar to the buckling aspect ratio for Newtonian fluids[27]. At an even larger heights of fall that increases with the flow rate, a third transition takes place, from coiling back to folding. This contrasts with both jets of fluids of constant viscosity such as Newtonian and Boger fluids and elastic ropes [35], which are steadily coiling around the vertical axis in the time-dependent regime. The experimental investigation of these transitions is shown in figures 4-7 and 4-8, and a schematic overview is presented in figure 5-3.

Another feature of wormlike micellar jets is the abrupt widening at their base, which we refer to as reverse swell. As can be seen on figure 4-11, a sharp and pronounced reverse swell is a feature that was unique to CPyCl solutions among our test fluids. The reverse swell phenomenon is reminiscent of die-swell and we explained it by the relaxation of elastic stresses in the jet stored during gravitational acceleration and stretching. The theoretical prediction of the amount of swelling of equation (5.22) is verified experimentally (figure 4-10 (c)).It is interesting to note that while the thinning in the top part of the jet is well predicted by a balance between gravitational and viscous forces as in the Newtonian case, predicting the reverse swell requires the use of a rubber-like approximation similar to elastic solid. This underlines how novel features of jets emerge from the specific non-Newtonian rheological properties of the fluid used.

6.2   Applicability to industrial problems

The present contribution is connected to industrial problems in several ways. It is obviously directly applicable to concentrated surfactant solutions forming wormlike micelles, as well as other viscoelastic fluids ubiquitous in food and cosmetic industries. Since very large flow rates and deformation rates are used in industry, some behaviors described here for moderate flow rates may not be relevant. Nevertheless, insights in low flow rate behavior, and especially

the connection between extensional viscosity and ability to resist breakup, can be useful to understand "stringiness" in consumer products. It can also help to prevent spills occurring when a thin string or filament of fluid remains between nozzle and bottle after filling. Another direct application of the regime maps we provide is that buckling limits can be seen as universal, which may be used as a design criteria for diving nozzle.

In a more general fashion, the framework developed here could be use to study any other type of fluid. The nondimensionalizing scheme and the idea of mapping instabilities on regime diagrams shown in Chapter 4 , as well as the physical mechanisms described in Chapter 5, can also be applied to yield stress materials such as pastes or concentrated emulsions, to gels, foams, etc. Although the actual dynamics of the jetting behaviors may not be the same as for CPyCl solutions, the same tools can be used to explore them. Shear rheology can be connected to the torques controlling the jet instabilities, and extensional rheology determines whether the fluid tends to jet or form drops.

Another contribution of this work is the investigation of large-amplitude events, chaotic motion, and the Kaye effect, of shampoo jets. These phenomena are linked to industrial problems such as incomplete filling, air entrapment, and spills, in situations such as the filling of shampoo bottles.

6.3   Future work

Several suggestions for improvements and extensions can be made from this study. First of all, CPyCl solutions could not be studied at large heights, because the jet becomes so thin that evaporative cooling as well as air currents dramatically affects its properties and motion. These problems could be at least partially alleviated by using an air-tight enclosure with a controlled atmosphere maintaining a high humidity.

A second point is that the theoretical tools such as the dimensionless framework presented in this study can be used for any other fluid. It has been pointed out that fluids only need sufficient extensional viscosity in order to form jets at low Reynolds number, therefore many non-Newtonian fluids could be used, such as polymer solutions or colloidal suspensions.

In addition, the principle on which this work is based, extending Newtonian-only experiments to different non-Newtonian fluids, could be applied elsewhere; for example to on Pouligny's study of air entrapment in silicone oil folds[4]. The relevance of non-Newtonian fluids in food, cosmetic, oil, or healthcare industry, has already been underlined, and entrapment of air bubbles is a major industrial concern[44].

The theoretical explanation of reverse swell led to the conclusion that all fluids with low viscosity but a large elastic component in extension should display a reverse swell similar to CPyCl solutions. It has not been possible to test this hypothesis with shampoo bases that are insufficiently elastic, or with a Boger fluid which is too viscous. The investigation of polymer solutions with rheological properties somewhat similar to CPyCl 100 could represent a good test for this theory.

From a theoretical point of view, a more thorough analysis could look at combining the Newtonian equations developed by Mahadevan[5] and Ribe[6] with non-Newtonian constitutive equations. This could provide equations allowing the computation of the jet shape and dynamics of jet motion for different fluids.

Lastly, for the problem of Kaye effect, a more systematic investigation of the phenomenon for different fluids could help in explaining why shear-thinning fluids do not necessarily lead to jumping jet, in spite of Versluis' general predictions[39].

Bibliography

[1] Lord Rayleigh, On the stability of a cylinder of viscous fluid under a capillary force," *Philos. Mag.* 34, 145 (1892).

[2] Lord Rayleigh, On the theory of long waves and bores, *Proc. R. Soc. Lond. A* 90, 324.(1914)

[3] J. O. Cruickshank, B. R. Munson, Viscous fluid buckling of plane and axisymmetric jets, *J. Fluid Mech.* 113: 221-239 (1981)

[4] B. Pouligny, M. Chassande-Mottin, Air ingestion by a buckled viscous jet of silicone oil impacting the free surface of the same liquid, *Phys. Rev. Let.*, 100, 154501 (2008)

[5] L. Mahadevan, W S. Ryu and A D.T. Samuel, Fluid rope trick investigated, *Nature* 392, 140 (1998)

[6] N. M. Ribe, Coiling of viscous jets, *Proc. R. Soc. Lond. A* 460, 3223-3239 (2004)

[7] B. Yesilata, C. Clasen, G.H. McKinley, Nonlinear shear and extensional flow dynamics of wormlike surfactant solutions, *J. Non-Newtonian Fluid Mech.* 133, 73-90 (2006)

[8] J. Eggers, Nonlinear dynamics and breakup of free-surface flows, *Rev. Mod. Phys.* 69, 865 - 930 (1997)

[9] J. Eggers, E. Villermaux, Physics of liquid jets, *Rep. Prog. Phys.* 71 (2008)

[10] C. Clanet, J.C. Lasheras, Transition from dripping to jetting, *J. Fluid Mech.*, 383, 307-326 (1999)

[11] D.T. Papageorgiou, On the breakup of viscous liquid threads, *Phys. Fluids* 7 (7), (1995)

[12] J. Eggers, Universal pinching of 3D axisymmetric free-surface flows, *Phys. Rev. Lett.* 71, 3458 (1993)

[13] P. Doshi, R. Suryo, O. E. Yildirim, G.H. McKinley, O. A. Basaran, Scaling in pinch-off of generalized Newtonian fluids, *J. Non-Newtonian Fluid Mech.* 113 1-27 (2003)

[14] S. L. Anna, G. H. McKinley, Elasto-capillary thinning and breakup of model elastic liquids, *J. Rheol.* 45 (1) (2001)

[15] M.A. Matovich, J.R.A. Pearson, Spinning of a molten threadline, *I&EC Fundamentals*, Vol 8, No 3, 512-520 (1969)

[16] E. J. Watson, The radial spread of a liquid jet over a horizontal plane, *J. Fluid Mech.*, 20, 481-499, (1964)

[17] E. Lorenceau, J. Eggers, D. Quéré, Air Entrainment by a Viscous Jet Plunging into a Bath, *Phys. Rev. Lett.* 93, 254501 (2004)

[18] J. W. M. Bush, A. E. Hasha, On the collision of laminar jets: fluid chains and fishbones, *J. Fluid Mech*, 511, 285-310. (2004)

[19] R. Buckingham, J. W. M. Bush, Fluid Polygons, *Phy. Fluids*, Vol 13, No 9 (2001)

[20] M. Zak, Dynamics of liquid films and thin jets, *SIAM J. Appl. Math.*, 37 (2) (1979)

[21] R. W. Freeman, L. L. Tavlarides, Observations of the instabilities of a round jet and the effect of cocurrent flow, *Phys. Fluids* 22, 782 (1979)

[22] A. Bejan, Buckling flows: a new frontier in fluid mechanics. *An. Rev. Num. Fluid Mech. and Heat Transfer*, pp. 262-304. Hemisphere. (1987)

[23] S. Kimura, A. Bejan, The buckling of a vertical liquid column, *J. Fluid Eng*, Vol. 105, No 4, pp. 469-473 (1983)

[24] J. O. Cruickshank, B. R. Munson, The viscous-gravity jet in stagnation flow, *J. Fluid Eng.* 104, 360-362 (1982)

[25] G.I. Taylor, Instability of jets, threads and sheets of viscous fluid, *Proc. 12th Intl Conf. Applied Mech.* (1969)

[26] J. O. Cruickshank, Viscous fluid buckling: A theoretical and experimental analysis with extensions to general fluid stability, *Ph.D. Thesis Iowa Univ.*, Iowa City (1980)

[27] J. O. Cruickshank, Low-Reynolds-number instabilities in stagnating jet flows, *J. Fluid Mech.*, 193: 111-127 (1988)

[28] B. Tchavdarov, A.L. Yarin and S. Radev, Buckling of thin liquid jets, *J.Fluid Mech*, vol 253, pp 593-615 (1993)

[29] A. L. Yarin and B. M. Tchavdarov, Onset of folding in plane liquid films, *J. Fluid Mech.*, 307: 85-99 (1996)

[30] L.Mahadevan, W.S. Ryu, A.D.T. Samuel, Correction to "Fluid rope trick investigated", *Nature* 403, 502 (3 February 2000)

[31] M Maleki, M Habibi, R Golestanian, NM Ribe, D Bonn, Liquid rope coiling on a solid surface, *Phys. Rev. Lett.* 93, 214502 (2004)

[32] M. Skorobogatiy, L. Mahadevan, Folding of viscous sheets and filaments, *Europhys. Lett.*, 52 (5), pp. 532-538 (2000)

[33] N.M. Ribe, Periodic folding of viscous sheets, *Phys.Rev. E* 68, 036305 (2003)

[34] L. Mahadevan, J.B. Keller, Periodic folding of thin sheets, *SIAM J. Appl. Math.* 55, No.6, 1609-1624 (1995)

[35] L. Mahadevan, J.B. Keller, Coiling of flexible ropes, *Proc. R. Soc. Lond. A*, 452, 1679-1694 (1996)

[36] M. Habibi, N. M. Ribe, D. Bonn, Coiling of elastic ropes, *Phys. Rev. Lett.* 99, 154302 (2007)

[37] A Kaye, A bouncing liquid stream, *Nature* 197, 100, 1001-1002 (1963)

[38] A.A. Collyer and P.J. Fisher, The Kaye effect revisited, *Nature* 261, 682 - 683 (1976)

[39] Versluis M, Blom C, van der Meer D, Van der Weele K and Lohse D, Leaping shampoo and the stable Kaye effect, *J. Stat. Mech* (2006)

[40] H. Rehage and H. Hoffmann, Rheological properties of viscoelastic surfactant systems, J. Phys. Chem., Vol. 92, No. 16 (1988)

[41] R. B. Bird, R. C. Amstrong, O. Hassager, Dynamics of polymeric liquids, John Wiley & Sons (1987)

[42] H.A. Barnes, The yield stress, a review of $\pi\alpha\nu\tau\alpha$ $\rho\epsilon\iota$, everything flows ?, *J. Non-Newtonian Fluid Mech.*, 81 133–178 (1999)

[43] J.H. Watson, The diabolical case of the recurring yield stress, *Appl. rheol.* 14, 40-45 (2004)

[44] Will Hartt (Procter and Gamble company), personal communication (2007)

[45] J. N. Israelachvili, D. J. Mitchell, B. W. Ninham, Theory of self-assembly of hydrocarbon amphiphiles into micelles and bilayers, *J. Chem. Soc., Faraday Trans.* 2, 72, 1525 - 1568, (1976)

[46] J.P. Rothstein, Transient extensional viscosity of wormlike micelles solutions, *J. Rheol.*, 47 (5) pp 1227-1247 (2003)

[47] J.-F. Berret, J. Appell and G. Porte, Linear rheology of entangled wormlike micelles, *Langmuir*,9, 2851-2854 (1993)

[48] P.-G. de Gennes, Simple views on condensed matters, *Modern Condensed Matter Physics*, Vol. 12 (1997)

[49] M.E. Cates, Repatation of living polymers: Dynamics of entangled polymers in the presence of reversible chain-scission reactions, *Macromolecules* 20, 2289 (1987)

[50] A. Bhardwaj, E. Miller, J.P. Rothstein, Filament stretching and capillary breakup extensional rheometry measurements of viscoelastic wormlike micelle solutions, *J. Rheology*, 51 (4) 693-719 (2007)

[51] M. S. N. Oliveira, G. H. McKinley, Iterated stretching and multiple beads-on-a-string phenomena in dilute solutions of highly extensible flexible polymers, *Phy. Fluids* 17, 071704 (2005)

[52] R.I. Tanner, Engineering rheology, 2nd ed, pp 421-435, Oxford Scientific Press (2000)

[53] F.T. Trouton, On the coefficient of viscous traction and its relation to that of viscosity, *Proc. Roy. Soc. Lond. A* Vol. 77, 519, 426-440 (1906)

[54] V.M. Entov, E.J. Hinch, Effect of a spectrum of relaxation times on the capillary thinning of a filament of elastic liquid, *J. Non-Newtonian Fluid Mech.*, 72, 31–53 (1997)

[55] N.A. Spenley, M.E. Cates, T.C.B. McLeish, Nonlinear rheology of wormlike micelles, *Phys. Rev. Let.*, Vol 71, No 6 (1993)

[56] J.-F. Berret, D. C. Roux, G. Porte, Isotropic-to-nematic transition in wormlike micelles under shear, *J. Phys. II France*, 4, 1261-1279 (1994)

[57] R. G. Larson, The structure and rheology of complex fluids, Oxford University Press (1999)

[58] PAC, 1972, 31, 577 (Manual of Symbols and Terminology for Physicochemical Quantities and Units, Appendix II: Definitions, Terminology and Symbols in Colloid and Surface Chemistry), p613

[59] T. Shikata, S. J. Dahman, D. S. Pearson, Rheo-optical behavior of wormlike micelles, *Langmuir*,10, 3470-3476 (1994)

[60] J.-M. Li, W.R. Burghardt, Flow birefringence in axisymmetric geometries, *J. Rheol*, Vol 39, 4, 743-766 (1995)

[61] C. Clasen, J. Bico, V. Entov, G.H. McKinley, 'Gobbling drops': the jetting/dripping transition in flow of polymer solutions, Under consideration for publication

[62] E. Buckingham, On physically similarr systems: illustrations of the use of dimensional equations, *Phys. Rev.* 4, No. 4, 345 (1914)

[63] M. S. Chai, Y. L. Yeow, Modelling of fluid M1 using multiple relaxation time constitutive equations, *J. Non-Newt. Fluid. Mech.*, 35, 459-470 (1990)

[64] A. Bhardwaj, D. Richter, M. Chellamuthu, J. P. Rothstein, The effect of pre-shear on the extensional rheology of wormlike micelle solutions, *Rheol Acta* 46, 861–875 (2007)